University of Iowa

Iowa Research Online

Theses and Dissertations

Fall 2010

Novel multi-scale topo-morphologic approaches to pulmonary medical image processing

Zhiyun Gao
University of Iowa

Recommended Citation

NOVEL MULTI-SCALE TOPO-MORPHOLOGIC APPROACHES TO

PULMONARY MEDICAL IMAGE PROCESSING

by

Zhiyun Gao

<u>An Abstract</u>

Of a thesis submitted in partial fulfillment of the
requirements for the Doctor of Philosophy
degree in Electrical and Computer Engineering
in the Graduate College of
The University of Iowa

December 2010

Thesis Supervisor: Associate Professor Punam K. Saha

ABSTRACT

The overall aim of my PhD research work is to design, develop, and evaluate a new practical environment to generate separated representations of arterial and venous trees in non-contrast pulmonary CT imaging of human subjects and to extract quantitative measures at different tree-levels. Artery/vein (A/V) separation is of substantial importance contributing to our understanding of pulmonary structure and function, and immediate clinical applications exist, e.g., for assessment of pulmonary emboli. Separated A/V trees may also significantly boost performance of airway segmentation methods for higher tree generations. Although, non-contrast pulmonary CT imaging successfully captures higher tree generations of vasculature, A/V are indistinguishable by their intensity values, and often, there is no trace of intensity variation at locations of fused arteries and veins. Patient-specific structural abnormalities of vascular trees further complicate the task.

We developed a novel multi-scale topo-morphologic opening algorithm to separate A/V trees in non-contrast CT images. The algorithm combines fuzzy distance transform, a morphologic feature, with a topologic connectivity and a new morphological reconstruction step to iteratively open multi-scale fusions starting at large scales and progressing towards smaller scales. The algorithm has been successfully applied on fuzzy vessel segmentation results using interactive seed selection via an efficient graphical user interface developed as a part of my PhD project. Accuracy, reproducibility and efficiency of the system are quantitatively evaluated using computer-

generated and physical phantoms along with *in vivo* animal and human data sets and the experimental results formed are quite encouraging.

Also, we developed an arc-skeleton based volumetric tree generation algorithm to generate multi-level volumetric tree representation of isolated arterial/venous tree and to extract vascular measurements at different tree levels. The method has been applied on several computer generated phantoms and CT images of pulmonary vessel cast and *in vivo* pulmonary CT images of a pig at different airway pressure. Experimental results have shown that the method is quite accurate and reproducible.

Finally, we developed a new pulmonary vessel segmentation algorithm, i.e., a new anisotropic constrained region growing method that encourages axial region growing while arresting cross-structure leaking. The region growing is locally controlled by tensor scale and structure scale and anisotropy. The method has been successfully applied on several non-contrast pulmonary CT images of human subjects. The accuracy of the new method has been evaluated using manually selection of vascular and non-vascular voxels and the results found are very promising.

Abstract Approved: _____
                     Thesis Supervisor

                     _____
                     Title and Department

                     _____
                     Date

NOVEL MULTI-SCALE TOPO-MORPHOLOGIC APPROACHES TO

PULMONARY MEDICAL IMAGE PROCESSING

by

Zhiyun Gao

A thesis submitted in partial fulfillment of the
requirements for the Doctor of Philosophy
degree in Electrical and Computer Engineering
in the Graduate College of
The University of Iowa

December 2010

Thesis Supervisor: Associate Professor Punam K. Saha

Graduate College
The University of Iowa
Iowa City, Iowa

CERTIFICATE OF APPROVAL

————————————————————

PH.D. THESIS

————————————

This is to certify that the Ph.D. thesis of

Zhiyun Gao

has been approved by the Examining Committee for the
thesis requirement for the Doctor of Philosophy degree
in Electrical and Computer Engineering at the December
2010 graduation.

Thesis Committee: ————————————————————
                  Punam K. Saha, Thesis Supervisor

                  ————————————————————
                  Milan Sonka

                  ————————————————————
                  Eric A. Hoffman

                  ————————————————————
                  Joseph M. Reinhardt

                  ————————————————————
                  Xiaodong Wu

ACKNOWLEDGEMENTS

The kingdom of research is not an island isolated to the rest of the world. What I have already traveled during years of my PhD studies can not be a pleasant journey without gifts from those outstanding individuals in and out of the University of Iowa. Such great and altruistic aids pave the roads of my life. I give my heartful gratitude to those warmhearted persons.

First of all I would like to thank my supervisor Dr. Punam Saha with his contribution and support through out my PhD studies. He has always gave me constructive and effective guidance in my work and made me grow up in the soil of science and engineering. I greatly appreciate the hopes and efforts he put on me and respect his carefulness and patience on reviewing my papers and thesis. I am also thankful for the excellent example he has setup for me in the field of research.

I am also grateful to Dr. Milan Sonka who opened a door for me to the realm of the medical image processing where I found my genuine interest. Knowledge learned from his lectures and academic interaction armed me as an essential weapon on this research road.

I would also like to show my gratitude to Dr. Eric Hoffman for his funding source to support my PhD study. Special thanks go to professional collaboration with Sara Alford, Randall Grout, Jered Sieren, Dragos Vasilescu, Colin Holtze and Ann Thompson from the Radiology Department. I also appreciate VIDA diagnoses provided me their software PW2, which facilitaed my research experiment.

I cordially appreciate Dr. Joseph Reinhardt and Dr. Xiaodong Wu being my PhD defense committee with their patient and inspiring work.Moreover, I would like to give my thanks to all the faculties who taught me in the courses of the Department of Electrical and Computer Engineering and other departments, from whom I learned lots of research related knowledge which is definitely beneficial in my following PhD pursuit.

I am indebted to my colleagues Honghai Zhang, Guoyuan Liang, Ziyue Xu, Yinxiao Liu, Yan Xu, Hong Duan, Cheng Li and Subhadip Basu to support and suggest me in my study. I cherish the memory of academic discussion and wonderful lab life with them.

My sincere thanks go to the department secretary Catherine Kern and the administrative assistant Dina Blanc for setting up paper work and their patient assistance.

Most of all thanks are for my loving, encouraging, and supportive husband Shanhui Sun, without whose support in every minute I cannot get through this PhD period and with whom my life is more beautiful and my future is full of sunshine.

Last but not least, I would like to thank my parents, parents in law and other family members. Without their love and support, it is not possible for me to complete this thesis.

ABSTRACT

The overall aim of my PhD research work is to design, develop, and evaluate a new practical environment to generate separated representations of arterial and venous trees in non-contrast pulmonary CT imaging of human subjects and to extract quantitative measures at different tree-levels. Artery/vein (A/V) separation is of substantial importance contributing to our understanding of pulmonary structure and function, and immediate clinical applications exist, e.g., for assessment of pulmonary emboli. Separated A/V trees may also significantly boost performance of airway segmentation methods for higher tree generations. Although, non-contrast pulmonary CT imaging successfully captures higher tree generations of vasculature, A/V are indistinguishable by their intensity values, and often, there is no trace of intensity variation at locations of fused arteries and veins. Patient-specific structural abnormalities of vascular trees further complicate the task.

We developed a novel multi-scale topo-morphologic opening algorithm to separate A/V trees in non-contrast CT images. The algorithm combines fuzzy distance transform, a morphologic feature, with a topologic connectivity and a new morphological reconstruction step to iteratively open multi-scale fusions starting at large scales and progressing towards smaller scales. The algorithm has been successfully applied on fuzzy vessel segmentation results using interactive seed selection via an efficient graphical user interface developed as a part of my PhD project. Accuracy, reproducibility and efficiency of the system are quantitatively evaluated using computer-

generated and physical phantoms along with *in vivo* animal and human data sets and the experimental results formed are quite encouraging.

Also, we developed an arc-skeleton based volumetric tree generation algorithm to generate multi-level volumetric tree representation of isolated arterial/venous tree and to extract vascular measurements at different tree levels. The method has been applied on several computer generated phantoms and CT images of pulmonary vessel cast and *in vivo* pulmonary CT images of a pig at different airway pressure. Experimental results have shown that the method is quite accurate and reproducible.

Finally, we developed a new pulmonary vessel segmentation algorithm, i.e., a new anisotropic constrained region growing method that encourages axial region growing while arresting cross-structure leaking. The region growing is locally controlled by tensor scale and structure scale and anisotropy. The method has been successfully applied on several non-contrast pulmonary CT images of human subjects. The accuracy of the new method has been evaluated using manually selection of vascular and non-vascular voxels and the results found are very promising.

TABLE OF CONTENTS

LIST OF TABLES

LIST OF FIGURES

CHAPTER 1
INTRODUCTION

1.1 Introduction and Project Definition

Over the last few decades, multi-layered extraction of knowledge embedded in two- and higher-dimensional images has remained a front-line research topic [113, 114, 55, 157, 42, 5, 143]. In particular, the availability of a wide spectrum of medical imaging techniques [11] including MR, ultrasound, CT, PET, and X- and γ-rays have further intensified the image processing needs for computerized extraction of knowledge from the huge image data sets daily produced in diagnostic, therapeutic and clinical and biomedical research imaging scan. The process of identifying and outlining relevant anatomical structures in an image dataset, often, referred to as *image segmentation or segmentation*, in short, is a central challenge in a variety of medical applications including surgical planning, 3D visualization, image enhancement and reconstruction, disease classification, data storage and compression. Major challenges in most medical image segmentation include, but not limited to, the following: (1) co-existence of multiple anatomic structures, (2) tight spatial coupling among different structures, (3) lack of well defined boundaries for several structures, (4) wide variations in shape and tissue volume of the same anatomic structure among subjects, (5) effects of disease, (6) effects of motion during imaging, and (7) limited signal-to-noise ratio (SNR) and spatial resolution. Several segmentation approaches, including manual outlining [58], boundary based [34, 63], region-based [51, 111, 132, 160, 159, 32],

and shape and model-based [25, 26] techniques have been introduced and subsequently modified and investigated in different medical imaging applications. Despite significant research effects over the two decades in medical image segmentation, the task has remained a challenge and several problems are yet unsolved. The overall aim of my PhD research work is to design, develop, and evaluate a new practical environment to generate separated representations of arterial and venous trees in non-contrast pulmonary CT imaging of human subjects and to extract quantitative measures at different tree-levels. The attempted task of artery/vein (A/V) segmentation is of substantial importance since separated A/V trees may significantly contribute to our understanding of pulmonary structure and function. Segmenting pulmonary A/V trees via CT imaging is a critical first step in the quantification of vascular geometry for purposes of determining, for instance, pulmonary hypertension, using vascular dimensions as a comparator for assessment of airway size, detection of pulmonary emboli and more. Segmentation of A/V trees may also be useful to enhance airway tree segmentation based on the relationship of artery and airway, and to provide landmarks for intra- and inter- subject pulmonary data registration. This research project will be accomplished by completing the following six specific aims:

Aim 1: Design and develop a complete method for artery/vein separation in non-contrast pulmonary CT imaging of human subjects using a novel multi-scale topo-morphologic opening algorithm.

Aim 2: Design and perform experiments to evaluate the accuracy, reproducibility, and efficiency of the new artery/vein segmentation algorithm.

Aim 3: Design and develop a complete method to generate multi-generation tree representation for arterial/venous trees and extract quantitative measures at different tree-levels.

Aim 4: Design and perform experiments to evaluate the accuracy and reproducibility of quantitative A/V parameters at multi-generation tree representation.

Aim 5: Design and develop a complete method for pulmonary vessel segmentation in non-contrast CT imaging of human lung using a novel tensor scale based constrained region growing algorithm.

Aim 6: Design and perform experiments to evaluate the accuracy of the vasculature segmentation algrithm using tensor scale-based constrained region growing.

Our pulmonary vessel segmentation algorithm is based on the region growing technique [111, 132, 160, 15, 21, 52, 112] initiated with a few seeds on pulmonary vasculature close to their exits from cardiac territory. A fundamental challenge faced in a region growing technique for tracing vascular structures, especially, at finer scales, is that, often, the continuity of structures are broken by noise and other imaging artifacts at *in vivo* imaging regime. However, a human expert may reconstruct the continuity using local structure geometry of vascular tree. Our method attempts to solve this fundamental problem using tensor scale, a local morphologic scale introduced by Saha *et al.* [117], that captures local structure orientation and geometry using an ellipsoidal model. The basic idea behind our method is to facilitate re-

gion growing along a structure while restricting the growth across it. This method involves modeling a local region growing process using tensor scale. A tensor scale-based constrained region growing algorithm has been developed and its performance on a limited set of human non-contrast pulmonary CT images has been evaluated.

The method for A/V separation has been developed and reported at IEEE Transaction on Medical Imaging [123]. It starts with a fuzzy segmentation of the assembly of two similar-intensity objects (the arterial and venous trees for the current application), and two sets of seed points (one for arteries and the other for veins) and outputs spatially separated arterial and venous trees. The algorithm is designed under the assumption that fusions of arteries and veins are locally separable using a suitable morphological opening operator. The method uses a novel approach to solve the following two fundamental challenges: how to find local size of morphological operators and how to trace continuity of locally separated regions. These challenges are met by combining fuzzy distance transform, a morphologic feature, with a topologic fuzzy connectivity and a new morphological reconstruction to iteratively open finer and finer details starting at large scales and progressing towards smaller scales. In short, artery/vein separation is modeled as a new multi-scale opening task and the method provides a unique solution, which offers a new research avenue of multi-scale topo-morphologic operations. The method effectively employs efficient user intervention at locations where the assumption of local morphological separability does not hold due to imaging ambiguity or other reasons. Efficiency and effectiveness of the new A/V segmentation algorithm is examined in terms - (1) required user interven-

tion, (2) accuracy on computer-generated phantoms and pulmonary vessel casts of a pig with known ground truth, and (3) reproducibility of A/V segmentation by two mutually-blind experts.

A new tree-analysis based method has been developed to extract artery/vein morphometric measures at different tree-levels. The tree-analysis method starts with the arc skeleton of an arterial or a venous tree and detects topological junctions and end voxels in the arc skeletal representation. Several challenges occurred due to the digital space have been solved using new methods relating — (1) topological correction, (2) single branch and end voxel detection, (3) tree construction, (4) merging false junctions, and (5) pruning noisy branches. Finally, different morphometric measures at different tree-levels are extracted by generating a multi-generation tree representation of the original volumetric data. The accuracy and reproducibility of the tree-analysis method has been evaluated on computer phantoms and *in vivo* and pulmonary cast CT data of pig's lung.

The designed PhD research project involves research works related to the following major areas - (1) simultaneous multi-object segmentation, (2) multi-scale approaches, (3) fuzzy geometry and topology, (4) morphology and (5) tree analysis . In the following section, a brief literature survey for each of these research areas is presented with emphasis on separating multi-objects in medical imaging and the contribution by my research study. Also, current state of the art research works related to vessel segmentation and artery-vein separation is presented in the following section.

1.2 Literature Survey

1.2.1 Artery/Vein Separation

The challenges in separating arteries and veins are multi-folded including: (1) A/V are indistinguishable by their intensity values in non-contrast pulmonary CT images, (2) often, there is no trace of intensity variation at locations of fused arteries and veins, (3) there is complex and tight coupling and fusion between A/V trees with arbitrary and multi-scale geometry, especially at branching locations, and (4) limited SNR and relatively low resolution are typical for *in vivo* CT imaging. Patient-specific structural abnormalities of vascular trees further complicate the task. Several works have been reported in literature addressing the task of separating arteries and veins using improvised image acquisition techniques; a thorough discussion on difficulties of such approaches, especially for smaller vessels, have been presented by Bemmel *et al.* [162]. To the best of our knowledge, only a few post-processing methods have been published for separating arteries and veins [162, 73]. The previous methods have only been applied to MR data and did not use morphological scale information. These methods primarily rely on intensity variations or presence of edge information at the adherence locations between A/V trees and may not work for *in vivo* CT images where no such intensity variations are present at locations of adherence. Two methods for A/V classification from pulmonary CT images have been presented by Büelow *et al.* [151] and Yonekura *et al.* [172]. Büelow *et al.*'s method for A/V separation is based on prior knowledge of airway tree segmentation which may not produce optimal A/V separation at distal branches in a pulmonary vascular tree.

The method by Yonekura *et al.* is based on using specific anatomical features of pulmonary arterial and venous trees and also, the knowledge of airway segmentation. A major difficulty of such method is the non-uniformity of different features over wide range of scales in the pulmonary tree and may not generalize to A/V separation in other body region. Our method is fundamentally different from previous method that neither requires any prior knowledge of arterial tree nor uses any anatomical feature to distinguish between arterial and venous trees. Rather, the method is based on the morphological signature of two different structures left at the locations of fusion at various scales.

1.2.2 Multi-Object Segmentation

Recently, increasing research interests are observed [38, 66, 30, 37, 61, 59, 60, 154, 35] related to multi-object segmentation where the fundamental thrust is to define an object in the context of its co-objects. Freedman *et al.* [38] developed a simultaneous multi-object segmentation algorithm using an integrated active appearance model for multiple organs with a probabilistic approach for pixel intensity within respective regions. Kobatake [66] designed a computer-aided-diagnostic system using a knowledge-based hierarchical model for multi-object representation in an image. Bruijne and Nielsen [30] developed a segmentation algorithm for multiple objects using a stochastic optimization approach for distribution of shape particles where spatial relationship among shape particles in objects are modeled using shape priors. Fleureau *et al.* [37] presented a multi-agent scheme for simultaneous segmentation of cardiac structures via multi-slice CT imaging using prior feature knowledge

in conjunction with image-derived properties relating homogeneity, connectivity, and compactness. Kainmueller [61, 59] combined a multi-object deformable model with graph-based optimization techniques to simultaneously segment multiple bone structures at different joints via CT imaging while maintaining bone surface topology; later they modified their approach to incorporate statistical shape models instead of a deformable model into their framework [60]. Tsai *et al.* [154] developed a new approach to capture spatial correlation among multiple objects using a parametric model for multiple signed distance transforms, one for each object. This model is used for simultaneous multi-object segmentation by coupling it with mutual information to optimize the parameters of the model for a test image. Ferrant *et al.* [35] developed a hierarchical approached for simultaneous segmentation of multiple brain structures in MR images using deformable-surface based atlas model.

A parallel research efforts is available in the literature on simultaneous multi-object segmentation using a competitive approach [51, 159, 14, 126, 23] where different co-objects competes among themselves to grab an image pixel/voxel based on prior knowledge, image features and some rules and the pixel/voxel is assigned to the winning object. Saha *et al.* [159, 126] developed an iterative approach to separate two objects using path-based fuzzy connectivity where, during an iteration, a pixel/voxel is assigned to an object with greater connectivity strength and the result is refined in the next iteration using the rule that, once a territory is assigned to an object, paths from its co-object are not allowed to pass through it. Herman and Carvalho [51] developed a modified simultaneous segmentation algorithm allowing

different fuzzy affinity rules for different objects. Cates *et al.* [14] used watershed approach to develop a user-assisted competitive segmentation framework and studied its effectiveness segment different anatomic structures in Visible Human Female head and neck color cryosection data and also, to segment tumors in brain MRI. Ciofolo and Barillot [23] developed a new approach for simultaneous segmentation of multiple structures with competitive level sets driven by fuzzy control where several contours evolve simultaneously toward desired anatomical targets.

Our method for simultaneous A/V separation falls in the second category where two regions compete with each other to grow from large scales to finer ones. The competitive growth of two structures is governed by fuzzy morpho-connectivity and multi-scale opening.

1.2.3   Multi-Scale Image Processing and Analysis

Scale is a widely used notion in image processing and analysis that evolved in the form of scale-space theory whose key idea is to represent and analyze an image at various resolutions. Scale [67, 77, 82, 170] may be thought of as the spatial resolution, or, more generally, a range of resolutions needed to ensure a sufficient yet compact object representation. Scale plays an important role in determining the optimum trade-off between noise smoothing and perception/detection of structures. Also, scale is helpful in breaking a computer vision and image-processing task into a hierarchy of tasks where tasks at higher levels deal with the larger structures. Marr [82] pointed out several benefits of multi-scale image analysis and computer vision. Witkin [170] and Koenderink [67] mathematically formulated the concept of scale in the form of

scale-space theory. Discrete scale-space representations [77] have been used in several imaging applications including segmentation [166], clustering [74], classification [80], and structural analysis [36].

Although, scale-space image representations have provided significant insight, it is not obvious-(1) how to unify the information from images at different scales, and (2) how to identify the optimal scale at each individual image point. These questions have paramount implications on several computer vision and image analysis tasks. For example, a knowledge of "local scale" would allow us to spatially tune the neighborhood size in different processes leading to selection of small neighborhoods in regions containing fine detail or near a boundary, versus large neighborhoods in deep interiors [132]. Also, local scale would be useful in developing space-variant parameter controlling strategies [129] to improve the quality of results. These observations have stimulated interest in research relating to the concept of local scale [152, 106, 33, 75]. Using the force field model, Tab and Ahuja [152] defined scale at each location as the minimum scale of the Gaussian weighting function at which the resultant attractive force exceeds a threshold (i.e., the force stabilizes). Pizer *et al.* [106] selected optimal local scale from the scale-space representation that maximizes "medialness" among the values at various scales. In their medialness model, local scale represents the distance at which a pair of opposing boundaries is expected. Elder and Zucker [33] described local scale as the smallest scale yielding a gradient measure above a statistically reliable threshold. Liang and Wang [75] proposed local scale as a measure of the number of zero crossings of the second-order derivatives of

the signal along a direction within a fixed-length and the amount of unipolar energy in these derivatives.

The notion of "local morphologic scale" was initiated by Saha *et al.* [132, 129] using a spherical model where local scale at an image voxel p indicate the size of the largest sphere centered at p and contained in the same homogeneous region. The notion of this association between scale and local structure size has been found to be effective in imaging applications including segmentation [57, 127, 171], filtering [129], registration [94], and removal of partial volume effects in rendering [144]. Later Saha developed a new notion of local morphologic scale referred to as "tensor scale" using an ellipsoidal model of local structure [117]. Research works explores applications of local morphologic scale in image segmentation. Mukhopadhya and Chanda developed a series of multi-scale morphological approaches to enhance and segment gray scale images [93, 91, 92]. They developed a multi-scale local contrast enhancement algorithm [91] using multi-scale top-hat transformation and later used this concept in image noise filtering [92] where features at lower scales are assigned smaller weights. Zheng *et al.* [175] developed a modified multi-scale morphological algorithm to enhance local contrast and demonstrated its effectiveness in X-ray imaging. Mukhopadhya and Chanda presented a multi-scale image segmentation algorithm [93] using a modified watershed approach where an image is subdivided into small regions first and then these regions progressively grow, merge, and saturate under a set of multi-scale morphological rules.

In the proposed research project, we develop a new constrained region growing

using local tensor scale that facilitates object region growth along a structure while restricting cross-structure growth. In the context of A/V separation, we demonstrate the correlation between ordinary or fuzzy distance transform and local scale and present a solution of local optimal scale to morphological separate two mutually fussed structures

1.2.4 Fuzzy Geometry and Topology

Rosenfeld introduced the notion of fuzzy geometry and topology in the context of image processing and pattern recognition [111, 112]. He defined several geometric and topologic concepts in a fuzzy digital image including adjacency, separation, and connectedness, area, perimeter, diameter, convexity, medial axes and thinning. More recently, Buckley and Eslami [12] have formulated some fundamental definitions related to fuzzy lines and planar geometry using the notion of a fuzzy point and have studied their properties. In our current research, we primarily use fuzzy geometric and topology features related to distance and connectivity. In the following paragraphs, we present a survey of research works related to these two fields.

Distance transform (DT) [7, 8, 9, 28, 96, 116], a shortest distance measure from the background, has been popularly adopted in many digital geometric applications [65] of binary objects. Most DT methods approximate the global Euclidean distance by propagating local distances between neighboring pixels. As observed in [9], this simple yet fundamental idea was first presented by Rosenfeld and Pfaltz [115] in 1968. In [116], they discussed different digital distance functions including city blocks and chess board distances and described how they can be mixed to create octagonal DTs

that are better approximations of the Euclidean distances. Okabe, Toriwaki, and Fukumara [96] investigated these issues in 3D; this was independently discovered and illustrated in [7]. In [28], Danielsson described how to reasonably compute the true Euclidean DT in digital spaces, including the 3D case. Borgefors [7, 8, 9] extensively studied DTs for binary 3D objects and presented the integer-valued approximation of the optimal local step lengths that are widely used by others. Local step optimization and accuracy of DT have further been studied by other research groups [4, 45, 165]. Saha *et al.* [134] introduced a generalized fuzzy DT (FDT) and established its metric property; applications of fuzzy distance transform have been studied by different research groups [29, 133, 148, 149, 150].

The notion of the "degree of connectedness" between two image pixels/voxels was first introduced by Rosenfeld [111, 112] in the context of studying the topology and geometry of fuzzy images. Rosenfeld's "degree of connectedness" [111] was further studied to understand the topological, geometrical, and morphological properties of fuzzy subsets [112]. Dellepiane and Fontana [32, 31] and Udupa and Samarasekera [160] were the first to suggest the use fuzzy connectivity in image segmentation. Udupa *et al.* [160] introduced a different framework for fuzzy connectivity bringing in a key concept of a local fuzzy relation called affinity on image pixels/voxels to capture their local hanging-togetherness. They showed how affinity can incorporate various image features in defining fuzzy connectedness, presented a general framework for the theory of fuzzy connectedness, and demonstrated how dynamic programming can be utilized to bring the otherwise seemingly intractable notion of fuzzy connectedness

into segmentation. Saha and Udupa *et al.* [132, 159, 126, 127] further advanced the theory of fuzzy connectedness considerably, bringing in notions of scale [132] and iterative relative fuzzy connectedness [159, 126] which was further extended by Herman and De Carvalha [51]. Saha and Udupa [127] axiomatically proved that the basic min-max construct used in fuzzy connectedness is the only possible formulation for fuzzy connectivity. Saha *et al.* [132] studied the issue of how to construct effective affinities and the use of local scale for this purpose. Aspects related to the computational efficiency of fuzzy connectedness algorithms have also been studied [13, 95]. The fuzzy connectedness methods have been utilized for image segmentation extensively in several applications, including multiple sclerosis lesion quantification [136, 161, 89, 90, 41, 2, 50], late life depression [72, 71], MR angiography [73, 109], CT angiography [1, 130], breast density quantification via mammograms [131].

Our presented methods are essentially designed and built using various notions of fuzzy geometry and topology. A new fuzzy connectedness based constrained region growing algorithm is formulated that combines tensor scale with fuzzy connectivity which facilitating region growth along local structure while arresting cross-structure leakages. In the context of A/V separation, we amalgamate fuzzy connectivity with fuzzy distance transform to realize a multi-scale morphologic opening for two iso-intensity structures fussed at various locations and scales.

1.2.5   Tree Generation and Analysis

Generation of topological tree representation from a vascular tree structucture [62, 169, 167, 173, 84] as well as matching two trees or solving the tree isomorphysm

problem [6] have remained active research fields. Kimia and Togawa [62] developed a vascular tree generation algorithm by identifying the root and end points and then by connecting them within the object to form a tree. They observed a good agreement for different tree-based geometric parameters measured in peritoneal vasculature of dogs. Williams and Wolff [169] developed a method to extract topological tree of pulmonary vasculature in CT images using differential geometry based vector fields and fluid flow approach. In their method junctions are detected as regions with non-zero divergence of the flow field. The method was applied on four CT data and qualitative results were presented. Wan *et al.* [167] developed an arc skeleton based approach to develop a tree-based multi-generation analysis of coronary vascular tree in micro-CT imaging. Yu *et al.*[173] developed a vascular tree generation algorithm using polygonal representation of vascular surface and differential geometric method. Martinez-Perez *et al* [84] developed a skeleton based method to generate tree structure for semi-automatically segmented arterial and venous trees and derived several topologic and geometric measures.

Althogh the problem of solving tree isomorphysm is beyond the scope of the current research, it may be highly related to our future works focusing on registration of multi-volume pulmonary images where tree isomorphysm may substantially help the registration process. There have been significant efforts reported in literature on tree matching. Pisupati *et al.* [104, 103] solved the rooted binary tree isomorphism problem using a dynamic programming algorithm and topological and geometric heuristics. Pelillo *et al.* [100, 101] proposed the association graph method

for matching rooted trees by detecting the maximal sub-tree isomorphism. Metzen *et al.* [88] used an enhanced association graph to formulate the entire tree matching problem as a single step optimization task. Graham *et al.* [44, 43] proposed a model-based approach where the extracted trees were assumed to arise from an initially unknown common tree structure corrupted by a sequence of modeled topological deformations. Lohe *et al.* [79] proposed a hierarchical tree search algorithm to compute the matching between branch points of anatomical trees. Tschirren *et al.* [156, 155] also proposed matching and labeling of human airway trees by using association graph. Among other non-graph-based approaches, Tang *et al.* [153] proposed an algorithm based upon minimization of tree edit distance between two vascular trees. Charnoz *et al.* [17, 16] proposed a tree matching algorithm for intra-patient hepatic vascular system registration based on a set of matching hypotheses which was updated to keep the best matches.

1.2.6   Mathematical Morphology

Mathematical morphology, introduced by Matheron [85, 86] and Serra [137, 138] provides an approach to the processing of digital images which is based on local shape and geometry. Mathematical morphological operations tend to simplify an image data extracting essential shape and geometric features while eliminating irrelevances. This property of the methodology along with its rigorous mathematical foundation has made it popular in the image processing community with its proven applicability in several imaging problems including noise elimination [47], clustering [108, 145], image segmentation [78, 99], feature extraction [139, 81, 105, 18, 83], video

supervision [139], and medical imaging [99]. Haralick *et al.* [48] presented a thorough discussion on different applications of mathematical morphology in image processing and analysis. Heijmans and Ronse formulated a general algebraic approach which both revealed the mathematical structure of morphological operations and unified several examples into one framework. Chen and Haralick [20] introduced the notion of recursive morphological operations and studied their theory and applications. Several research works were devoted on developing specialized computer architecture and hardware design to efficiently perform morphological operation [146, 146, 87, 76]. Zhuang and Haralick [176] presented the theory and algorithms to decompose a larger morphological structuring element into smaller elements facilitating computational aspects of morphological algorithms. Originally, mathematical morphology was developed for binary images and, later, it was adopted to grayscale and fuzzy images. Sternberg defined various morphological operations for grayscale images[147]. Fuzzy or soft morphological operations was proposed in [69] and its ability to reduce effects of impulsive noise was demonstrated. The properties of soft mathematical morphology were further investigated in [70, 140, 107, 142, 27, 46, 46, 39]. Chatzis and Pitas [18] presented a generalized formulation of fuzzy mathematical morphology using the notion of fuzzy inclusion indicator and demonstrated its robustness in object representation. The association between scale and a convolution kernel has been demonstrated in literature [3, 174] and this perspective of scale establishes its relation with mathematical morphology where every operation is associated with a morphological structure. Chen and Yan [19] showed that a binary morphological opening satisfies

causal property of scale-space for zero-crossings of curvature of the boundary curve of a 2D binary image. Jang and Chin [56] generalized their result to arbitrary convex structuring functions. Furthermore, mathematical morphology provides efficient and practical tools for abstraction of information from low level to high-level [49]. Jackway [54] proved that morphological dilation and erosion satisfy causality for any dimension with local maxima and local minima as feature points, respectively. In [163], Boomgaard and Smeulders show that dilation and erosion simulate morphological propagating of the initial condition into the scale-space, like the Gaussian convolution is the propagator for the linear diffusion equation. Park and Lee [98] proved that the scale-space of a one-dimensional gray-scale signal based on morphological filtering satisfies causality. In the proposed research work, we solve the problem of multi-scale opening of two similar-intensity structures using fuzzy distance transform and fuzzy connectivity models.

1.3   Organization of the Thesis

My thesis is organized in six chapters. The purpose of the current chapter is to outline the specified aims of my research works and present the overall significance, innovation and justification of my research works in the context of the state-of-art research. Also a literature survey is presented in this chapter. In the following, I outline major contents of individual chapters.

chapter 2: In this chapter, I describe the theory and algorithm of our new multi-scale topo-morphologic opening algorithm for artery/vein separation. Also, I describe our experimental plans, methods, and results evaluating the accuracy,

reproducibility and efficiency of our artery/vein separation algorithm. Specifically, this chapter describes our research plans, results, and observations related to Aims 1 and 2.

chapter 3: In this chapter, I describe the theory and algorithms related to generation of multi-level tree representation of pulmonary arteries/veins and extraction of quantitative measures at different tree levels. Also, I present our experimental plans, methods, and results evaluating the accuracy and reproducibility of the quantitative arterial/venous parameters at multi-level tree representations. Specifically, this chapter describes our research plans, results, and observations related to Aims 3 and 4.

chapter 4: In this chapter, I describe the theory and algorithms related to our new pulmonary vascular segmentation method using tensor scale based constrained region growing. Also, I describe our experimental plans, methods, and results evaluating the accuracy of the new vasculature segmentation method. Specifically, this chapter describes our research plans, results, and observations related to Aims 5 and 6.

chapter 5: In this chapter, I briefly outline a different application of our multi-scale topo-morphologic opening algorithm to segment acinus in high resolution micro-CT images of murine lung specimen. This research work is primarily being carried out by Mr. Vasilescu in Professor Hoffman's laboratory. I contributed to this research study by developing image processing cascade for acinar segmentation.

chapter 6: In this chapter, I draw my concluding remarks and present an

outline of my future research works related to my PhD projects.

CHAPTER 2
HUMAN PULMONARY ARTERY/VEIN SEPARATION USING
MULTI-SCALE TOPO-MORPHOLOGIC SEPARATION

2.1   Introduction

In this chapter, I describe a new multi-scale topo-morphologic opening theory
and algorithm for separation of arterial and venous trees from fuzzy segmentation
of pulmonary vasculature. Then I will describe experimental plans to examine the
performance of the artery/vein segmentation. In the following, first, I present ba-
sic definitions and notions along with brief descriptions for fuzzy connectivity and
fuzzy distance transform which were invented by our research group and are used
in the artery/vein separation algorithm. Then I present the theory and algorithm of
multi-scale topo-morphologic opening for artery/vein separation. In the experimental
methods and results section, I describe our plan and methods related to our experi-
ments evaluating the accuracy, reproducibility, and efficiency of the method. Finally,
I present our experimental results and draw our conclusion.

2.2   Basic Definition and Notations

The current work is designed for three-dimensional medical images, commonly
defined on cubic grids. A three dimensional (3D) cubic grid, or simply a *cubic grid*, is
represented by the points in $\mathbb{Z}^3$ where $\mathbb{Z}$ is the set of all integers. A *grid point*, often
referred to as a *point* or a *voxel*, is represented by a triplet of integer coordinates. Two
points $p, q \in \mathbb{Z}^3$ are called *adjacent* if and only if $\alpha(p,q) = 1$ where α is a reflexive and

symmetric relation. Standard 26-adjacency [119] is used here for α, i.e., two points (x_1, x_2, x_3) and (y_1, y_2, y_3) in $\mathbb{Z}^3$ are adjacent if and only if $max_{1\leq i\leq 3}|x_i - y_i| \leq 1$, where $|\cdot|$ denotes the absolute value. Two adjacent points are often referred to as *neighbors* of each other; the set of 26-neighboors of a point p excluding itself is denoted by $\mathcal{N}^*(\mathrm{p})$. An image may be defined using an *image intensity function* $f : \mathbb{Z}^3 \to \mathbb{Z}^+$, where $\mathbb{Z}^+$ is the set of positive integers including zero. An *object* $\mathcal{O}$ is a fuzzy subset $\{(p, \mu_{\mathcal{O}}(p))|p \in \mathbb{Z}^3\}$ of $\mathbb{Z}^3$, where $\mu_{\mathcal{O}} : \mathbb{Z}^3 \to [0, 1]$ is its membership function. The support $\Theta(\mathcal{O})$ of an object $\mathcal{O}$ is the set of all points with non-zero membership, i.e., $\Theta(\mathcal{O}) = \{p|p \in \mathbb{Z}^3 \text{ and } \mu_{\mathcal{O}}(p) \neq 0\}$. Images are always acquired with a finite field of view. Thus, we will assume that an object always has a bounded support. Let S denote a set of points; a *path* π in S from $p \in S$ to $q \in S$ is a sequence $\langle p = p_1, p_2, \cdots, p_l = q \rangle$ of points in S such that every two successive points on the path are adjacent. A *link* is a path $\langle p, q \rangle$ consisting of exactly two mutually adjacent points $p, q \in \mathbb{Z}^3$.

2.2.1 Fuzzy Connectivity

Fuzzy connectivity defines the strength of connectivity between any two points p, q in an image using a symmetric and reflexive 2-ary fuzzy relation referred to as "affinity". *Affinity* between any two points p, q, denoted as $\mu_{\kappa}(p, q)$, indicates the "hanging-togetherness" between the two points in a target object. More precisely, $\mu_{\kappa}(p, q)$ is the strength of the link $\langle p, q \rangle$ and its value lie in the interval [0,1]. Under a given fuzzy affinity relation κ, *the strength of a path* $\pi = \langle p = p_1, p_2, \cdots, p_l = q \rangle$,

denoted as $\mu_{\mathcal{N}}(\pi)$ is defined as the strength of the weakest link on the path, i.e.,

$$\mu_{\mathcal{N}}(\pi) = \min_{1 \leq i \leq l} \mu_{\kappa}(p_i, p_{i+1}). \tag{2.1}$$

There are infinitely many paths between two points p, q and let $\mathcal{P}(p, q)$ denote the set of all paths from p to q. The fuzzy connectivity between p and q, denoted as $\mu_K(p, q)$, is defined as the strength of the strongest path among all paths in $\mathcal{P}(p, q)$, i.e.

$$\mu_K(p, q) = \max_{\pi \in \mathcal{P}(p,q)} \mu_{\mathcal{N}}(\pi). \tag{2.2}$$

Finally, for given set S of seed points, the fuzzy object is defined as a fuzzy set $\mathcal{O}$ where the membership values at any point p indicates the maximum strength of fuzzy connectivity to any seed point in S, i.e.,

$$\mu_{\mathcal{O}}(p) = \max_{s \in S} \mu_K(p, s) \tag{2.3}$$

It has been shown in [127], that fuzzy connectivity is a similitude fuzzy relation and an efficient computational solution was presented in [160].

2.2.2   Fuzzy Distance Transform

Distance transform is a local depth measure inside an object and we call it "fuzzy distance transform" when the object representation is fuzzy. Fuzzy distance transform [134] accounts for both partial voxel occupancy and spatial heterogeneity of an object distribution. The *length* of a link $\langle p, q \rangle$ is calculated as $\frac{1}{2}(\mu_{\mathcal{O}}(p) +$

$\mu_{\mathcal{O}}(q)) \times \|p - q\|$, where $\|\cdot\|$ denotes any Euclidean L2 norm. The *length of a path* $\pi = \langle p_1, p_2, \cdots, p_l \rangle$ in a fuzzy object $\mathcal{O}$, denoted by $\Pi_{\mathcal{O}}(\pi)$, is defined as the sum of lengths of all links along the path, i.e.,

$$\Pi_{\mathcal{O}}(\pi) = \sum_{i=1}^{l-1} \frac{1}{2}(\mu_{\mathcal{O}}(p_i) + \mu_{\mathcal{O}}(p_{i+1})) \times \|p_i - p_{i+1}\|. \tag{2.4}$$

Between any two points $p, q \in \mathbb{Z}^3$, infinitely many paths may exist; let $\mathcal{P}(p, q)$ denote the set of all paths from p to q. A path $\pi_{p,q} \in \mathcal{P}(p, q)$ is *one of the shortest paths* from p to q in $\mathcal{O}$, if and only if, $\Pi_{\mathcal{O}}(\pi_{p,q}) \leq \Pi_{\mathcal{O}}(\pi)$ for all $\pi \in \mathcal{P}(p, q)$. It may be noted that the shortest path between two points $p, q \in \mathbb{Z}^3$ may not be unique. The *fuzzy distance* from $p \in \mathbb{Z}^3$ to $q \in \mathbb{Z}^3$ in an object $\mathcal{O}$, denoted by $\omega_{\mathcal{O}}(p, q)$, is the length of one of the shortest paths from p to q, i.e

$$\omega_{\mathcal{O}}(p, q) = \min_{\pi \in \mathcal{P}(p,q)} \Pi_O(\pi). \tag{2.5}$$

It has been shown in [134] that fuzzy distance satisfies the metric properties in both continuous as well as discrete spaces in any dimension. The *fuzzy distance transform* or FDT of an object $\mathcal{O}$ is represented as an image $\{(p, \Omega_{\mathcal{O}}(p)) | p \in \mathbb{Z}^3\}$, where $\Omega_{\mathcal{O}} : \mathbb{Z}^3 \to \Re^+$ denotes the fuzzy distance transform value at a given point; R^+ is the set of positive real numbers including zero. $\Omega_{\mathcal{O}}(p)$ is defined as the fuzzy distance between p and its nearest points in $\bar{\Theta}(\mathcal{O}) = \mathbb{Z}^3 - \Theta(\mathcal{O})$. In other words,:

$$\Omega_{\mathcal{O}}(p) = \min_{q \in \bar{\Theta}(\mathcal{O})} \omega_{\mathcal{O}}(p, q). \tag{2.6}$$

2.3 Multi-Scale Topo-Morphologic Opening: Theory, Algorithms and an Application to A/V Separation

As described in the previous chapter, in the current project, artery/vein separation is modeled as a multi-scale opening task. This method has already been published in the journal of IEEE Transactions on Medical Imaging [123]. Consider two iso-intensity cylindrical objects with significant mutual overlap as illustrated in Figure 2.1(a). Often, the intensity variations at fusions may not be a reliable feature to separate the two structures. On the other hand, the two structures may frequently be locally separable using a suitable morphological opening operator. The questions are how to determine local size of suitable morphological operators and how to combine the locally separated regions.

The separation process is initiated by picking two seeds, one for each object, as shown in Figure 2.1(b) and continues by exploring connectivity on the FDT image. Using the knowledge that the two seeds represent two different objects, a threshold may be selected on the FDT image that barely disconnects the two objects in the FDT image. Essentially, the FDT threshold indicates the radius of the optimal erosion operator partially separating the two cylinders as in Figure 2.1(b). The immediate next question is how to proceed with the separation to next lower scales. The difficulty here is that the scale of the annular remainder (Figure 2.1(b)) of the morphological erosion is at least equal to that of the regions not yet separated. This difficulty is overcome using a proposed morphological reconstruction operation that fills the annular remainder while maintaining the separate identities of the two objects (Figure
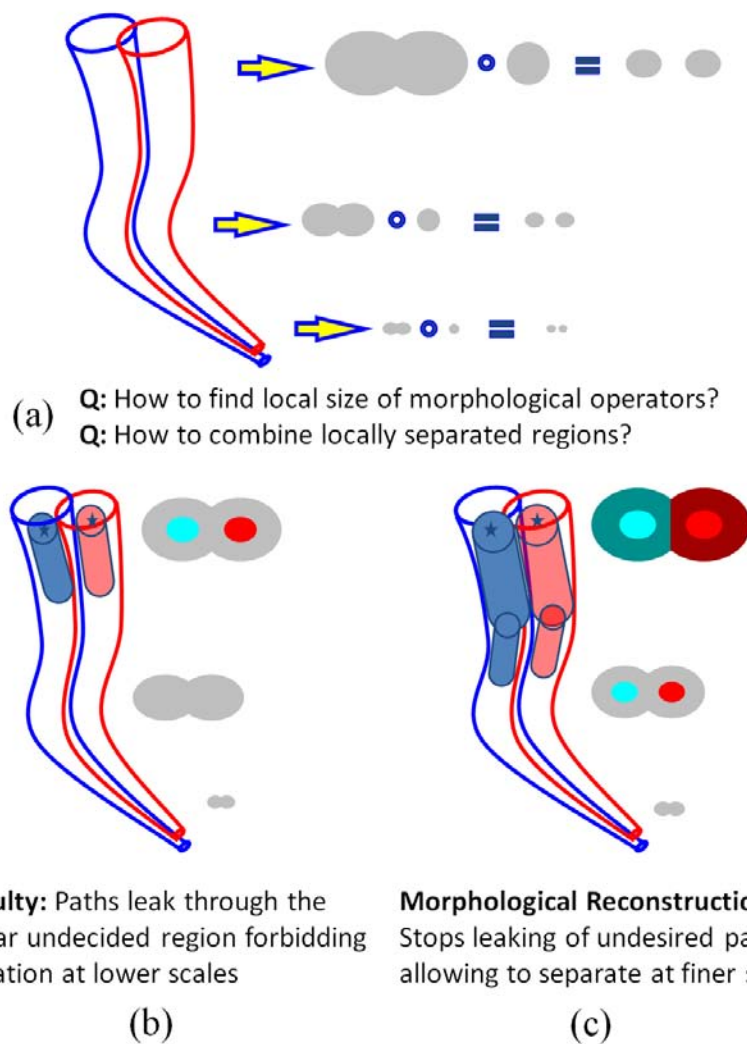
Figure 2.1: A schematic description of the artery/vein separation problem and its solution using a multi-scale topo-morphologic opening algorithm. Fundamental challenges and their solutions at different steps of the algorithm are mentioned and illustrated graphically. Hollow dots in (a) represents a morphological opening operator. See text for further details.
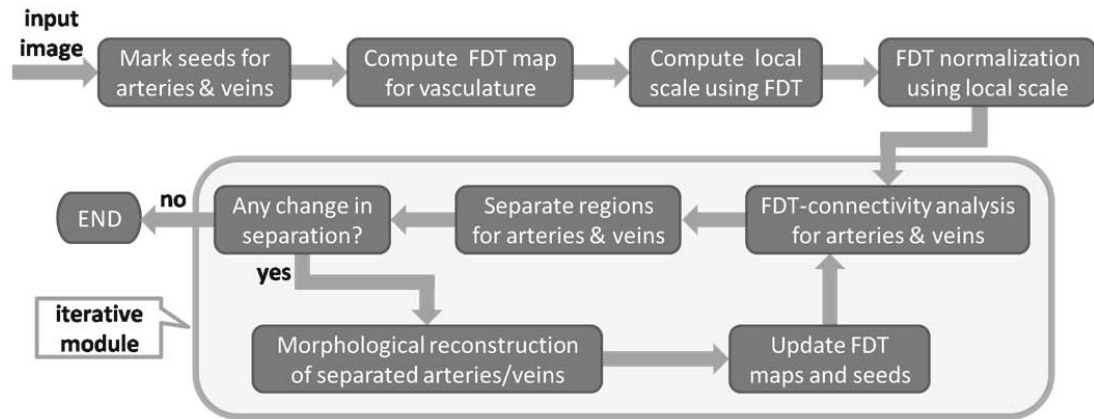
Figure 2.2: A modular representation of the multi-scale topo-morphologic opening algorithm separating two iso-intensity objects fused at different scales and locations.

2.1(c)). This step allows proceeding with separations at a lower scale and the method progresses iteratively separating fused structures at finer and finer scales starting with the larger one. In short, the method may be summarized by the following three steps:

Step 1: Compute normalized FDT of the assembly of two mutually fused structures (see Figure 2.3(c)).

Step 2: Find the optimum morphological opening structure scale separating the two objects specified by two sets of seeds (see Figure 2.1(b) and Figure 2.32(d)).

Step 3: Block the annular remainder around currently separated regions enabling morphological separations at lower scales (see Figure 2.1(c) and Figure 2.3(e)).

Step 4: Repeat Steps 2 & 3 until convergence.

The overall workflow diagram of the proposed method is presented in Figure 2.2. As input, it receives fuzzy segmentation of the assembly of two iso-intensity objects and two sets of seeds - one for each object - and it outputs the separated

objects. Although the method immediately extends to multiple objects, here we formulate a solution for two objects only and we will refer to one object as the "rival" of the other. Let us consider an image consisting of two iso-intensity fuzzy objects with significant noise and overlap at different scales as shown in Figure 2.3(a); a few cross sectional images are shown in Figure 2.3(b). The two cylinders with gradually reducing radii are running in parallel. The diameter of one cylinder is significantly larger than that of the other; a sinusoidal swing is added to both cylinders in the xy-coordinate direction so that centerlines of both cylinders lie on one xy-plane, say the central xy-plane. Usefulness of the method may be better understood in three and higher dimensions. On the other hand, it is always easier to illustrate a method in 2D. Therefore, we show results of different steps of the method on the central xy-plane first. One seed is identified at the approximate center of each cylinder at the top-most cross-section. As shown in Figure 2.2, the process is iterative and begins with marking the seeds followed by fuzzy distance transform computation [134] of the assembly of two cylinders prior to iterations; see Figure 2.3(c) for the results of FDT computation. It is visually notable from the FDT image that we cannot find a single FDT threshold to separate the two cylinders from their head to tail. Therefore, no straightforward morphological opening operator can solve the problem. On the other hand, over a small region, the two cylinders are separable using their FDT values. In other words, the problem demands regional selection of optimal opening structures to separate the two cylinders.

The above observation motivated us to use local scale to normalize FDT values.

This approach reduces the effect of spatial scale variations. Local scale at a point p is defined as the FDT value of the locally-deepest point (a point with locally maximum FDT value) that is nearest to p. With the normalized FDT map, the method adopts an iterative strategy that first separates the cylinders over large-scale regions using FDT-based relative connectivity [159, 126] where a point becomes associated with an object if its connectivity to the point is strictly greater than that of its rival. A separator is built between the two objects using a morphological reconstruction method that simultaneously and radially dilates each currently segmented region until blocked by its rival (maximum radius of the dilating structure is determined by FDT values). Figure 2.3(d,e) shows the results of initial separation and morphologic reconstruction of two cylinders after the first iteration. In the next iteration, the FDT-connectivity paths of one object are not allowed to enter into the region already assigned to its rival. This strategy facilitates object separation at smaller scale regions (Figure 2.3 (f)). The iterative process is continued as long as any change is detected step-to-step. For this phantom image, the method stopped after 12 iterations (see Figure 2.3(g-i) for final separation). In the remainder of this section, we formally describe the theory and algorithms.

2.3.1 Local Scale and FDT Normalization

Intuitively, "local scale" at a point p is defined as the FDT value (or, the ordinary distance transform [9] value for binary images) at the locally-deepest point that is nearest to p. Toward this aim, we first define "nearest point" as follows. Let $S \subset \Theta(\mathcal{O})$ denote a set of points and let $p \in \Theta(\mathcal{O})$ be a point inside the support of a
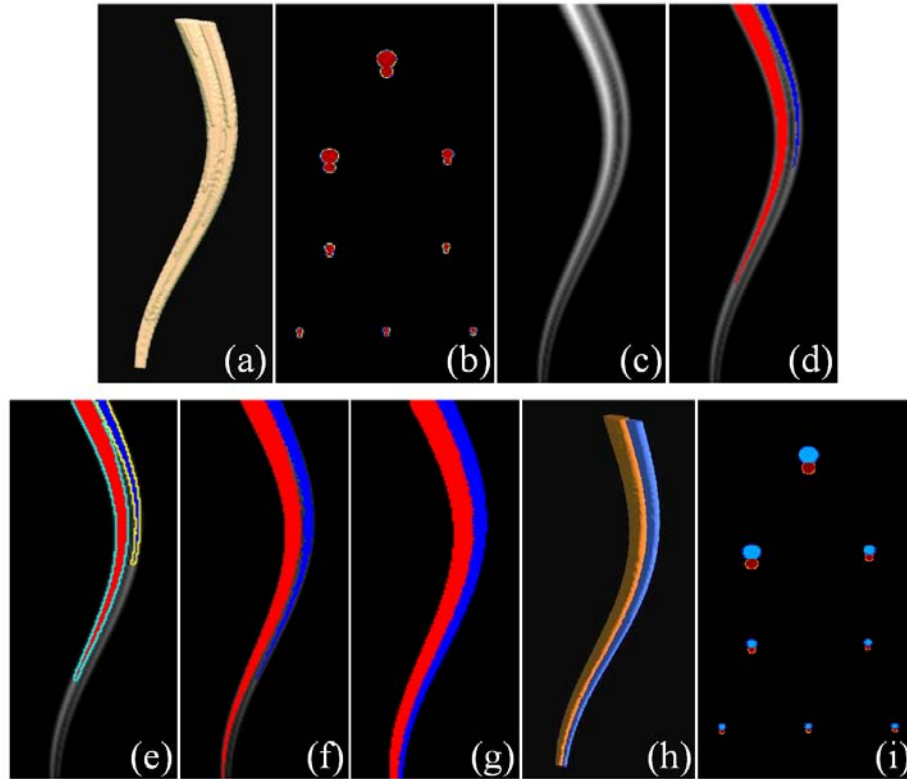
Figure 2.3: Illustration of intermediate results at different steps of the multi-scale topo-morphologic opening. (a) 3D rendition of a computer-generated phantom representing two iso-intensity objects fused at various scales and locations. (b) A few cross-sectional images of the phantom. (c) FDT image on the central xy-plane. Intuitively, it is a union of two FDT maps, one for each cylinder. Although the cylinders are locally separable in the FDT image, no global thresholding serves the purpose. (d) Results of separation of two cylinders after first iteration using FDT-based connectivity. (e) Morphologic reconstruction on the result shown in (d). Regions marked in cyan (or yellow) represents the expansion of the red (respectively, blue) object after morphological reconstruction. (f, g) Same as (d) after second (f) and terminal (g) iterations. (h,i) 3D rendition and cross-sectional images of the final result.

fuzzy object $\mathcal{O}$. The *nearest point* of p in S over an object $\mathcal{O}$, denoted by $NP_{\mathcal{O}}(p, S)$, is the point $q \in S$ such that, $\forall r \in S$, $\omega_{\mathcal{O}}(p, q) \leq \omega_{\mathcal{O}}(p, r)$; in case there are multiple such q's, the point with the largest FDT value is chosen. Let $S_{\max} \subset \Theta(\mathcal{O})$ be the set of points with locally maximal FDT values in $\mathcal{O}$, i.e., $S_{\max} = \{p | p \in \Theta(\mathcal{O})$ and $\forall q \in \mathcal{N}_l(p), \Omega_{\mathcal{O}}(q) \leq \Omega_{\mathcal{O}}(p)\}$, where $\mathcal{N}_l(p)$ is the $(2l + 1) \times (2l + 1) \times (2l + 1)$ neighborhood of p; in this paper, we have used $\mathcal{N}_2(p)$ to avoid noisy local maxima. Finally, *local scale* at a point p in an object $\mathcal{O}$, denoted by $\delta_{\mathcal{O}}(p)$, is defined as the FDT value of the local maximal point nearest to p, i.e. $\delta_{\mathcal{O}}(p) = \Omega_{\mathcal{O}}(NP_{\mathcal{O}}(p, S_{\max}))$.

In order to reduce the effects of spatial variation in object scales, we normalize the FDT value at each point p by dividing the original FDT value by the local scale, i.e., dividing $\Omega_{\mathcal{O}}(p)$ by $\delta_{\mathcal{O}}(p)$. Note that the normalized FDT values always lie in the interval [0,1]. This step of normalizing the FDT value is simple yet effective in reducing the artifacts of scale variation in an object. Although this step causes no change in the FDT map for phantom images where local radii change monotonically along the axis of each structure (see Figure 2.3(c)), it is useful when local radii vary non-monotonically along an object (e.g., arteries and veins in Figure 2.14(d) and Figure 2.15(d)). Essentially, FDT normalization is equivalent to equating the height of all local maxima of the original FDT map. It can be shown that, by this process, all local minima and valley lines of the original FDT map are preserved and may thus be exploited as separating features by the multi-scale topo-morphologic opening algorithm. Therefore, all separations of the original FDT map will be preserved in the normalized FDT map. The major advantage of the FDT normalization is that it

reduces the number of iterations in most real applications. In the rest of this paper, by "FDT" we will refer to the "scale-normalized FDT" and $\Omega_{\mathcal{O}}(p)$ will denote the scale normalized FDT value at p unless stated otherwise.

2.3.2 Fuzzy Morpho-Connectivity

This step is essentially the same as used when determining the fuzzy connectivity [111, 160] except that the FDT values are used instead of the intensity values. We follow the formulation of fuzzy connectivity method introduced by Rosenfeld [111]. *Fuzzy morpho-connectivity strength* of a path $\pi = \langle p_1, p_2, \cdots, p_l \rangle$ in a fuzzy object $\mathcal{O}$, denoted by $\Gamma_{\mathcal{O}}(\pi)$, is defined as the minimum FDT value along the path:

$$\Gamma_{\mathcal{O}}(\pi) = \min_{1 \leq i \leq l} \Omega_{\mathcal{O}}(p_i). \tag{2.7}$$

A path $\pi_{p,q} \in \mathcal{P}(p,q)$ is one of the *strongest morphological paths* from p to q, if and only if, $\Gamma_{\mathcal{O}}(\pi_{p,q}) \geq \Gamma_{\mathcal{O}}(\pi), \forall \pi \in \mathcal{P}(p,q)$. The *fuzzy morpho-connectivity* between two points $p \in \mathbb{Z}^3$ and $q \in \mathbb{Z}^3$, denoted by $\gamma_{\mathcal{O}}(p,q)$, is the strength of one of the strongest morphological paths between p and q:

$$\gamma_{\mathcal{O}}(p,q) = \max_{\pi \in \mathcal{P}(p,q)} \Gamma_{\mathcal{O}}(\pi). \tag{2.8}$$

Intuitively, fuzzy morpho-connectivity between two points $p, q \in \mathbb{Z}^3$ indicates the size of the morphological erosion operator that barely disconnects the two points.

2.3.3   Object Region Detection

This step is accomplished by comparing the fuzzy morpho-connectivity values for the two target objects $\mathcal{A}$ and $\mathcal{B}$ similar to that presented in [159, 126, 22]. Specifically, the region acquired by $\mathcal{A}$, denoted as $R_{\mathcal{A}}$, is defined as

$$R_{\mathcal{A}} = \left\{ p | \max_{a \in S_{\mathcal{A}}} \gamma_{\mathcal{A}}(a, p) > \max_{b \in S_{\mathcal{B}}} \gamma_{\mathcal{B}}(b, p) \right\}, \tag{2.9}$$

where $S_{\mathcal{A}}$ and $S_{\mathcal{B}}$ are the sets of seeds for objects $\mathcal{A}$ and $\mathcal{B}$, respectively. It may be noted that we need to specify the FDT maps $\Omega_{\mathcal{A}}$ and $\Omega_{\mathcal{B}}$ for the two objects $\mathcal{A}$ and $\mathcal{B}$ in order to complete the definition of $R_{\mathcal{A}}$ and similarly the definition of $R_{\mathcal{B}}$. In this paper, at the beginning of the algorithm, the two FDT maps $\Omega_{\mathcal{A}}$ and $\Omega_{\mathcal{B}}$ are both assigned to the FDT map computed from the assembly of the two fuzzy objects. However, the theory and algorithms work equally well even if we initiate the algorithm with two different FDT maps computed from two different representations of the assembled objects, each representation emphasizing one over the other. It allows taking advantage of features that partially distinguish the two objects. After every iteration, the values of $\Omega_{\mathcal{A}}$ and $\Omega_{\mathcal{B}}$ are updated following the strategy described in Section 2.3.5.

2.3.4   Morphological Reconstruction

Two regions $R_{\mathcal{A}}$ and $R_{\mathcal{B}}$, defined in the previous section, provide a separation of the two objects based on fuzzy morpho-connectivity analysis; an output of this step is illustrated in Figure 2.1(b) and Figure 2.3(d). The idea is to morphologically

extend the two separated regions $R_\mathcal{A}$ and $R_\mathcal{B}$ to fill the annular space around them without compromising their separation; results of this step are illustrated in Figure 2.1(c) and Figure 2.3(e). In order to define the morphological reconstruction process, we first introduce the notion of "morphological neighborhood". The *morphological neighborhood* of a set of points X in an object $\mathcal{O}$, denoted by $N_\mathcal{O}(X)$, is a set of all points $p \in \Theta(\mathcal{O})$ such that for some $q \in X$, $\omega_\mathcal{O}(p,q) < \Omega_\mathcal{O}(q)$ and p is connected to q by a path $\pi = \langle p = p_1, p_2, \cdots, p_l = q \rangle$ of monotonically increasing FDT values. It may be noted that the original FDT map is used here without scale normalization as morphological neighborhood is defined on the basis of original geometry and size of a local structure. Finally, $R_\mathcal{A}$ (or $R_\mathcal{B}$) is extended by the set of points $p \in N_\mathcal{O}(R_\mathcal{A})$ (respectively, points $p \in N_\mathcal{O}(R_\mathcal{B})$) which are strictly closer to $\mathcal{R}_\mathcal{A}$ (respectively, $R_\mathcal{B}$) than $R_\mathcal{B}$ (respectively, $R_\mathcal{A}$). Results of this step are illustrated in Figure 2.1(c) and Figure 2.3(e). It may be noted that, gaps between the separated regions visible in Figure 2.3(d) are filled in Figure 2.3(e) after the morphological reconstruction. This step is important as it stops paths running through those gaps that would be creating problems during separation of smaller scale regions in subsequent iterations. Let $M_\mathcal{O}(R_\mathcal{A})$ and $M_\mathcal{O}(R_B)$ represent morphological reconstructions for $R_\mathcal{A}$ and $R_\mathcal{B}$, respectively.

2.3.5   Modification of FDT Maps and Seeds

This step is similar to the iterative strategy described in [126, 22] for intensity based fuzzy connectivity. For each of the objects, we set the FDT values to zeros over the region currently acquired by its rival object. This step stops paths from one

object to run through the acquired territory of its rival object. Thus, a hypothetical wall is created between the two regions currently separated. Specifically, the FDT images of the object $\mathcal{A}$ are updated after each iteration as follows:

$$\Omega_{\mathcal{A}}(p) = \begin{cases} 0, & \text{if } p \in N_{\mathcal{O}}(R_{\mathcal{B}}) - M_{\mathcal{O}}(R_{\mathcal{A}}), \\ \\ \Omega_{\mathcal{O}}(p), & \text{otherwise.} \end{cases} \tag{2.10}$$

The FDT map of the other object is updated similarly. The seeds $S_{\mathcal{A}}$ and $S_{\mathcal{B}}$ for the two objects are replaced by $\mathcal{R}_{\mathcal{A}}$ and $\mathcal{R}_{\mathcal{B}}$, respectively. With this set-up, the algorithm enters into the subsequent iteration, i.e., steps described in Sections 2.3.2–2.3.5 are restarted.

2.3.6   Local Update with an Effective User Interface

A composite 2D and 3D user interface has been developed allowing to simultaneously view 2D and 3D vascular geometry along with current results of A/V separation overlaid in different colors (see Figure 2.4). The correspondence of vascular geometry in 3D and three planar views is realized by tagging the 3D cursor with 2-D planar cursors indicated with color-matched orthogonal lines. Facilities to select and edit different seeds and separators are supported within the graphical interface along with various display and overlay related options. A major challenge with the development of the graphical user interface is the time required (approximately 2-3 minutes for a $512 \times 512 \times 600$ CT image of a human lung in a 2.33 GHz intel(R) Xeon(R) CPU running under Linux operating system) to update the A/V separation result in the entire image prohibiting interactive editing of seeds. On the other hand,
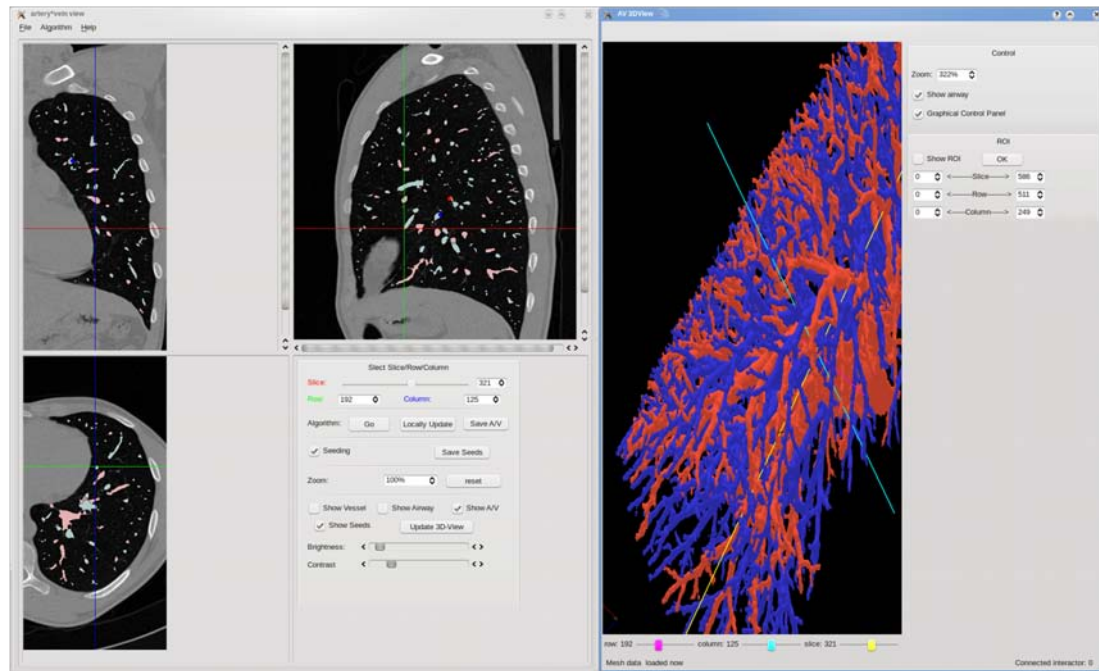
Figure 2.4: 2D/3D graphical interface. The left side includes 2D display and main operations, including basic display options, overlay options, add/delete seeds and local/global update process of A/V separation. The right side shows the 3D display, with the cursor connected with the 2D display to guide seed selection

a user is often interested in the local updates of A/V separation during the selection or deletion of a seed or a separator. It encouraged us to develop the theory and algorithm for local updates facilitating user interface. The basic idea is to confine the A/V separation over a small local window of size, say, $51 \times 51 \times 51$ so that a user may view local changes in A/V separation at an interactive speed while editing with seeds and separators. After several edits a user may ask for a global update of A/V separation before entering for another round of editing if needed. It is important to make the following two observations to understand the challenges as well as the solution for the local update algorithm.

(1) The local window inherits some A/V separation results from prior selected seeds possibly outside the local space (see Figure 2.5(b)).

(1) A/V separation inside the box needs to be partially or fully overruled with selection or deletion of seeds and separators.

The first observation suggests that we need to inherit some seeds in the local space based on global results of A/V separation. On the other hand, if all voxels marked as arteries (or, veins) are considered as seeds, the algorithm fails to overrule faulty segmentations inside the local space. Therefore, the aim is to use minimum sets of seeds to inherit the global A/V separation in the local space. It may noted that any branch of an artery or vein must cross the outer surface of the local space to enter inside and therefore, regions of intersection between global separated arteries (or, veins) and the ourter surface of the local space may be used to inherit seeds for arteries (respectively, veins) during local updates; these seeds will be referred to
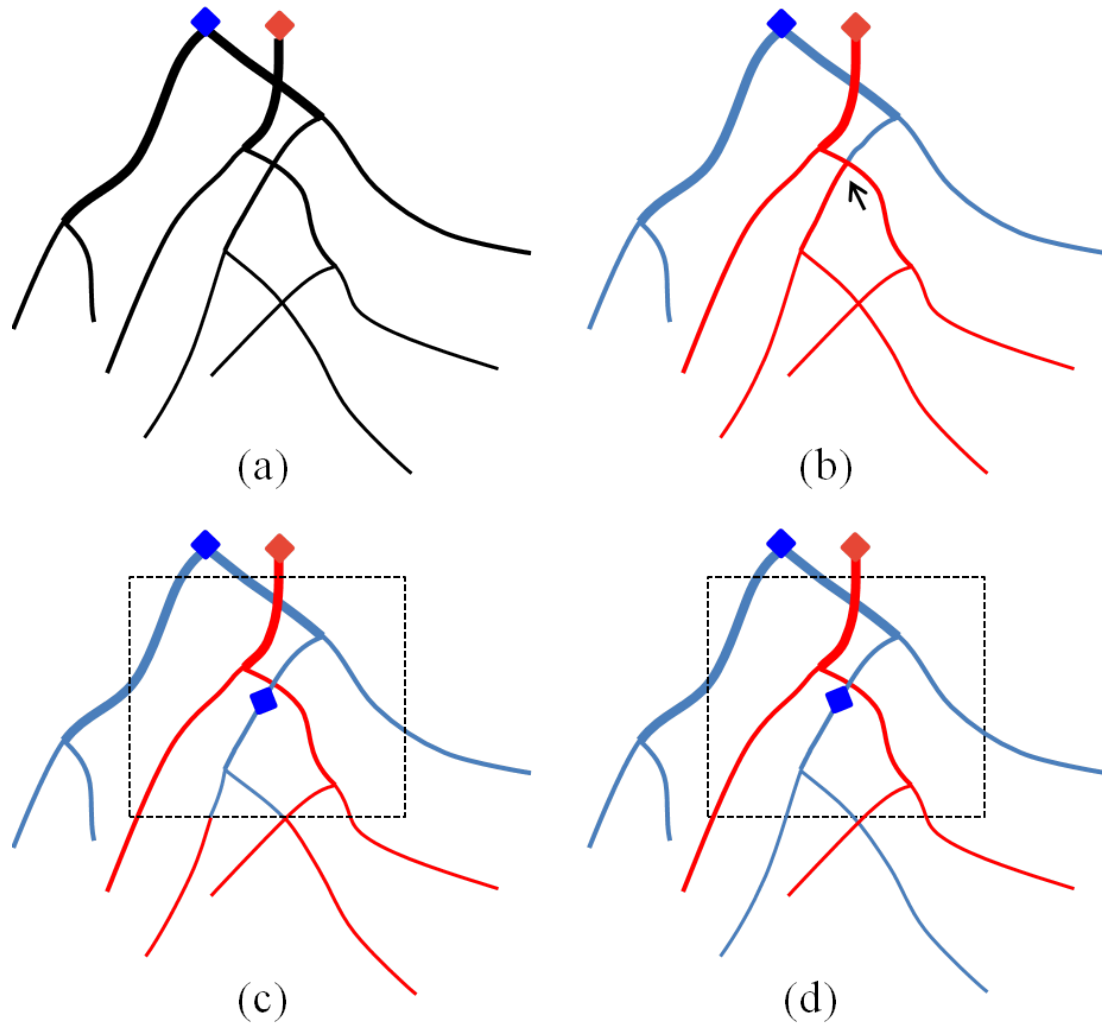
Figure 2.5: Illustration of the idea of local update. (a) Vessel structures without artery/vein identity, one seed for artery and another for vein are selected. (b) Artery and vein cannot be separated well with those two seeds. (c) In the local space, an additional seed for artery has been selected. After locally update, artery and vein can be separated in the local space. (d) Result after golbal update

as inherited seeds. User-specified seeds falling inside the local space are also used in conjunction with inherited seeds for local updates. Further, in an attempt to eliminate adverse effects of inherited seeds, an inherited seed is eliminated if it falls inside the morphological neighborhood of a user-specified seed, probably, a new one. Let us consider the example of Figure 2.5. Here, the image are displayed in 2D, although, the structures are imaged in 3D. Figure 2.5(a) shows the original vasculature along with two seeds — one for arterial tree and another for venous tree. The result of global A/V separation using the initial seed is shown in Figure 2.5(b). Note that the branch indicated by an arrow is falsely grabbed by venous tree and an user interaction is needed here. As the user put an arterial seed to rectify the error, a local update process is invoked. It starts with defining a local space. The Space enclosed by the rectangle as shown in Figure 2.5(c), with the new added seed as the center. After the local update precess, artery/vein trees are separated correctly in local space but the connected arterial/venous structure in the whole image are not updated immediately, as shown in Figure 2.5(c). In order to get the new separated arterial/venous trees, a global update preocess is needed, which takes more times.

2.3.7 Algorithms

Algorithms for computing fuzzy distance transform and fuzzy connectivity have been presented in several papers including [132, 160, 126, 134]. The algorithmic solutions for local scale computation, FDT normalization, object region detection and modification of FDT maps and seeds are trivial following their descriptions in Sections 2.3.1, 2.3.3 and 2.3.5. However, the algorithmic realization of morphologi-

cal neighborhood computation in the context of morphological reconstruction is not straightforward from the descriptions in Section 2.3.4. Therefore, a pseudo code for the algorithm of computing morphological neighborhood is presented in the following.

begin compute-morphological-neighborhood

input:

a set of points X

a fuzzy object $\mathcal{O} = \{(p, \mu_\mathcal{O}(p))|p \in \mathbb{Z}^3 \text{ and } \mu_\mathcal{O} : \mathbb{Z}^3 \to [0,1]\}$

original FDT map $\Omega_\mathcal{O}(p) : \mathbb{Z}^3 \to \mathfrak{R}^+$ without scale normalization.

output:

morphological neighborhood $N_\mathcal{O}(X)$

auxiliary data structure

monotonic distance transform map $\xi_\mathcal{O}(p) : \mathbb{Z}^3 \to \mathfrak{R}|\mathfrak{R}$ is the set of all real numbers

a sequential queue Q

for each point $p \in \mathbb{Z}^3$

assign $\xi_\mathcal{O}(p) = 0$

for each point $p \in X$

assign $\xi_\mathcal{O}(p) = -\Omega_\mathcal{O}(p)$

push p in Q

while Q is not empty

pop a point p from Q

for each point $q \in \mathcal{N}^*(p)$ and $\Omega_\mathcal{O}(q) < \Omega_\mathcal{O}(p)$

assign $link(p,q) = \frac{1}{2}(\mu_\mathcal{O}(p) + \mu_\mathcal{O}(q)) \times \|p - q\|$

$$\textbf{if } \xi_{\mathcal{O}}(q) > \xi_{\mathcal{O}}(p) + link(p, q)$$

$$\text{assign } \xi_{\mathcal{O}}(q) = \xi_{\mathcal{O}}(p) + link(p, q)$$

$$\text{push } q \text{ in } Q$$

$$N_{\mathcal{O}}(X) = \{p|p \in \mathbb{Z}^3 \text{ and } \xi_{\mathcal{O}}(p) < 0\}$$

end compute-morphological-neighborhood

2.4 Experimental Methods and Results

As outlined in the second specific aim in Chapter 1, the overall objective of our experimental plan is to examine the accuracy, reproducibility, and efficiency of our artery/vein separation algorithm. Specifically, the accuracy of the algorithm is evaluated using — (1) computerized mathematical phantoms with and without bifurcations, (2) CT images of a pig pulmonary vessel cast phantom, and (3) non-contrast pulmonary CT images of human subjects. Reproducibility of the method is evaluated using - (1) contrast-enhanced CT images of a pig lung at different respiratory volumes and (2) multi-user A/V separations in non-contrast pulmonary CT images of human subjects. Finally, the efficiency of the method is examined by studying the relation between the number of user-specified seeds and achieved accuracy. In following sections, I will describe experimental methods to evaluate accuracy, reproducibility, and efficiency of our method.

2.4.1   Accuracy

In this section, I present experimental plans and results to evaluate the accuracy of the A/V separation method. Following the difficulties in generating ground truths for *in vivo* pulmonary images in human subjects, we have designed our experimental plans to examine accuracy of out A/V separation algorithm using phantoms. We have used several computer generated mathematical phantoms along with a physical phantom generated by casting arterial and venous trees in a pig lung. Two types of mathematical phantoms have been created to evaluate the performance of the method under two different conditions. The first group of phantoms contains a pair of quasi-parallel tubular objects with different geometry of mutual coupling while the second group of phantoms was designed to evaluate the performance of the method in the presence of bifurcations and different levels of partial overlaps. A physical phantom was created from a pig lung with different CT contrast materials for venous and arterial trees to generate ground truths for the A/V separation problem.

2.4.1.1   Computer Phantoms with no Bifucation

Performance of the method has been examined both qualitatively and quantitatively on mathematically generated phantoms (Figures 2.3 and 2.6). Six mathematical phantoms were computer-generated, each being an assembly of a pair of tubular objects running quasi-parallel across the slice direction with different levels of fuzziness, overlap, scale and noise. Initially, the phantom images were generated at high resolution and then down-sampled using $3 \times 3 \times 3$, $4 \times 4 \times 4$ and $5 \times 5 \times 5$ windows to simulate different resolutions and partial volume effects. Each down-
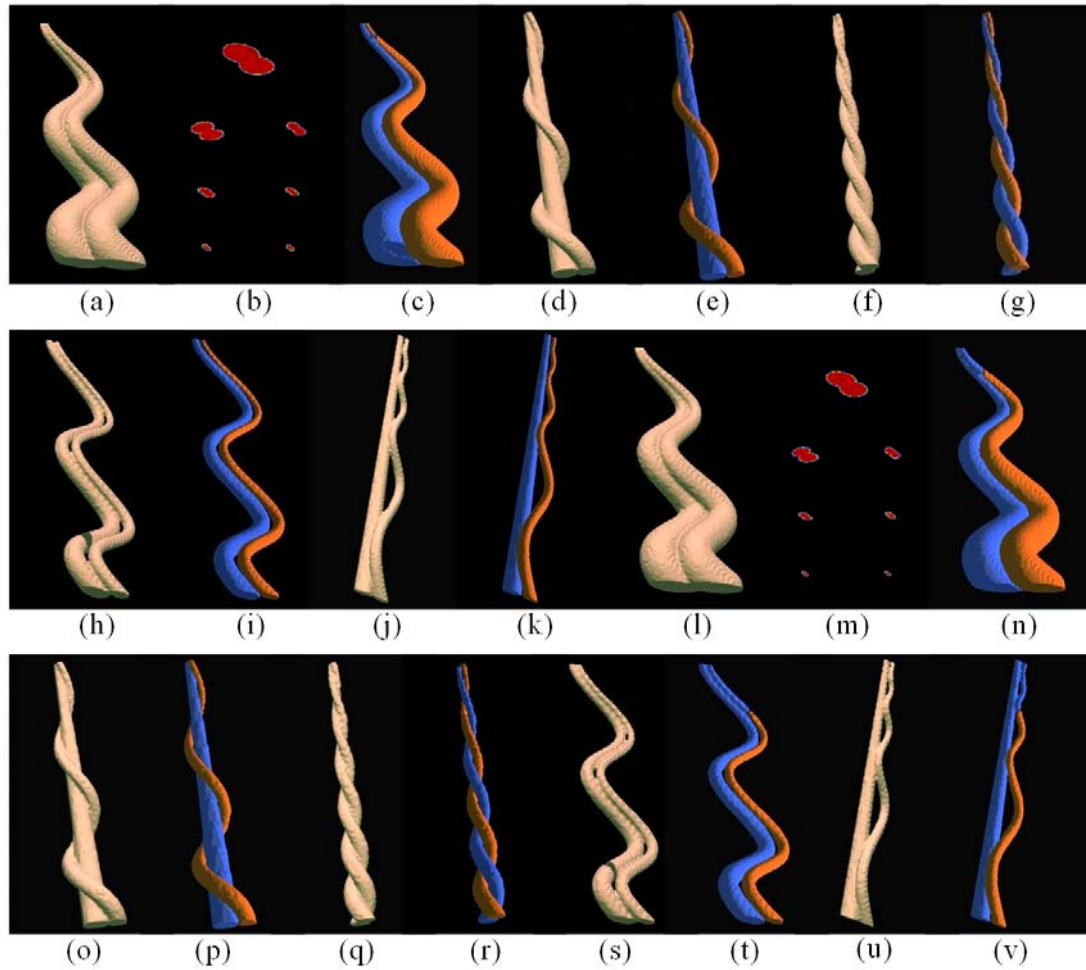
Figure 2.6: Results of applying our method to several computer-generated 3D phantoms. (a-k) Results of phantoms after $4 \times 4 \times 4$ down sampling. (a,b) 3D rendition and cross-sectional images of one phantom. (c) Separated cylinders. (d-k) Results for other four phantoms. (l-v) Results of application of the method after $5 \times 5 \times 5$ down sampling. Note that this level of down sampling makes separation impossible for smallest-scale features in phantom (l, s, u).

sampled image was further degraded with additive random noise at SNR of 12. Using a graphical user interface, exactly two seed points were manually selected for each phantom. One seed was placed for each tubular object near its center on the slice at the largest-scale level. Although there is no theoretical restriction on positioning the seed points, the seeds were positioned visually close to the centerline of each cylinder. Example phantoms and their object-separation results are depicted in Figure 2.6 at $4 \times 4 \times 4$ and $5 \times 5 \times 5$ down-sampling only, as the method has always successfully separated the two cylinders at $3 \times 3 \times 3$ down-sampling. The phantom image of Figure 2.3 was generated at $4 \times 4 \times 4$ own sampling. At extremely low resolution and high noise, the morphological information may be entirely lost at a few locations leading to a failure of separations as shown in Figure 2.6(n, t, v). Specifying another pair of seeds at each of those locations would have helped achieving correct separations. Cross-sectional images of the first phantom are given at both resolutions to demonstrate the 3D phantom image quality used and the complexity of separating the two objects. The smallest radius of the phantom shown in Figure 2.6(a) is 1.87 pixels after down-sampling by $4 \times 4 \times 4$ pixels; the largest radius in the same example at the same down-sampling resolution is 18.75 pixels. Except for the examples of Figure 2.6(a,f), the radii of the two cylinders differed significantly. It may be noticed that at the upper part of the object colored in red in Figure 2.6(c), the object visually appears disconnected. We confirm that each of the red and blue objects in Figure 2.6 has been explicitly checked by a computerized algorithm and found to be a single connected component as expected according to the presented theory of the method.

A quantitative analysis was performed on the six phantoms images of Figure 2.3 and Figure 2.6. For this purpose, the ground truth of separations of two objects in those phantoms was generated from the knowledge of their generation at the original resolution prior to down sampling. For each tubular object in a phantom, its center-line along with local radii was recorded at the time of its computerized generation. Let $(c_{i,j}, r_{i,j})|i = 1, 2; j = 1, 2, \cdots, L_i$ be the set of points and local radii along the centerline of the ith object in a phantom prior to down sampling. Let $p = (x, y, z)$ be a point with non-zero intensity value in the corresponding phantom image obtained by down sampling at $l \times l \times l$ where $l = 4$ or 5. Local-radius-normalized distance of p from the centerline of the ith object, denoted by $D_i(p, l)$, is defined as follows:

$$D_i(p, l) = \min_{j=1,2,\cdots,L_i} \frac{\|(xl, yl, zl), c_{i,j}\|}{r_{i,j}}. \qquad (2.11)$$

Here, local-radius-normalized distance is used to avoid a bias in separation due to local radius difference between two objects. Finally, in the true separation of two objects, the point p is assigned in the first object (or, the second object) if $D_1(p, l) < D_2(p, l)$ (respectively, $D_2(p, l) < D_1(p, l)$). Note that in a rare situation of $D_1(p, l) = D_2(p, l)$ (since, $c_{i,j}$ is the point in Euclidean 3D-space), the point is not assigned to any of the two objects.

Let T_1 and T_2 denote true segmentations of the two objects in a phantom image computed as above and let S_1 and S_2 denote the segmentations of corresponding objects in the same phantom image computed by the current method. *True positive*

and *false negative* of the computerized separation of two objects are defined as follows:

$$True \ \ Positive = \frac{(T_1 \cap S_1) \cup (T_2 \cap S_2)}{T_1 \cup T_2}, \tag{2.12}$$

$$False \ \ Negative = \frac{(T_1 \cap S_2) \cup (T_2 \cap S_1)}{T_1 \cup T_2}. \tag{2.13}$$

Results of quantitative analysis of true positive and false negative of separation of two tubular objects in each phantom image at different down sampling rates using our algorithm are presented in Table 2.1. These results demonstrate that our method produces high accuracy in spatially delineation of the two structures while its performance in terms of maintaining the identity of individual structures along their axes is qualitatively illustrated in Figures 2.3 and 2.6.

Table 2.1: Results of quantitative analysis of true positive and false negative separations of two objects using our multi-scale topo-morphologic opening algorithm for different phantom images at different down sampling rates.

Phantoms	Down-sampling rate=4		Down-sampling rate=5	
	True positive	False negative	True positive	False negative
Fig.2.3(a)	98.00%	0.70%	93.72%	5.06%
Fig.2.6(a)	99.11%	0.45%	98.64%	0.74%
Fig.2.6(d)	98.78%	0.45%	98.36%	0.65%
Fig.2.6(f)	98.43%	0.50%	97.98%	0.50%
Fig.2.6(h)	97.54%	1.79%	97.45%	1.78%
Fig.2.6(j)	99.23%	0.28%	96.49%	2.82%
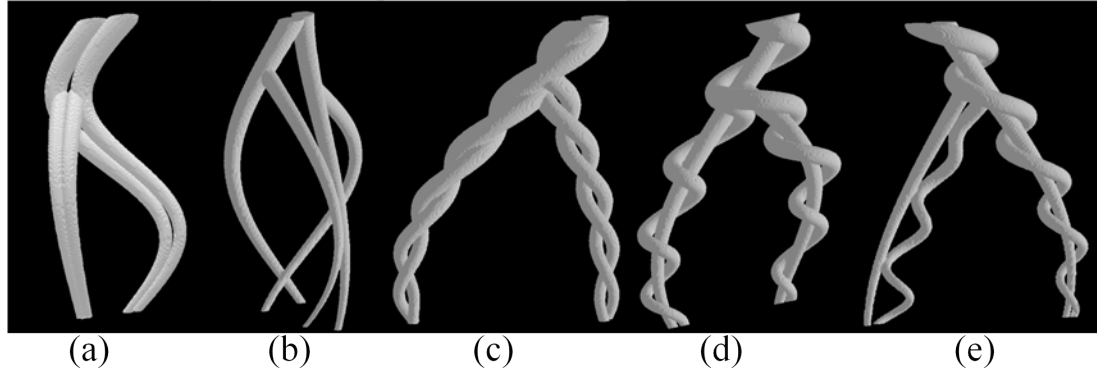
Figure 2.7: 3D rendition of five computer generated phantoms with bifurcation at 25% overlap and $4 \times 4 \times 4$ downsampling used in our experiments

2.4.1.2   Computer Phantoms with a Bifurcation

In this section, I present our experimental plans and methods related to evaluation of the A/V separation method based on mathematical phantoms generated as an assembly of a pair of tubular tree objects running across the slice direction with different levels of fuzziness, overlap, scale and noise. We have generated five base phantoms(Figure 2.7) with different geometry at the bifurcation. From each base phantom, we generated four different phantoms at different overlaps (see Figures 2.8(a,g,m,s)) by bringing the two tubular tree structures closer. The overlap factor is computed as follows. Following the same approach discussed in Section 2.4.1.1, a tubular tree in a phantom image may be represented using the centerline of a tree structure along with the radius associated to each location on the centerline. Let us assume that a phantom image contains two tubular objects denoted as follows:

$$A = \{(c_{1,1}, r_{1,1}), (c_{1,2}, r_{1,2}), \cdots, (c_{1,L}, r_{1,L})\}, \tag{2.14}$$
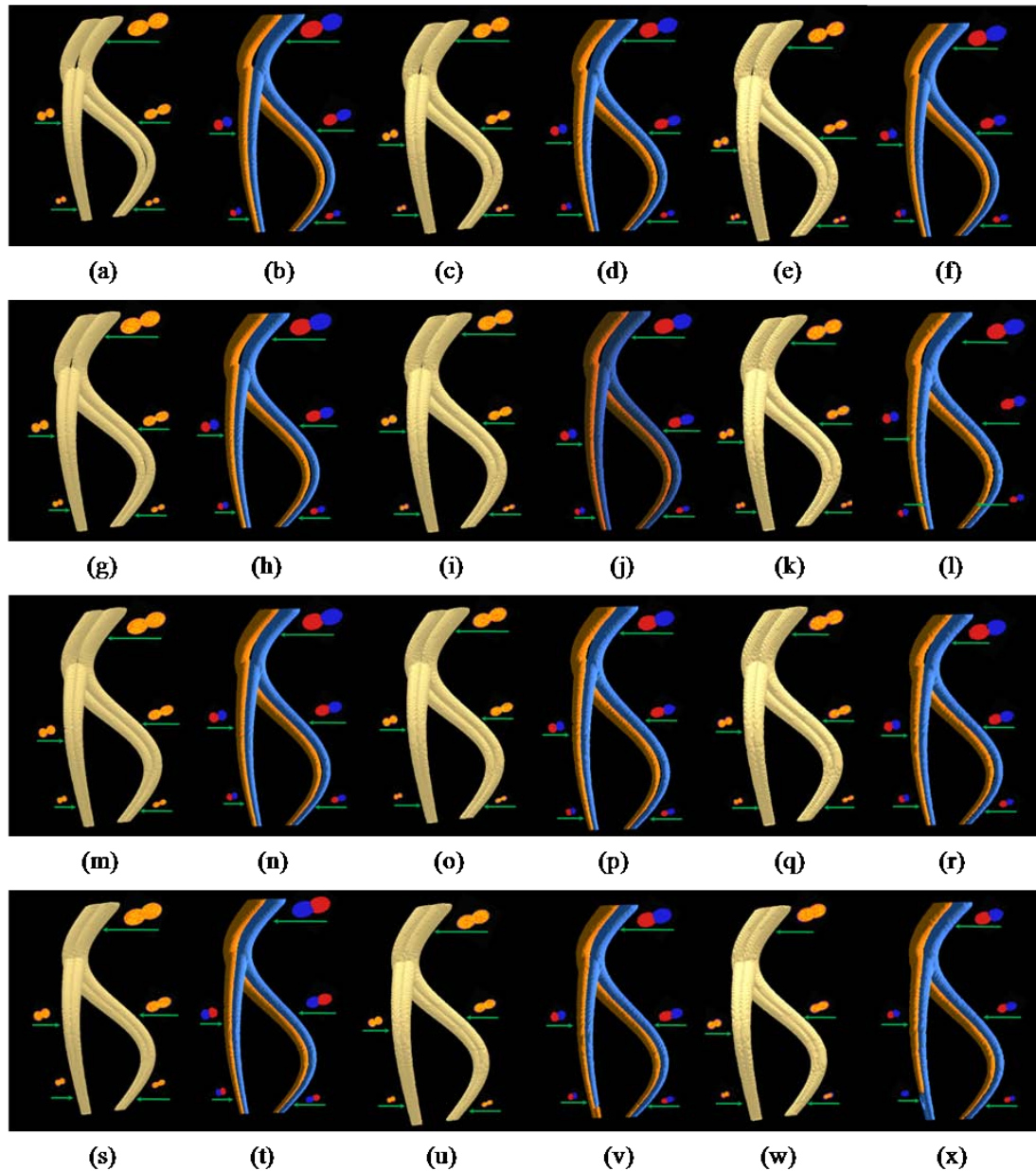
Figure 2.8: Results of applying our method to three computer-generated 3D phantoms. (a-f) Results of phantoms with 5% overlap at $3 \times 3 \times 3$ (a, b), $4 \times 4 \times 4$ (c, d) and $5 \times 5 \times 5$ (e, f) down sampling. (a,b) 3D renditions of the phantom images before (a) and after (b) applying topo-morphologic separations. On each image, several 2D cross sectional images are presented to illustrate relative overlap at various scales in different phantoms. (g-l), (m-r), (s-x) Same as (a-f) but for 10%, 15%, and 25% overlaps. At 25% overlap and $4 \times 4 \times 4$ and $5 \times 5 \times 5$ downsampling rate, the method has failed to sucessfully separate two objects at small scales

and

$$B = \{(c_{2,1}, r_{2,1}), (c_{2,2}, r_{2,2}), \cdots, (c_{2,M}, r_{2,M})\}. \tag{2.15}$$

The ratio of overlap between the two structures is defined as the maximum normalized overlap between the two structures in the entire image which is defined as follows:

$$Overlap(A, B) = \max_{i,j} \frac{r_{1,i} + r_{2,j} - |c_{1,i} - c_{2,j}|}{r_{1,i} + r_{2,j}}. \tag{2.16}$$

In the above equation, $|c_{1,i} - c_{2,j}|$ denote the Euclidean distance between two centers $c_{1,i}$ and $c_{2,j}$. Four phantoms were generated with the percent of overlaps of 5, 10, 15, and 25. Noisy phantoms at three different resolutions was generated from each phantom at a given overlap using the same approach described in Section 2.4.1.1. Thus, twelve test phantoms were generated for each base phantom with bifurcation producing a total of seventy-two test phantoms. Results of A/V separation on one base phantom at different overlaps and resolutions are presented in Figure 2.8. Quantitative results of Figure 2.8 show that, even in the presence of bifurcation, significant overlap, down sampling and random noise, the method can separated the two conjoined structure except at small scale regions in phantom with overlapping and downsampling. A similar trend is confirmed in results of other phantoms presented in Figure 2.9. The same protocol of quantitative analysis of of Section 2.4.1.1 was used to examine the performance of the method on phantoms with bifurcation. The Results of quantitative analyses are summarized in Tables 2.2, 2.3 and 2.4.The results demonstrated that, even in the presence of bifurcation, our method produces

high accuracy in spacial delineation of the two structures at different downsampling rates and different overlaps. The performance of our method deteriorates with increase overlaps of two structures as well as downsampling rate. As observed in our experimental results, with phantom data, most of the failure in separating two structures occurs at small scales due to relatively higher effects of noise and other image quality degrading artifacts at small scales. detonates
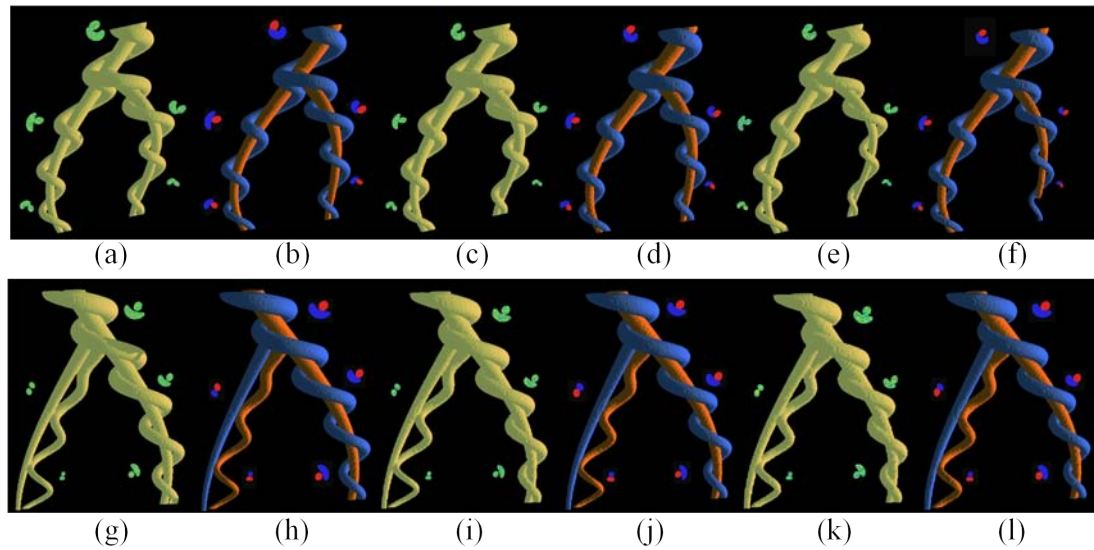
Figure 2.9: Results of applying our method to threee computer-generated 3D phantoms. (a)-(f) Results of phantoms with increasing overlap and downsampling rates — (a, b) 10% overlap and $3 \times 3 \times 3$ downsampling; (c, d) 15% overlap and $4 \times 4 \times 4$ downsampling; (e, f) 25% overlap and $5 \times 5 \times 5$ down sampling.(g-l)is the same as (a-f) but for another base phantom

2.4.1.3 Vessel Cast Phantom for a Pig Lung

To evaluate the performance of the method for complexity level present in pulmonary A/V trees of human subjects, we generated a vessel cast of a pig's lung

Table 2.2: Results (mean $\pm$ std) of quantitative analysis of true positive and false negative separations of computer generated phantoms with bifurcation using the proposed multi-scale topo-morphologic opening algorithm for different phantom images at down sampling rates $3 \times 3 \times 3$ and different overlaps.

Phantoms	True Positive	False Negative
Fig.2.7(a)	$97.80 \pm 1.85\%$	$0.63 \pm 0.30\%$
Fig.2.7(b)	$99.68 \pm 0.27\%$	$0.39 \pm 0.16\%$
Fig.2.7(c)	$99.35 \pm 0.34\%$	$0.47 \pm 0.26\%$
Fig.2.7(d)	$98.52 \pm 0.18\%$	$1.14 \pm 0.17\%$
Fig.2.7(e)	$99.29 \pm 0.30\%$	$0.45 \pm 0.23\%$

Table 2.3: Results (mean $\pm$ std) of quantitative analysis of true positive and false negative separations of computer generated phantoms with bifurcation using the proposed multi-scale topo-morphologic opening algorithm for different phantom images at down sampling rates $4 \times 4 \times 4$ and different overlaps.

Phantoms	True Positive	False Negative
Fig.2.7(a)	$97.26 \pm 2.1\%$	$1.03 \pm 0.65\%$
Fig.2.7(b)	$99.45 \pm 0.31\%$	$0.47 \pm 0.22\%$
Fig.2.7(c)	$99.18 \pm 0.41\%$	$0.50 \pm 0.27\%$
Fig.2.7(d)	$98.09 \pm 0.22\%$	$1.25 \pm 0.19\%$
Fig.2.7(e)	$98.92 \pm 0.34\%$	$0.54 \pm 0.26\%\%$

Table 2.4: Results (mean $\pm$ std) of quantitative analysis of true positive and false negative separations of computer generated phantoms with bifurcation using the proposed multi-scale topo-morphologic opening algorithm for different phantom images at down sampling rates $5 \times 5 \times 5$ and different overlaps.

Phantoms	True Positive	False Negative
Fig.2.7(a)	$96.34 \pm 2.50\%$	$1.46 \pm 1.03\%$
Fig.2.7(b)	$99.07 \pm 0.52\%$	$0.46 \pm 0.23\%$
Fig.2.7(c)	$98.81 \pm 0.54\%$	$0.56 \pm 0.28\%$
Fig.2.7(d)	$97.35 \pm 0.46\%$	$1.43 \pm 0.23\%$
Fig.2.7(e)	$97.27 \pm 1.10\%$	$1.78 \pm 1.08\%$

with different CT contrast materials for arterial and venous trees. To generate the vessel cast, the animal was first exsanguinated and then the pulmonary vasculature was flushed with 1L 2% Dextran solution and pneumonectomy performed while maintaining ventilation at low positive end-expiratory pressures (PEEP). Finally, a rapid-hardening methyl methacrylate compound (Orthodontic Resin, DENTSPLY International, York, PA) was injected into the vasculature to create a cast of the pulmonary arterial and venous trees while keeping the lungs inflated at approximately 22 cm H_2P_{awy}. The casting compound was mixed with red oil paint for the venous (oxygenated) side and blue oil paint for the arterial (deoxygenated) side of the vascular beds. The arterial side was also contrast-enhanced by the addition of 10 cc of Ethiodol (Savage Laboratories, Melville, NY) to the casting compound (Figure 2.10(a))[141]. The vessel cast was scanned in a Siemens sensation 64 MDCT scanner with the following protocol: 100 mAs, 120 kV, pitch of 1, $64 \times 0.6mm$ slice collimation; reconstruction: Siemens B30f and B50f kernels, 0.5mm slice thickness, 512×512 matrix and 0.47mm pixel size (Figure 2.10(b)). True A/V separation was obtained from the MDCT image by thresholding at a suitable CT value (Figure 2.10(c)). Before applying the A/V separation algorithm, the effect of distinguishing contrast between A/V trees was eliminated using a post image processing algorithm and subsequently, the contrast eliminated image was down-sampled by a $2 \times 2 \times 2$ window (Figure 2.10(e)). For each of A/V trees, ten seeds were manually selected on the post processed image using a 2D graphical interface and the A/V separation was computed (Figure 2.10(f)).
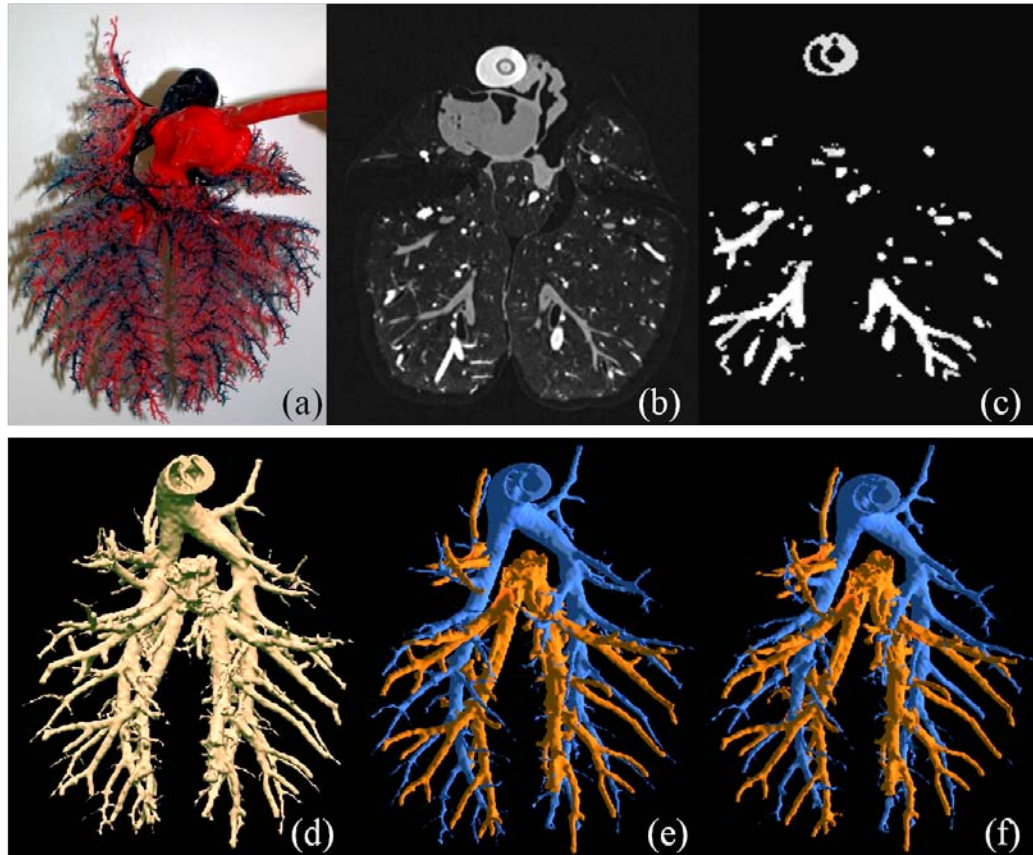
Figure 2.10: Results of A/V separation on a pulmonary pig vessel cast phantom. (a) A photograph of the phantom. (b) A coronal slice from the original CT image of the phantom with different CT-contrasts for arteries and veins. (c) The matching slice after eliminating the effect of distinguishing contrast between arteries and veins. (d) 3D renditions of the reconstructed vasculature from CT data after A/V contrast elimination. (e) True A/V separation from the original contrast-separated CT image. (f) A/V separation using our algorithm after eliminating contrast separation between A/V trees.

Results of A/V separation on vessel casts data are presented in Figure 2.10. The photographic image of the vessel cast (Figure 2.10(a)) shows an extremely dense tree of pulmonary vasculature. CT imaging of the vessel cast at clinically recommended dose could successfully capture (Figure 2.10(d)) 8-10 levels of branching of the pulmonary vasculature. Contrast separation (Figure 2.10(b)) in injected compound in arterial and veinous trees enabled to separate the two trees in the acquired CT image using simple thresholding on CT values (Figure 2.10(e)). The multi-scale topo-morphologic separation algorithm was applied after eliminating effects of contrast separation and down sampling (Figure 2.10(c)). Results of computerized A/V separation are presented in Figure 2.10(f) which shows strong visual agreement with the true A/V separation obtained from contrast separation. Two A/V separations in Figure 2.10(e) and Figure 2.10(f) look very similar except at a few locations with fine scales of vasculature. Also, we performed a quantitative analysis to compute the true positive and false negative of the automated A/V separation as compared with the true knowledge of A/V separation (Figure 2.10(e)). Same equations for true positive and false negative used in computerized phantom study (see Section E.1.a) were applied here. True positive value for the separation found is 94.4 % while false negative is only 1.6%. This results indicate that most of the A/V separations by the algorithm are correct in the sense that, for only at 1.6% situations, arteries was labeled as veins or vice versa. For this example 100%-(94.4+1.6)%=4% volume of true vasculature was missed by the A/V separation algorithm that include the space between the two structures at conjoining locations and also, some of the missing small branches.

To complete this study on vessel cast, the vessel cast was scanned at the Iowa Comprehensive Lung Imaging Center(I-CLIC) on a Siemens Somatom Definition Flash 128 scanner following using the same CT protocol : single tube spiral acquisition at 120kV, 115 effective mAs, 1 sec rotation speed, picth factor: 1.0, norminal collimation: 16×0.3mm. Images were reconstructed in 512×512 matrix with in plane resolution of 0.34mm×0.34mm and with different slice thickness and slice spacing. Four different slice thickness values (0.6, 0.75, 1.0 and 1.5mm) were used for reconstruction and for each slice thickness two different slice spacing (see Talbe 2.5)were considered resulting a total of eight images. Theses images were processed using the same image processing cascade described earlier. For each image exactly ten seeds were selected for A/V trees. Results of A/V separation on the image with 0.6mm slice thickness and 0.4mm slice spacing are shown in Figure 2.11(a-c). Results of application of the method on the image at 1.5mm slice thickness and 1.5mm slice spacing is presented in Figure 2.11(d-f) for comparison. Results of quantitative accuracy analyses using the same protocol as before, is presented in Talbe 2.5, at every slice thickness and spacing, the method has produced high accuracy (true positive). However, as observed in Figure 2.11, a larger slice thickness, finer branches are missed in the process of vascular segmentation. In other words, slice thickness/spacing plays an important role in vascular segmentation at the finer scale. However, after segmentation of vasculature, slice thickness/spacing plays only a minimum role in accuracy of A/V separation.
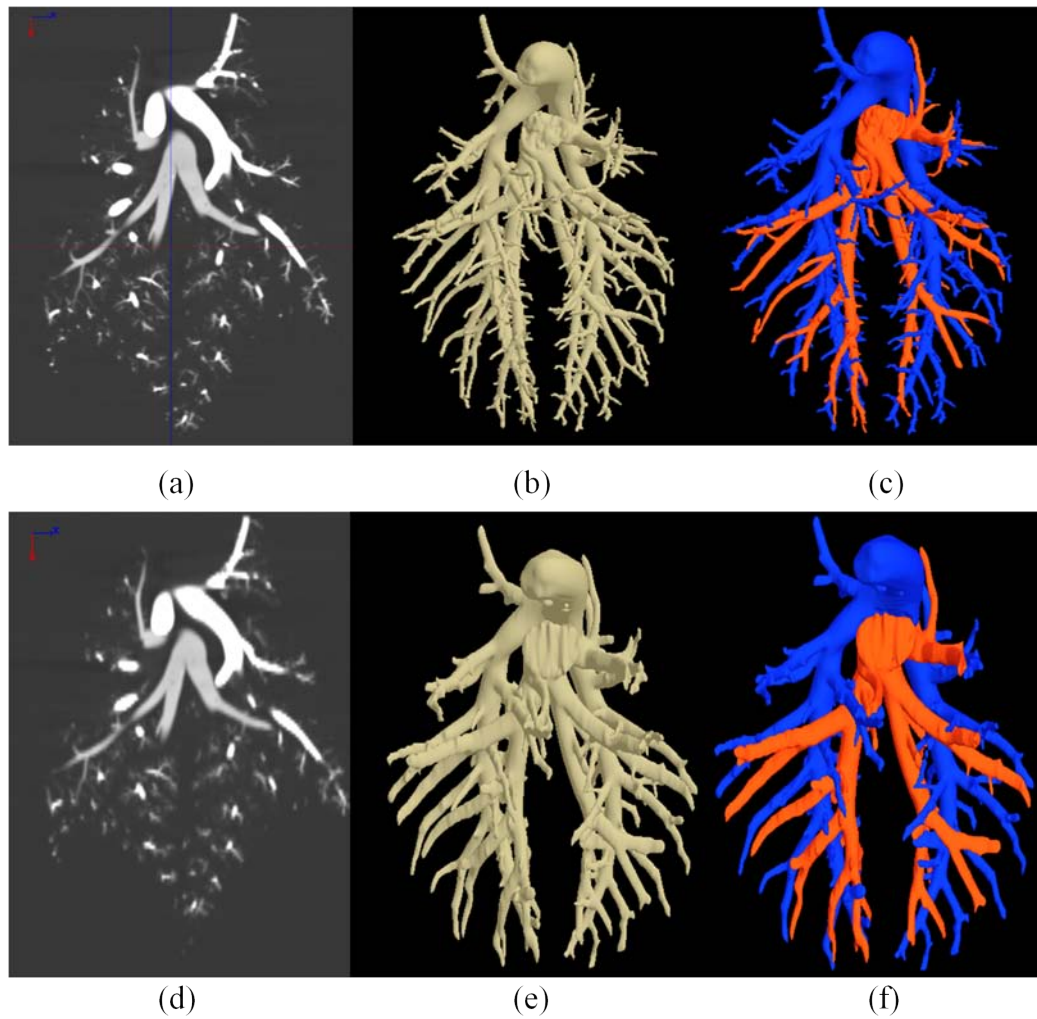
Figure 2.11: Results of A/V separation on a pulmonary pig vessel cast phantoms. (a) and (d) are CT images of two data sets, one with slice thickness 0.6mm and with slice spacing 0.4mm and the other with slice thickness 1.5mm and with slice spacing 1.5mm. (b) and (e) show the 3D rendition of the vasculature of those two data sets. (c) and (f) show the A/V separation using our algrithm

Table 2.5: Results of quantitative accuracy analysis of artery/vein separation of a pig pulmonary vessel cast phantom reconstructed at different slice thickness and spacing.

Slice Thickness (mm)	Slice Spacing (mm)	True Positive	False Negative
0.6	0.4	99.24%	0.76%
0.6	0.6	99.60%	0.40%
0.75	0.5	99.35%	0.65%
0.75	0.75	99.33%	0.67%
1.0	0.8	99.21%	0.78%
1.0	1.0	99.14%	0.86%
1.5	1.2	99.63%	0.36%
1.5	1.5	99.49%	0.50%

2.4.2 Reproducibility

To evaluate the reproducibility of the A/V separation method, we have conducted two different experiments - (1) qualitative multi-airway-pressure reproducibility analysis using contrast-enhanced *in vivo* pulmonary CT imaging of a pig at different lung volumes and (2) quantitative multi-user reproducibility analysis using *in vivo* pulmonary CT imaging of human subjects. In the following sections, I present experimental plans and results for these studies. Also, it has been checked that, for the mathematical phantoms described in Sections 2.4.1.1 and 2.4.1.2, results of separation of two objects in each phantom were exactly the same for seed selection by two independent users, each selecting seeds visually close to the center of corresponding object at the highest scale level. These results demonstrate the theoretical robustness of the method with respect to seed selection.
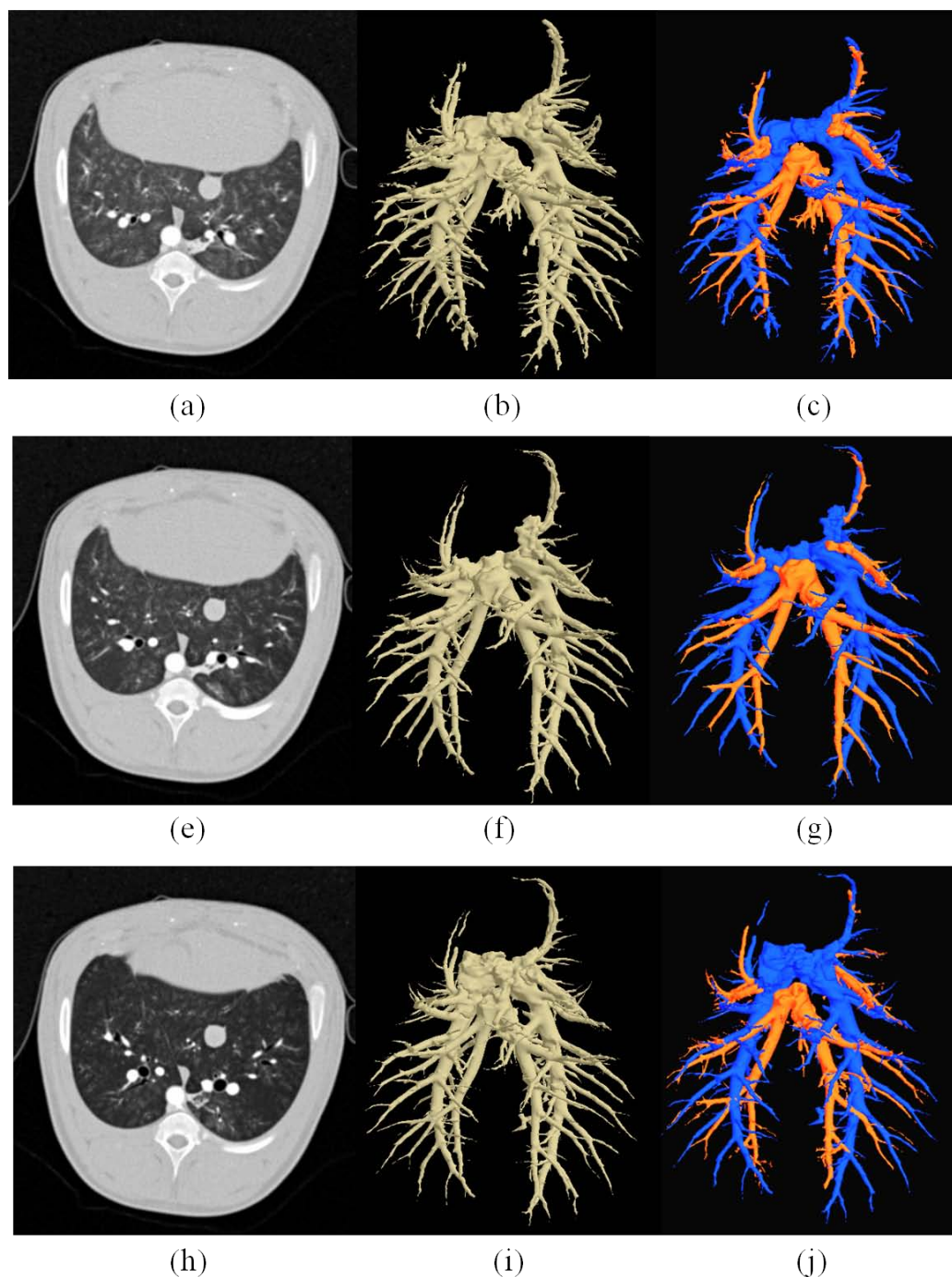
Figure 2.12: Results of A/V separation on contrast-enhanced *in vivo* CT images of a pig's lung at three different lung volumes with B30f reconstruction kernels. (a,d,g) Visually matched coronal slices from original pulmonary CT images at 7.5 cm (a), 12 cm (d) and 18 cm (g) H_2O Positive End-Expiratory Pressures. (b,e,h) 3D renditions of the segmented vasculature from two CT data sets of (a,d,g). (c,f,i) 3D renditions of A/V separation results using our method.
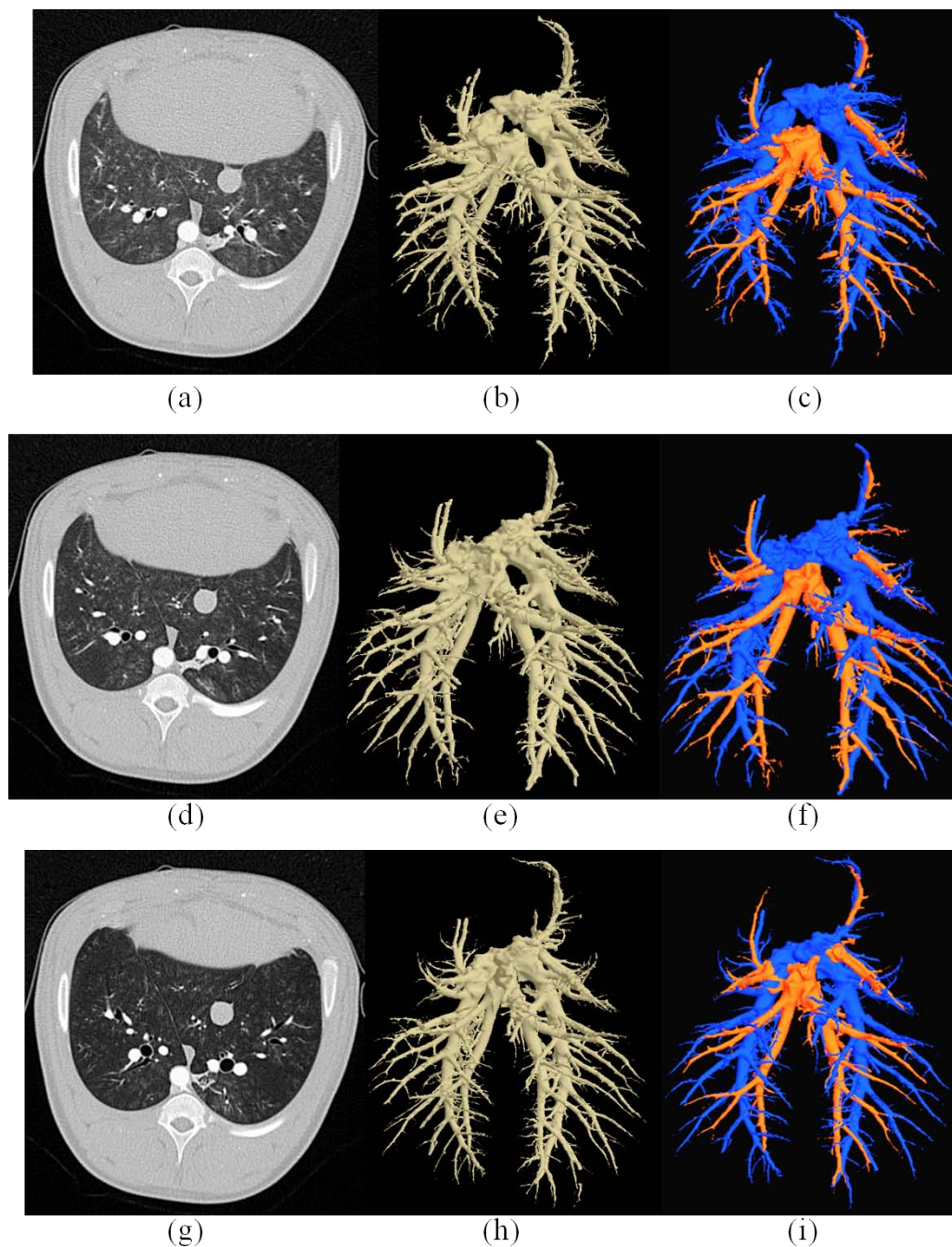
Figure 2.13: Results of A/V separation on contrast-enhanced *in vivo* CT images of a pig's lung at three different lung volumes with B50f reconstruction kernels. (a,d,g) Visually matched coronal slices from original pulmonary CT images at 7.5 cm (a), 12 cm (d) and 18 cm (g) H_2O Positive End-Expiratory Pressures. (b,e,h) 3D renditions of the segmented vasculature from two CT data sets of (a,d,g). (c,f,i) 3D renditions of A/V separation results using our method.

2.4.3 Contrast-enhanced *In vivo* Pulmonary CT Imaging of a Pig at Different Lung Volumes

An anesthetized pig was imaged in the prone body posture at two different positive end-expiratory pressures (PEEP): 7.5, 12 and 18 cm H_2O with the intravenous infusion of 40 cc at 2.5 cc/sec of contrast agent (Omnipaque, GE Healthcare Inc, Princeton, NJ) into the external jugular vein. This contrast protocol was selected to match that used clinically for evaluating the pulmonary arterial bed for the presence of pulmonary emboli. The following CT protocol was used for imaging: 100 mAs, 120 kV, 0.75 mm slice thickness, $64 \times 0.6mm$ slice collimation, B30f and B50f reconstruction kernels, pitch of 1 mm, and 512×512 reconstruction matrix [141]. It's worth mentioning that both the contrast-enhanced *in vivo* CT imaging described here and pulmonary vessel cast data described in the previous paragraph were performed on the same animal and the *in vivo* imaging experiment was performed prior of cast generation. Qualitative results of reproducibility of A/V separation at different airway pressures for contrast-enhanced pig pulmonary CT data are presented in Figures 2.12 and 2.13. Both vasculature and A/V separations results at three airway pressures are displayed from visually similar views. Agreements of A/V separations results three pressures are visually very promising.

2.4.4 *In vivo* Pulmonary CT Imaging of Human Subjects

The overall aim of this experiment is to quantitatively evaluate multi-user reproducibility of the A/V separation method for pulmonary vasculature in human subjects imaged using a clinical CT scan protocol. We have performed run the repro-

ducibility study on seven *in vivo* pulmonary CT images of human subjects. We have completed the experiment on seven data sets. For this study, all images were acquired using the following MDCT protocol: 120kVp, 100mA. Images were colllected at 0.75 mm slice thickness and were reconstructed with 0.5 mm slice-thickness and $(0.6mm)^2$ in-plane resolution. Coronal slice images of MDCT data for two human subjects are presented in Figures 2.14(a) and 2.15(a). The entire vascular tree inside the lung region was segmented in a CT image using a previously published method by Shikata *et al.* [53] that uses tree-connectivity on CT intensity data after processing the image with a tubular enhancement filter and produces a binary vessel image. A fuzzy vascular tree segmentation was generated using the following three steps - (1) determine the mean and standard deviation of intensity values over segmented vascular region, (2) dilate the binary vascular region by one voxel to include partial-volume voxels, and (3) assign fuzzy membership at each voxel over the dilated vascular region following a step up Gaussian function with mean and standard deviation parameters as computed in Step 1. 3D rendition of segmented vascular tree is presented in Figure 2.14(b). Seed points for each of the A/V trees were manually selected by two mutual-blind independent experts using a self-developed 2D/3D graphical interface with the multi-scale topo-morphological separator algorithm built in. A/V separation results from two independent users were used evaluate the reproducibility of the method.

Results of multi-user reproducibility of A/V separation on clinical thoracic CT of two patients are illustrated in Figure 2.14 and Figure 2.15. Although, no true A/V segmentations are available to compare with for this experiment, homogeneous
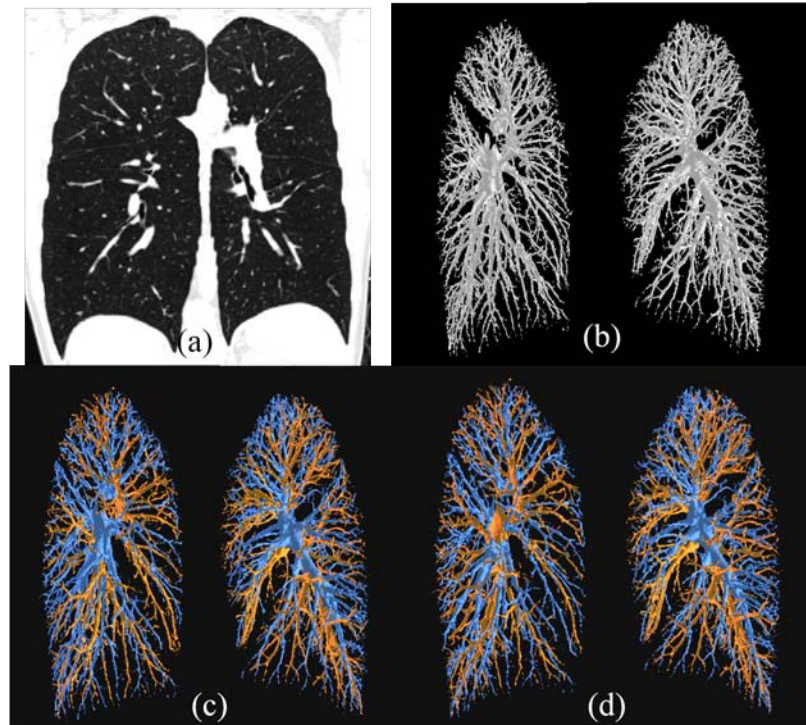
Figure 2.14: Results of A/V separation on an *in vivo* pulmonary CT image of a patient. (a) A coronal image slice from a thoracic CT image. (b) 3D rendition of the fuzzy segmentation of vasculature from the CT data. (c,d) Color-coded renditions of A/V separations using seeds selected by two independent experts.
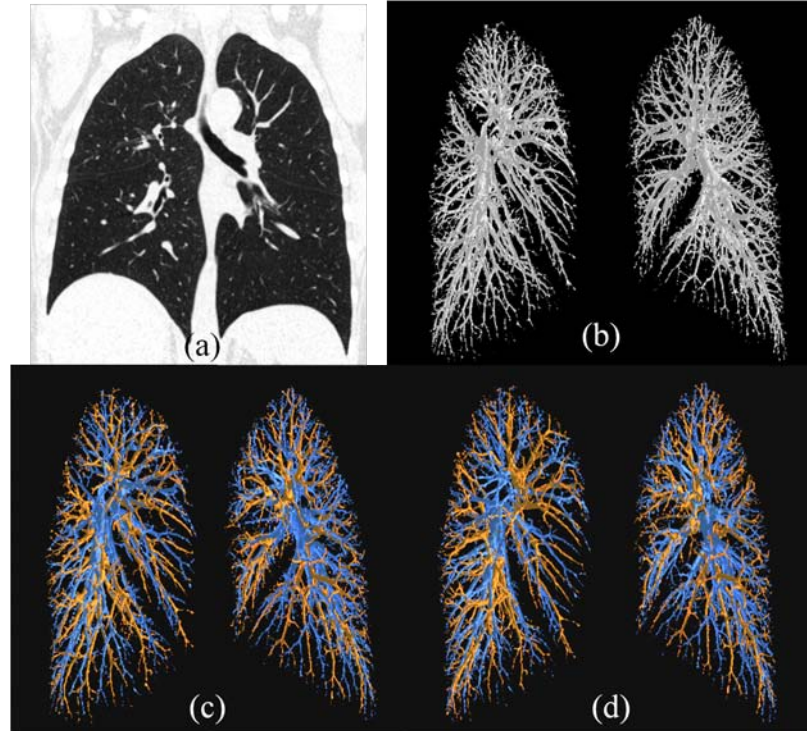
Figure 2.15: Same as Figure 2.14 but for another data set.

distribution of arterial and venous structure complies with biological knowledge of pulmonary artery/vein structures. Despite very dense tree structure of pulmonary vasculatures, for most A/V branches, there are remarkable agreements among results of separation by two independent experts. In order to quantitative evaluate multi-user reproducibility of the method, we computes the following two measures which are designed as small variations of "True positive" and "False Negative" to eliminate the bias in the denominator:

$$Agreement = \frac{(A_1 \cap A_2) \cup (V_1 \cap V_2)}{(A_1 \cup V_2) \cup (A_1 \cup V_2)},\tag{2.17}$$

$$Disagreement = \frac{(A_1 \cap V_2) \cup (A_2 \cap V_1)}{(A_1 \cup V_2) \cup (A_1 \cup V_2)}, \tag{2.18}$$

The quantitative results of multi-user reproducibility on seven human pulmonary CT data sets are shown in Table 2.6.

Table 2.6: Results of quantitative analysis of agreement(AG) and disagreement(DAG) between A/V separations using seeds selected by two independent mutual blind users.

subject No.	whole lung		left lung		right lung	
	AG	DAG	AG	DAG	AG	DAG
1	88.39%	10.03%	90.10%	8.31%	86.77%	11.68%
2	93.64%	5.30%	94.04%	4.89%	93.31%	5.63%
3	94.71%	4.56%	93.73%	5.40%	95.50%	3.88%
4	93.65%	5.83%	92.08%	4.91%	94.24%	2.93%
5	92.53%	6.80%	83.95%	12.69%	97.21%	2.76%
6	90.53%	8.42%	94.16%	5.12%	87.32%	11.34%
7	85.41%	13.32%	82.44%	16.28%	88.29%	10.44%

2.4.5 Efficiency

In this section, I describe our experiments evaluating the efficiency of the A/V separation method using manual tracing of arterial and venous trees using *in vivo* pulmonary CT images of human subjects. It may be noted that for any given manual artery/vein separation (considered as the reference), it is always possible to achieve 100 % accuracy with the proposed method using a sufficiently large number of seed points. It is therefore justified to study the performance of the method in terms of its relation between needed user intervention and accomplished accuracy
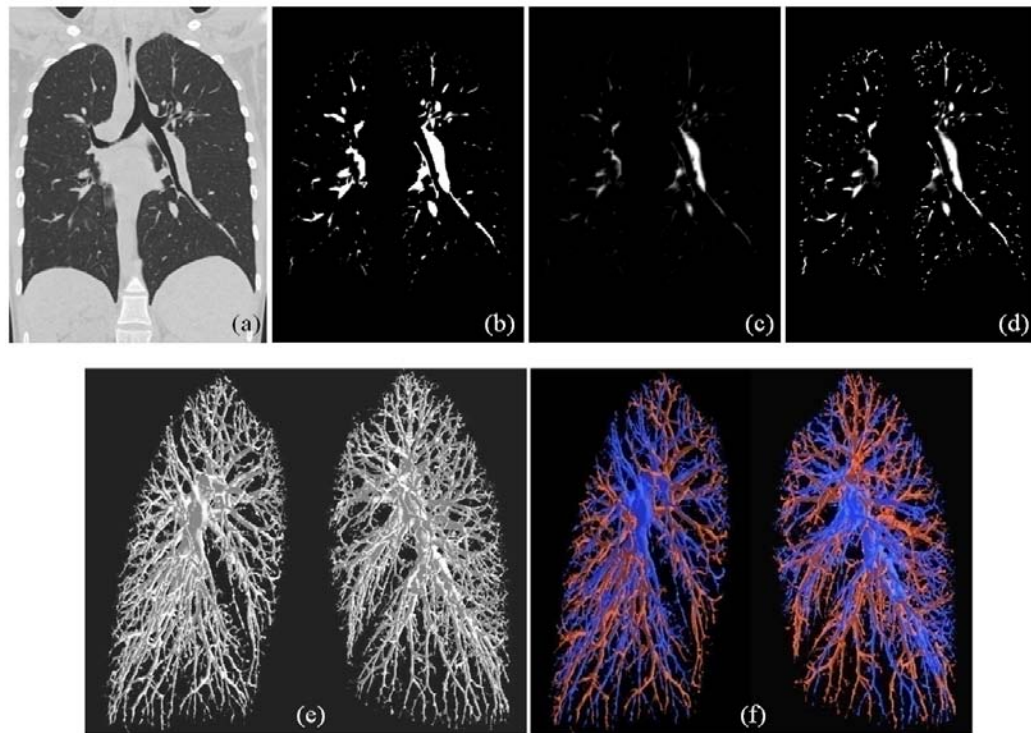
Figure 2.16: Results of application of the method to a human in-vivo pulmonary CT image. (a) A coronal image slice from a thoracic CT image of a 22 years old female. (b) Fuzzy segmentation of vasculature. (c,d) Original (c) and local-scale normalized (d) FDT maps of the vasculature. (e) 3D surface rendition of left and right pulmonary vascular trees. (f) A color-coded 3D rendition of separated arterial and venous trees computed by the proposed method.

or error. Specifically, we compute the accuracy/error of artery/vein separation as a function of the number of seeds used. Two CT data sets presented in Figure 2.16 and Figure 2.17 are used for our quantitative experiment. For each lung data, approximately 8,000-10,000 voxels were manually labeled as arteries and veins by an expert; henceforth, this expert input will be referred to as *inputA*. The purpose of *inputA* was to separately trace arteries and veins in pulmonary vasculature and was accomplished by clicking several points on each slice inside corresponding structures. *InputA* consists of approximately 2,000-2,500 points for arteries and another 2,000-2,500 points for veins in each of the left and right lungs. The first four to five levels of branching is thus described for each of the A/V trees. Now, I will describe a seed selection scheme based on expert's segmentation (*inputA*) of arteries and veins which is considered as the reference in this experimental design. Note that the seed selection scheme is based on expert's segmentation and designed primarily to evaluate the method. Thus, the seed selection scheme is not intended to solve problems relating to "automatic seed selection" which is a research topic on its own.

Let $\mathcal{O} = (p, \mu_{\mathcal{O}}(p))|p \in \mathbb{Z}^3$ denotes the fuzzy representation of a pulmonary vascular tree and let $\Omega_{\mathcal{O}}$ denote the FDT map derived from $\mathcal{O}$. In this section, the original FDT map without any local scale-normalization is used so that the seed selection starts separating arteries and veins at larger scales and then progresses into finer details. Let M_{artery} and M_{vein} denote the sets of voxels manually labeled by the expert as belonging to arteries and veins, respectively; note that M_{artery} and M_{vein} are subsets of *inputA*. The first arterial seed is automatically selected as the
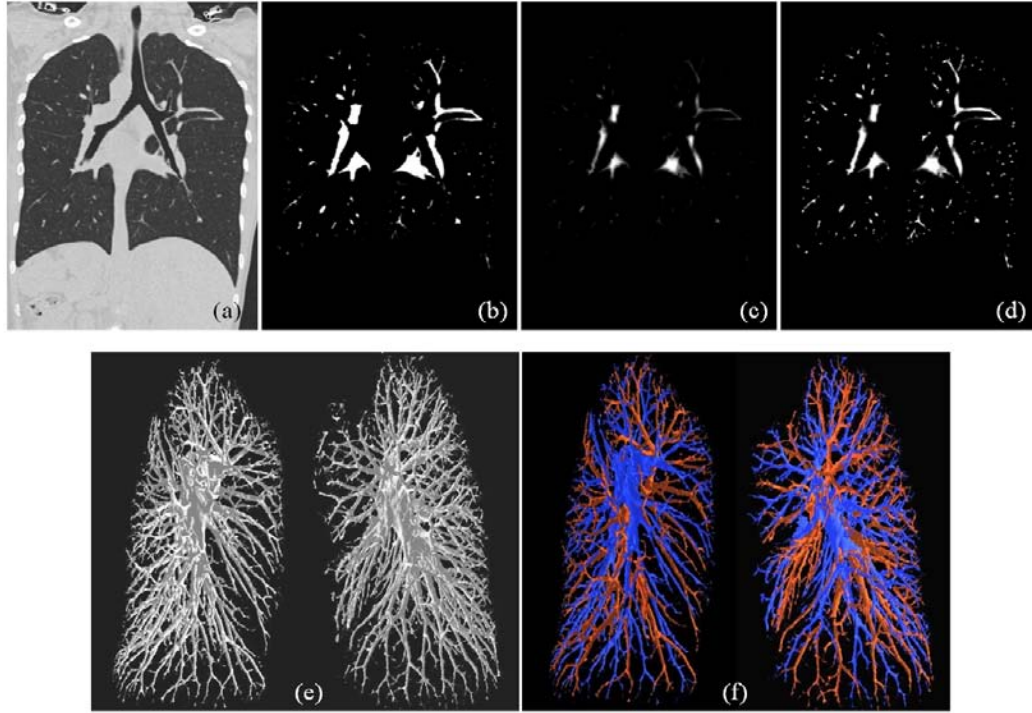
Figure 2.17: Same as Figure 2.16 but for another human subject.

voxel in M_{artery} with the highest FDT value, i.e., with the largest-scale value. Let A_1 denote the set of the singleton seed voxels for artery; the subscript index indicates the iteration number. The set V_1 of singleton seed voxels for veins is defined in the exact same way using M_{vein}. Let C_{artery}^1 and C_{vein}^1 denote the arterial and venous regions computationally segmented from $\mathcal{O}$ using the proposed method with A_1 and V_1 being the sets of seeds for arteries and veins, respectively. Accuracy and errors of the proposed method for single seed may be computed by comparing C_{artery}^1 and C_{vein}^1 with the reference segmentation M_{artery} and M_{vein} .

Exact definitions of accuracy and error measures are described in the following paragraph; first, let us describe the iterative progression scheme for seed selection

refining artery/vein separation. Let A_i and V_i denote the sets of seeds for arteries and veins in the ith iteration and let C_{artery}^i and C_{vein}^i denote the regions assigned to arteries and veins, respectively; note that each of A_i and V_i contains exactly i number of seeds. Let O_i denote the same fuzzy object as O except that membership values over $(C_{artery}^i \cap M_{artery}) \cup (C_{vein}^i \cap M_{vein})$, i.e., the set of correctly segmented artery/vein voxels, are set to zero. Let Ω_{O_i} denote the FDT map of O_i. During the $(i + 1)$th iteration, the set of arterial seeds A_{i+1} is augmented by exactly one voxel p to $A_i \cap p$ such that $p \in M_{artery} - C_{artery}^i$ and it has the highest value in Ω_{O_i}; in case of multiple voxels with the highest FDT value, one is selected arbitrarily. The set of venous seeds V_{i+1} is augmented in exactly the same manner. It may be noted that the seed selection scheme adopted for the current experiment is deterministic in nature and therefore generates only one sequence of seeds for a given segmentation of vasculature and A/V separation.

Accuracy of the method is defined by comparing its results with manual labeling of arteries or veins in inputA. Here, we need to mention the following three facts.

1. Each of manually labeled arteries and veins M_{artery} and M_{vein} is truly a set of voxels selected by an expert using mouse cursor clicks and not a painted region. On the other hand, our computerized method generates volumetric regions C_{artery}^i and C_{vein}^i for arteries and veins.

2. Segmented arterial and venous trees produced by the computerized method capture fine details. On the other hand, the expert could separately trace
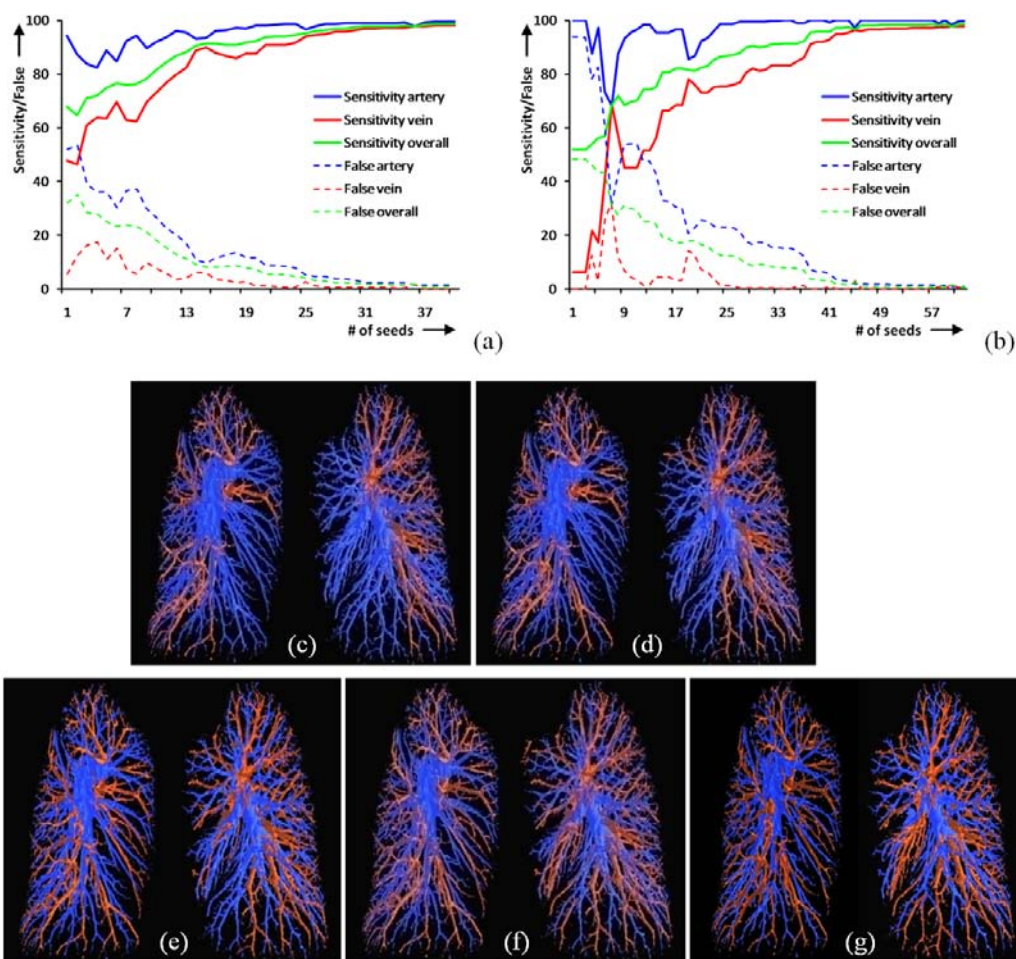
Figure 2.18: Illustration of the results of evaluation of efficiency of the A/V separation method. (a,b) Graphical presentations of results of quantitative analysis comparing required user intervention with accomplished accuracy/errors for the pulmonary CT data presented in Figure 2.16(a) and Figure 2.17 (b). For Figure 2.16, the number of seeds, false and miss at 95% and 99% overall sensitivity are: 27, 4.2%, 0.8% and 52, 0.6%, 0.4%, respectively; these numbers for the example of Figure 2.17 are 40, 3.7%, 1.3% and 66, 0.5%, 0.5%, respectively. (c-f) Qualitative illustrations of artery/vein separation at sensitivity levels of 80%, 90%, 95%, and 99%, respectively. (g) Results of A/V separation of the same lung using seeds from an independent expert. To produce this result approximately 25-35 seeds were used for each of the A/V trees for each of the left and right lungs.

arterial or venous trees only for larger branches.

3. A large number of voxels, approximately 8-10 thousand, were labeled for arteries/veins for each thoracic CT image.

Based on these three observations, we have defined segmentation performance measures in terms of sensitivity, false detection, and missed locations as follows (arterial definitions given):

$$Sensitivity = \frac{|M_{artery} \cap C_{artery}^i|}{|M_{artery}|}, \tag{2.19}$$

$$False = \frac{|M_{vein} \cap C_{artery}^i|}{|M_{artery}|}, \tag{2.20}$$

$$Miss = \frac{|M_{artery} - C_{artery}^i \cap C_{vein}^i|}{|M_{artery}|}. \tag{2.21}$$

Sensitivity and *false* detection measures of the method for the two CT data sets of Figure 2.16 and Figure 2.17 are presented in Figure 2.18(a) and (b), respectively. Assuming that both M_{artery} and M_{vein} are entirely included via initial segmentation of composite pulmonary vasculature, the measure of *miss* was expected to be close to zero and the experimental results confirmed our expectation. Therefore, we omit the graphical plots for missed locations in Figure 2.18(a) and (b) keeping the graphs simpler. As illustrated in Figure 2.18(a), 95% overall accuracy was achieved for the CT data set of Figure 2.16 using 27 seeds at the cost of 4.2% false detections and 0.8%

miss. It required 52 seeds to accomplish 99% sensitivity at false rate of 0.6% and 0.4%
miss. For the CT data set of Figure 2.17, 95% overall accuracy was achieved using
40 seeds at the false detection rate of 3.7% and 1.3% miss and 99% accuracy was
obtained using 66 seeds at the false detection rate of 0.5% and 0.5% miss. To convey
the quality of artery/vein separation at different levels of accuracy, we present the
results for the data set of Figure 2.16 at 80%, 90%, 95% and 99% overall accuracy.
It may be interesting to compare the results of Figure 2.18(f) produced from the
expert input inputA with that produced using seeds from an independent expert.
It is encouraging to see the high level of agreement between such two independent
expert-driven separations of arteries and veins using the current algorithm.

An intriguing observation in Figure 2.18(a) and (b) is that the sensitivity
of separating arteries/veins may reduce despite adding more seeds. For example,
in Figure 2.18(b), it starts with almost 100% sensitivity for arteries and then falls
significantly after adding more seeds before rising again. What happens here is that,
initially, most of the vasculature is occupied as arterial territory leaving only a small
region for veins. It leads to the initial high sensitivity for arteries while low sensitivity
is observed for veins. As more seeds are added, the segmentation loses falsely acquired
venous territories along with some arterial territories which were connected through
those previous false acquisitions of venous territories. This leads to the reduction
in both arterial sensitivity and false measures as presented in Figure 2.18(a) and
(b). A high sensitivity together with a low false detection generally indicates a good
segmentation of the specific structure.
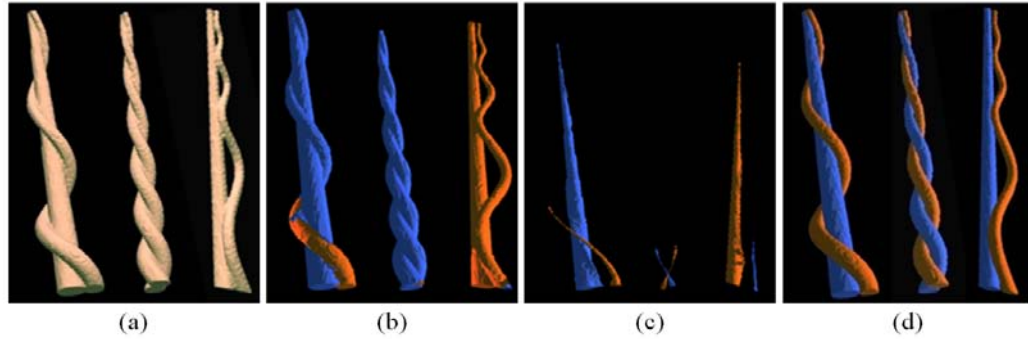
Figure 2.19: Comparison of the results on three mathematical phantoms using three different methods. (a) Three mathematical phantoms each containing two tubular objects fused at different locations and scales with significant overlap. Results of separations of two objects using the algorithm by Lei *et al.* [73] (b), simple FDT-based IRFC [126, 159] (c), and the multi-scale topo-morphologic opening algorithm reported here (d).

In conclustion, a fundamentally novel topo-morphologic multi-scale opening operator was presented for separating two iso-intensity objects mutually fused at various scales and locations. Experimental results demonstrated its performance. The method seeks morphological identities of each object at a specific scale and separates them without using any gradient- or edge-like features. Introduction of the ideas of morphological reconstruction and separator allows the method to seal the joining border at the current scale and then seek morphological features identifying different objects at finer scales. Let us first clarify the differences between the current method and the previous state of the art algorithms related to fuzzy connectivity [73, 160, 158] and fuzzy distance transform [134]. The prior arts of fuzzy distance transform and fuzzy connectivity are used here only to solve the first step of the three basic steps used by our new method as stated in Section 2.2. Further, the novelty of

demonstrating that fuzzy distance transform and fuzzy connectivity together with the seeds of two objects allow automatic determination of the optimum opening structure scale separating two mutually fused objects is part of the current work. Additionally, the morphological reconstruction introduced here to block the annular remainder of separation at the current scale is a simple yet effective step allowing morphological separations at lower scales. The A/V separation paper published by Lei *et al.* [73] was designed for contrast enhanced MR images and it uses intensity variations at vessel walls (which are expected to exhibit lower MR signal values as compared to contrast enhanced lumen) to separate arteries and veins. However, such assumption does not hold for CT images where intensity variation at regions of fusion between arteries and veins is almost absent. To demonstrate the improvements achieved by the current method, the algorithm by Lei *et al.*, and an algorithm with a straightforward application of fuzzy distance transform into iterative relative fuzzy connectivity (IRFC) framework [126] were implemented and applied to several mathematical phantoms of Fig. 2.6. By comparing the results of these three different methods presented in Fig. 2.19, it is obvious that the current method is fundamentally different from prior state of art methods. In summary, the technical contributions of the current work are as follows:

1. The current work models the A/V separation task via non-contrast CT imaging as an entirely new multi-scale topo-morphologic opening task.

2. Our method provides a unique solution to the problem where existing methods fail.

3. The reported method provides a practical solution to a clinically important problem.

4. The presented theory opens a new avenue of multi-scale topo-morphologic operations.

An application of the proposed method for separating pulmonary arteries and veins in *in vivo* thoracic CT images has been studied. For pulmonary CT images, the geometry of coupling between arteries and veins is very challenging and quite unknown. However, the method has shown acceptable performance with a reasonable number of seeds. Approximately 25–35 seeds were manually selected by an expert on each of the A/V sub-trees for each of the left and right lungs. It may be pointed out that the seeds were selected using a 3D/2D graphical tool. Often multiple seeds were placed within the same locality of an object and therefore, not all of the seeds contributed to true A/V separation. A quantitative experiment has demonstrated that the method can yield 99% accuracy for the entire pulmonary vasculature using approximately 60 seeds selected using a computerized blind seed selection scheme.

Both qualitative and quantitative results on computer and cast phantoms as well as clinical pulmonary CT data have been presented. Results have established viability of the new method in resolving multi-scale fusions of two iso-intensity structures with complex and unknown geometry of coupling, that are often present in biological objects. The experimental results, beyond any doubt, have established usefulness of the current method in separating arteries and vein in pulmonary CT images without any blood pool contrast.

CHAPTER 3
MULTI-LEVEL ANALYSIS OF PULMONARY ARTERY/VEIN TREES

In this chapter, I describe a new theory and method to construct a tree representation for each of arterial/venous trees obtained using the method described in Chapter 2. The immediate application of the method is to extract quantitative morphometric measurements at different tree levels of A/V trees. A reliable and automatic method of A/V topological tree generation will be of paramount interest in intra- and inter- object pulmonary registration. Here, tree junctions and branches will play roles in building landmark correspondence. Also, a cross-sectional study on analysis of A/V tree topology and geometry has potential to develop human pulmonary A/V tree atlas and nomenclature of major A/V branches. Such a study may be useful in understanding variations among human pulmonary tree topology and geometry and their association with different diseases and genotypes.

Basic design of our method to generate A/V topological tree is based on computation of arc skeleton and then building a topological tree using topologic and geometric analysis of the arc skeleton. However, the complexity of the task is significantly increased due to presence of noisy branches as well as topologic and geometric aberrations intrinsically linked to the skeletonization step. Our method produces a multi-level representation of arterial/venous volumetric trees. The accuracy of the method is evaluated using several computer generated tree phantoms. Also, the reproducibility of the method is examined using CT images of the pulmonary vessel cast

of a pig lung and CT image of a pig's lung under different airway pressures already discussed in Chapter 2.

In the following sections, first, I present definitions, theory and algorithm related to 3D topology and skeletonization used in this chapter. Then, I describe the method to generate A/V topological tree and multi-level volumetric A/V representation along with different A/V measurements. Subsequently, I describe our experimental plans, methods and results. Finally, I draw some concluding remarks along with future research directions.

3.1   Definitions and Notations

Here, $\mathbb{Z}$ is used to denote the set of all integers. It may be noted that $\mathbb{Z}^3$ represents a *digital space* and each element of a digital space is referred to as a *voxel* whose position is denoted by Cartesian coordinates $(x_1, x_2, x_3)|x_1, x_2, x_3 \in \mathbb{Z}$. For any two voxels $p, q \in \mathbb{Z}^3$, $|p - q|$ denotes the Euclidean distance between the two voxels. All topological formulations described in this chapter are confined to binary digital images, i.e., a voxel may have only two values — object and background. Such images are often obtained by thresholding [97, 128] a gray-scale intensity image into object and background regions. An *object* in a binary image may be represented as a set $\mathcal{O} \subset \mathbb{Z}^3$ of voxels. Following the fact that the field of view of an acquired image is always finite, the cardinality of an object $\mathcal{O}$, denoted by $\|\mathcal{O}\|$, is always finite. We use $\bar{\mathcal{O}} = \mathbb{Z}^3 - \mathcal{O}$ to denote the background for the object O. In the current application, the set of arterial or venous voxels constitutes the object and the background represents the set of all other voxels. Two voxels (x_1, x_2, x_3) and (y_1, y_2, y_3) are called 6-*adjacent*

if and only if $\sum_{i=1}^{3}(x_i - y_i)^2 \leq 1$ (face adjacent only); they are called 18-*adjacent* if and only if $\sum_{i=1}^{3}(x_i - y_i)^2 \leq 2$ (face or edge adjacent); and they are called 26-*adjacent* if and only if $\sum_{i=1}^{3}(x_i - y_i)^2 \leq 3$ (face, edge, or corner adjacent). Two α-adjacent voxels, where $\alpha \in \{6, 18, 26\}$, are often referred to as α-neighbors of each other. Let $p = (x_1, x_2, x_3)$ denote a voxel and let $q = (y_1, y_2, y_3)$ and $r = (z_1, z_2, z_3)$ denote two 6-neighbors of p. The two voxels q, r are referred to as opposite 6-neighbors of p if and only if $y_i - x_i = x_i - z_i = \pm 1$, for some $i \in \{1, 2, 3\}$; note that the two opposite 6-neighbors q, r share two opposite faces of the voxel p. To satisfy the Jordan surface property in a binary digital image, whenever 26-adjacency is used for object (i.e., the set of A/V voxels), 6-adjacency must be used for the background (i.e., the set of non A/V voxels) and vice versa [110]. It ensures that a closed object surface is the necessary and sufficient condition to separate the background into two components — the interior and the exterior. Here, we use 26-adjacency for object voxels and 6-adjacency for background voxels. Often, a topological property derived with such an adjacency convention is referred to as a (26,6) topological property.

In digital topology, we often refer to three entities — components, tunnels, and cavities; we define these three entities in the following. Let S be a nonempty set of voxels. An α-path$|\alpha \in 6, 18, 26$ in S between two voxels $p, q \in S$ is a sequence of voxels $\langle p = p_0, p_1, \cdots, p_n = q \rangle$ in S such that p_i is α-adjacent to p_{i+1} for all $0 \leq i \leq n$. An α-curve is an α-path $\langle p_0, p_1, \cdots, p_n \rangle$ if and only if p_i, for $0 < i < n$, has exactly two α-neighbors on the path. An α-path (or, an α-curve) is an α-closed path (respectively, an α-closed curve) if p_0 is α-adjacent to p_n. Two voxels $p, q \in S$ are α-connected in S

if there exists an α-path from p to q in S. An α-component of S is a maximal subset of S where each pair of voxels is α-connected in S. A *cavity* in S is a 6-component of $\bar{S}$ surrounded by S. Although tunnels are easily visualized and intuitively described, they are difficult to formally define. However, the number of tunnels in an object can be defined precisely. Intuitively, a tunnel is formed by bending a cylinder to connect its two ends to each other or to a single connected object, e.g., the handle of a coffee mug. More accurately, the number of tunnels in an object is the rank of its first homology group [68].

In the following discussions, for any voxel p, $\mathcal{N}(p)$ denotes the set of all voxels in the $3 \times 3 \times 3$ neighborhood of p including p and $\mathcal{N}^*(p)$ denotes the set $\mathcal{N}(p) - \{p\}$. Because of the structure of $3 \times 3 \times 3$ neighborhood, assuming that the central voxel p is an object voxel, the set of all object voxels in $\mathcal{N}(p)$ always forms exactly one 26-connected component without tunnels and cavities [125], i.e., the topological property of the set of object voxels in $\mathcal{N}(p)$ is invariant. Therefore, the local topology of a voxel p is solely characterized by the set of object voxels in $\mathcal{N}^*(p)$. Let $\xi(p)$, $\eta(p)$ and $\delta(p)$, respectively, denote the numbers of object components, tunnels, and cavities formed by the set of object voxels in $\mathcal{N}^*(p)$. The entities $\xi(p)$, $\eta(p)$ and $\delta(p)$ are referred to as local topological parameters of p [120, 124]. Let $X(p)$ and $Y(p)$ denote the sets of 6- and 18-adjacent background neighbors of p, respectively. The following two theorems [120, 118, 121] provide computational definitions of $\eta(p)$ and $\delta(p)$:

Theorem 1 If $X(p)$ is nonempty, the number of tunnels $\eta(p)$ is one less than the number of 6-components of $Y(p)$ intersecting with $X(p)$, or zero otherwise.

Theorem 2 The number of cavities $\delta(p)$ is one when all the 6-neighbors of p are object voxels and zero otherwise.

Rigorous proofs for these theorems may be found in [125] while more intuitive and illustrative clarifications are presented in [49]. Intuitively, a voxel p is a "simple voxel" if and only if its binary transformation (i.e., conversion from object voxel to a background voxel or vice versa) does not alter digital topology of an object. Following Saha *et al.* [120, 118, 121], a voxel p is a (26,6)-simple voxel if and only if the number of object component $\xi(p)$ in $\mathcal{N}^*(p)$ is exactly one and the number of tunnels $\eta(p)$ and the number of cavitie $\delta(p)$ in $\mathcal{N}^*(p)$ are both zero. An efficient computational solution for both (26,6)-simple voxels and local topological parameters $\xi(p)$, $\eta(p)$ and $\delta(p)$ was presented in [120, 124, 125] using the notions of dead faces, dead edges, effective voxels and geometric classes of $3 \times 3 \times 3$ neighborhood. In the following, first, we briefly review the skeletonization method as the developments in subsequent sections are based on the output of this step.

3.2   Skeletonization

We have adopted a previously reported skeletonization method [122] where the entire process is completed in two stages, namely, surface skeletonization and arc skeletonization. Each of these two skeletonization stages is completed in two steps — primary and secondary skeletonization. Primary skeletonization iteratively erodes object voxels from the current outer layer of the respective structure while preserving its topology and so-called "shape". In order to preserve object topology, only (26,6)-simple voxels [118, 121] are considered for erosion. Both surface- and arc-like shape

voxels [122] are preserved during the erosion process in surface skeletonization while only arc-like shapes are preserved during arc-skeletonization. The output of primary skeletonization may contain two-voxel thick surfaces and curves. Extra thick voxels [122] are removed using an extra iteration referred to as secondary skeletonization. It may be noted that, surface skeleton produced a digital structure consisting of both arcs and surfaces. These arcs need no further thinning while the surfaces are converted into arcs during arc-skeletonization. Result of the skeletonization method on an arterial tree of a pulmonary pig lung cast is presented in Figure 3.3(b). It is noted that the skeleton shown in Figure 3.3(b) is the 3-D mesh display of the arc skeleton tree after dilated by 3 voxels. The purpose of such dilation is to make the arc skeleton more visible in 3-D mesh display.

3.3   Shape Distance Transform

The skeletonization method [122] adopted in our research attempts to reduce effects of noise in a skeleton using local context of object geometry. However, some noisy protrusions/dents in a digital image slips through the constrains leading to noisy branches in the arc skeleton and therefore, such branches need to be pruned before generating final A/V topological tree. We have developed a new tree pruning algorithm described in Section 3.4.4 using shape distance transform [135] that allows identification of noising branches based on global context of skeletal geometry. In the following we, define shape distance transform and describe its significance in detecting noisy skeletal branches.

The basic idea here is to distinguish skeletal branches contributed by true
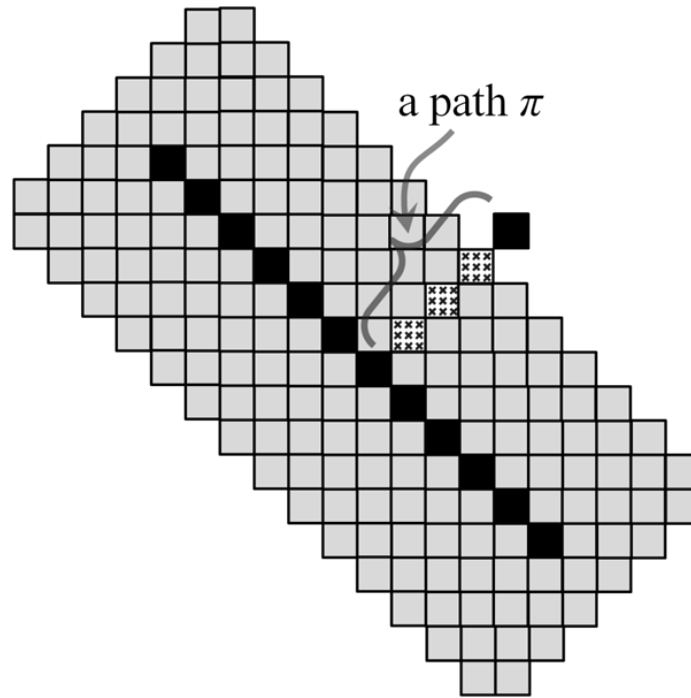
Figure 3.1: An illustration of shape distance transform. Both black and textured pixels indicate skeletal pixels in the given shape. Black pixels survive in the skeletonization process as shape pixels, i.e., saved to preserve local shape of the structure. On the other hand textured pixels are preserved to maintain the topology. Shape distance only counts shape voxels on a path. For example, only one shape voxel contributes to the shape length of the path π.

geometric features in the original object from those originated by noisy bumps or dents, often, common in digital images. However, often, a small branch originating from a one- or two-voxel protrusion grows iteratively due to the topology preservation constraint and eventually leads to a long branch in the final skeleton (see Figure 3.1). Frequently, such branches appear to be an important feature in a skeleton and may not be recognized as a noisy branch without additional information. To overcome this problem, in a skeletal branch, we distinguish voxels needed to maintain object shape features from those survived merely for topology preservation. Fortunately, the skeletonization method adopted here keeps record of the voxels surviving for shape preservation during skeletonization; we will refer to those voxels as *shape voxels* in a skeleton and will use S_S to denote the set of all shape voxels in the skeleton S. In order to determine the importance of a branch in a skeleton, we only consider shape voxels in length computation and ignore voxels survived merely for topology preservation. The idea of "shape distance transform" (STD) may be better understood using an example as illustrated in Figure 3.1. Let us consider a linear digital shape as shown in the figure that contains a noisy pixel. Following that shape pixels/voxels are always defined locally, a noisy pixel/voxel may slip through the constraint of a shape pixel/voxel. Depending upon the constraints for a shape point, it is always possible to create an example of a noisy protrusion that is wrongly chosen as a shape pixel/voxel. Here, we have used a simple example as our main intension is to illustrate the idea of SDT. Although, only one pixel in a noisy protrusion is selected as a shape pixel, it leads to a long branch in the final skeleton caused by topology preservation. Therefore,

just by looking at the skeleton, it's often difficult to decide whether a branch is caused by noisy protrusion or it carries meaningful information of the original shape. We formulate SDT such that only shape pixels/voxels contribute to the "shape length" of a path (or a branch) and the pixels/voxels survived merely because of topology preservation are ignored. Thus only one pixel will contribute to shape length of the path that later makes it easy to decide the path as a noisy branch. Shape length is formulated using a new membership function μ_{S_S} which takes '1' value when a voxel is a shape voxel and '0', otherwise.

Using the digital topological classification method [168], we can identify junction, interior and edge voxels in a skeleton. Let S_E denote the set of all edge voxels and let S_J denote the set of all junction voxels in the skeleton S. A 26-path $\pi = \langle p = p_0, p_1, \cdots, p_{n-1} = q \rangle$ between two voxels $p, q \in S$ is called a 26-valid path if $\nexists r \in S_J$ and $0 \leq i < n$ such that $\|p_i - p_{i+1}\| > max(\|p_i - r\|, \|r - p_{i+1}\|)$. A violation of the validity condition of a path is considered as a "crossing" with a junction, because, the path $\cdots, p_i, r, p_{i+1}, \cdots$ is more natural than the path $\cdots, p_i, p_{i+1}, \cdots$ in the sense that the former path requires shorter steps to move from p_i to p_{i+1}. Shape length of any 26-valid path $\pi = \langle p_0, p_1, \cdots, p_{n-1} \cdots \rangle$ on a skeleton S, denoted by $\Pi_{S_S}(\pi)$ is defined as follows

$$\Pi_{S_S}(\pi) = \sum_{i=0}^{n-2} \frac{1}{2}(\mu_{S_S}(p_i) + \mu_{S_S}(p_{i+1}))\|p_i - p_{i+1}\|, \qquad (3.1)$$

$$\text{where } \mu_{S_S}(p) = \begin{cases} 1, & \text{if } p \in S_S, \\ 0, & \text{oherwise.} \end{cases} \tag{3.2}$$

Shape distance transform or SDT of a voxel $p \in S$, denoted by $SDT(p)$ is the shape length of one of the shortest (w.r.t. shape length) 26-valid paths from p to any voxel $q \in S_E$; if there is no 26-valid path from p to a voxel $q \in S_E$, the SDT value $SDT(p)$ is set to $+\infty$ or equivalently, a very large number. The algorithm for computing shape distance transform is presented in the following.

begin compute-shape-distance-transform

input:

    (1) a skeleton S

    (2) a set of junction voxels $S_J \subset S$

    (3) a set of edge voxels $S_E \subset S$

    (4) a set of shape voxels $S_S \subset S$

    (5) a fuzzy distance transform image $\{(p, \Omega_{\mathcal{O}}(p)) | p \in \mathbb{Z}^3\}$

output: shape distance transform map $SDT : S \to R$

auxiliary data structure: a sequential queue Q

Step 1 for each voxel $p \in S$

    assign $SDT(p) = max\_SDT\_value$

Step 2 for each voxel p in S_E

    assign $SDT(p) = \Omega_O(p)$

    push p in Q

Step 3 while Q is not empty

    pop a voxel p from Q

    for each voxel $q \in N_{26}(p) \cap S$

        define $link(p, q) = \frac{1}{2}(\mu_{S_S}(p_i) + \mu_{S_S}(p_{i+1}))\|p - q\|$

Step 3a if $q \in S_J$ AND $SDT(q) > SDT(p) + link(p, q)$

    assign $SDT(q) = SDT(p) + link(p, q)$

Step 3b else if $SDT(q) > SDT(p) + link(p, q)$

    AND $\nexists r \in S_J$ such that $\|p - q\| > max(\|p - r\|, \|q - r\|)$

    assign $SDT(q) = SDT(p) + link(p, q)$

    push q in Q

end compute-shape-distance-transform

The above algorithm for computing shape distance transform works similar as the FDT computation algorithm except that initial waves are placed only at edge voxels of a skeleton (Step 2). Also, in the wave propagation process (Step 3), only shape voxels contribute in shape distance as discussed earlier. The conditions in Steps 3a and b are used to check validity of paths to avoid undesired crossing with junctions.

3.4   Topological Tree Generation

In this section, I describe the theory and algorithms to generate a topological A/V tree form their arc skeleton representations. In order to reduce ambiguities, I

will consistently use topological and volumetric, arc skeleton and volumetric trees to denote these different data structures. Specifically, volumetric tree is a 3-D binary image representing 3-D region occupied by A/V. An arc skeletal tree is a 3-D binary image representation of the arc skeleton of A/V obtained by applying arc skeletonization on its volumetric tree representation. A topological tree is an analytic representation of A/V tree using tree nodes and branches connecting root, parent, child and end nodes. In our development, a tree node representation is using the following data structure:

Tree-Node

{

        Voxel-Coordinate: slice, row, column

        Depth-from-the-Root: depth

        Height-from-the-Leaf: height

        Arc-length-from-the-farthest-Leaf: arcLength

        Branch-Length-to-Parent-Node: branchLength

        Parent-Node-Address: parentNode

        Child-Node-List: childList

}

Overall work flow diagram of the topological tree generation algorithm is presented is Figure 3.2. The method starts with volumetric representation of A/V and its arc skeleton as inputs and output its topological tree representation along with
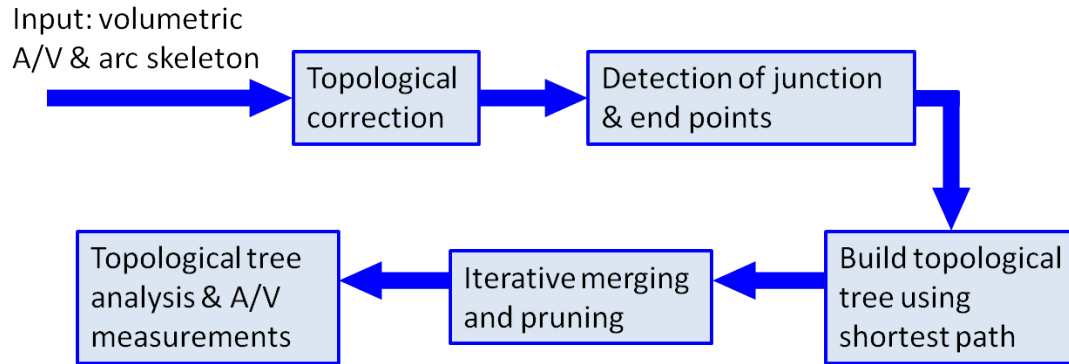
Figure 3.2: Overall work flow diagram of the topological tree generation algorithm.

different A/V measures and multi-level representation of the volumetric tree. In the following section, I describe each of this steps shown in Figure 3.2.

3.4.1 Topological Correction

The purpose of this step is to ensure that an arc skeleton is proper tree-concatenation of finitely many curves. More specifically, this step ensures that an arc skeleton contains no (26,6) simple points expect at end voxel, i.e., a curve edge type voxel [119]. This topological correction step is also used in the iterative merging and pruning to ensure topological validity in the arc skeleton after every iteration pruning and merging. The topological correction is accomplished by iteratively deleting non-end (26,6) simple points in an arc skeleton-like representation.

3.4.2 Detection of Junction and End Voxels

Junction voxels are detected on the arc skeleton. Intuitively, a junction voxel is characterized as the location where multiple curves are glued, i.e., removal of the voxels creates multiple object components in the sufficiently small neighborhood of
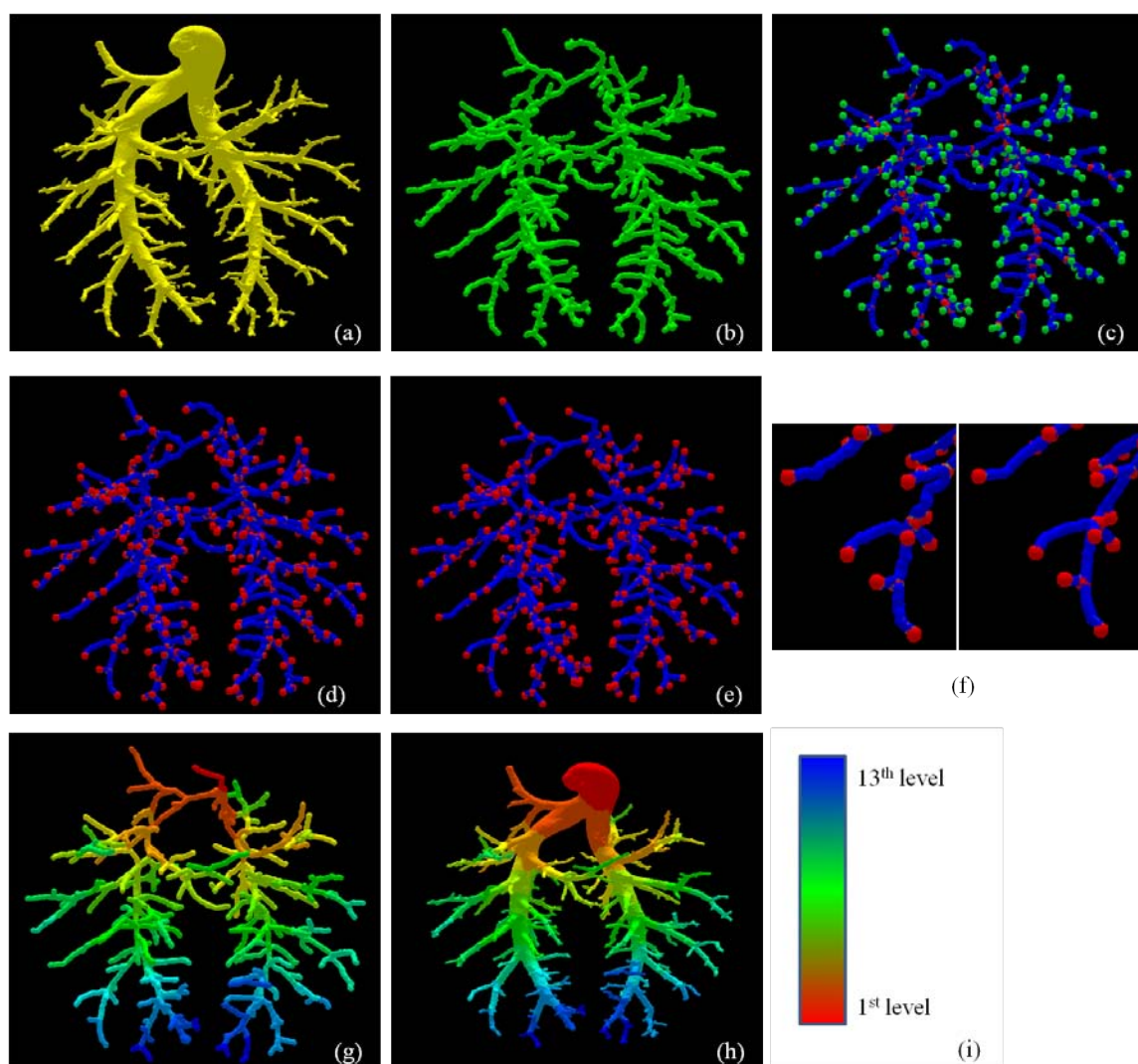
Figure 3.3: Illustration of intermediate results at different steps of the tree generation and analysis(a) 3-D rendition of arterial tree. (b) Arc skeleton of the artery tree. (c) Arc skeleton with all the branch points and end voxels. (d) Arc skeleton with branch and end voxels after tree merging and pruning. (e) Short path tree structure with all branch and end voxel. (f) Comparison between arc skeleton and short path tree structure, (g) Short path tree structure with different tree levels displayed as different colors after tree merging and pruning. (h) The volumetric representation of the artery tree after tree merging and pruning. (i) Color coding bar for (g, h)

a junction voxel. However, due to the existence of topological aberration in a digital space discussed in [119, 124] , junction voxels in an arc skeleton is defined as follows. An arc skeleton voxel p is an initial junction voxel if the number of object $\xi(p) > 2$ or either the number of tunnels $(\eta(p))$ or cavities $(\delta(p))$ is nonzero in $\mathcal{N}^*(p)$. Also, each component of initial junction voxels is replaced by simple junction voxel as follow. For each 26-component junction voxels, the final junction voxel p is defined as the arc skeleton voxel closest to the center of the gravity of component c. It may be noted that the final junction voxels form a set of isolated voxelss and in the rest of this section, by junction voxel, we will understand final junction voxels. End voxels in an arc skeleton are defined similarly expect that initial end voxels are defined as the set arc skeletal voxels with exactly one 26-adjacent arc skeletal voxels in its neighborhood. Results of junction and end voxel detection are shown in Figure 3.3(c). In the figure, arc voxels are shown blue, while junction voxels are shown in as red and green bullets, respectively.

3.4.3   Topologic Tree Generation

All junction and end voxels detected in the previous section are considered as tree nodes and other arc voxels are used to determine node connectivity. The main purpose of this step is to find connectivity among junction and end voxels. The method starts with manual identification the root node in the tree. This step is accomplished by indicating one of the junction or end node as the root node with a mouse click in a 3-D graphical interface. A major challenge in computing tree connectivity is that all nodes are arc interconnected in an arc skeletal tree. We solved
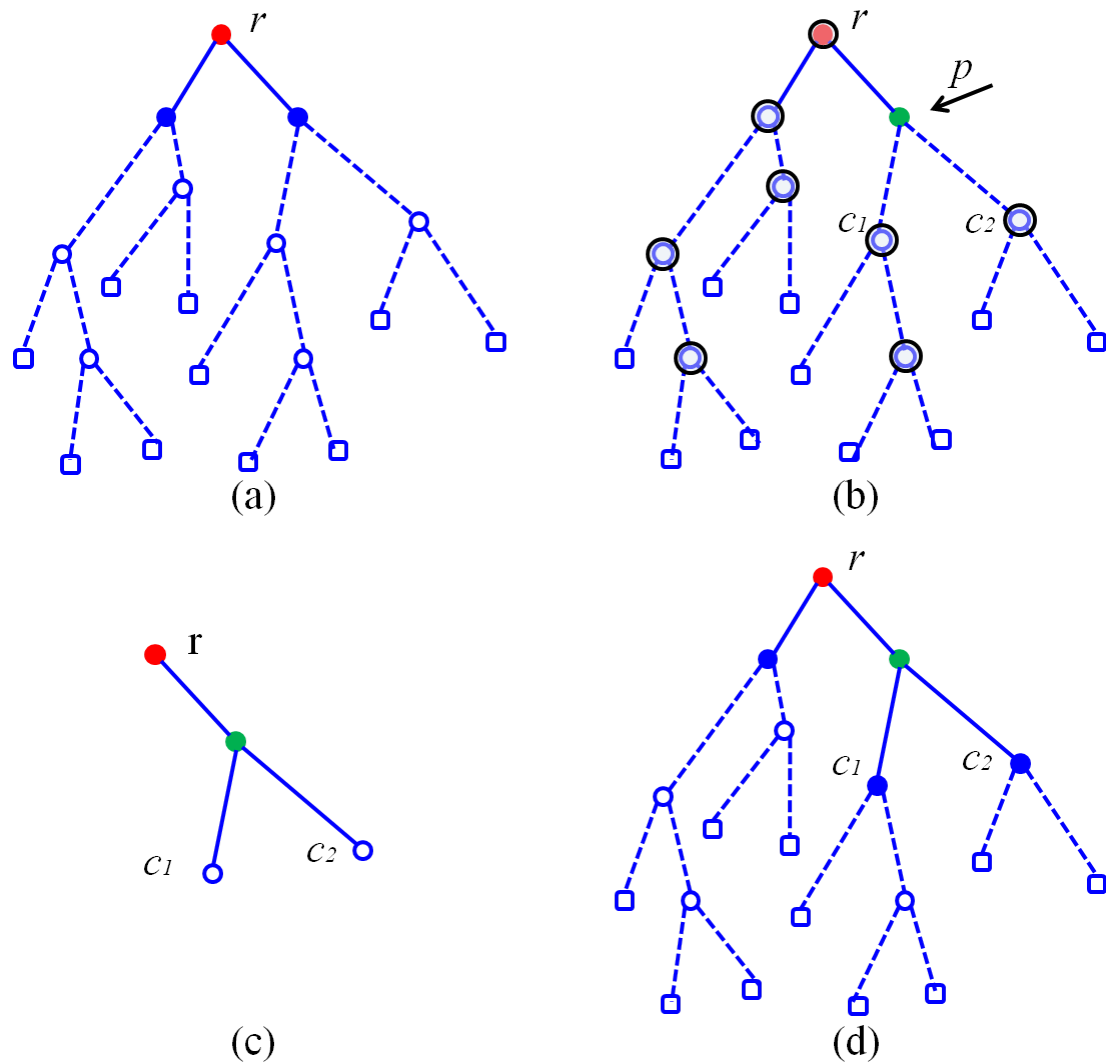
Figure 3.4: Illustration of the method computing tree connectivity. An intermediate result of tree connectivity analysis is shown in (a). Here the red dot indicate the root and solid dots and soild edge indicate the nodes and branch connectivities are already established in the tree. Suppose that we want to determine child nodes for the junction node p. First, the ungluing is applied around all junction nodes expect the candidate junction node p. then the connectivity from p in the tree (b)is computed (c). (d) All unprocessed nodes to which the connectivity from p expand are connected as child node of p.

this problem using the ungluing technique at junction originally introduced by Saha *et al.* [171] . Figure 3.4 illustartes the idea of computing tree-connectivity using ungluing approach. The algorithm is presented in the following.

begin compute-tree-connectivity

input:

    (1) arc skeleton A

    (2) set of junction nodes J

    (3) set of end nodes E

    (4) root node r

output: connected tree structure T_{node}, T_{edge}

auxiliary data structure: a sequential queue Q

initialization:

    $T_{node} = \{r\}$

    $T_{edge} = \{\}$

    $J' = J - \{r\}$

    push r in Q

while Q is not empty

    pop a node p from Q

    $A' = A$

    for all node $q \in J - \{p\}$

        for all $r \in \mathcal{N}(q) \cap A$

            $A' = A' - \{r\}$

$$X = \{q | q \in A' \text{ and 26-connected to } p \text{ in } A'\}$$

for all nodes $q \in J' \cup E$

    if $\exists r \in \mathcal{N}(q)$ and $m \in X$, s.t. r is 26-adjacent to m

$$T_{node} = T_{node} \cup \{q\}$$

$$T_{edge} = T_{edge} \cup \{edge(p, q)\}$$

        if $q \in J'$

$$J' = J' - \{q\}$$

            push q in Q

        else

$$E = E - \{q\}$$

end compute-tree-connectivity

The above algorithm successfully captures tree among connectivity junction and end nodes p and q suffers from the artifacts of arc skeletonization. However, the edge (p, q) between two nodes p and q suffers from the artifacts of arc skeletonization. In order to derive a better edge between two nodes p, q, we use the shortest path centrally passing along the volumeteric A/V structure. To ensure that the path passes centrally along the volumeteric A/V tree, we have used the following distance function $f_{dist}(p, q)$ between two 26-adjacent points p, q.

$$f_{dist}(p, q) = \frac{|p - q|}{min(FDT_{norm}(p), FDT_{norm}(q))}, \tag{3.3}$$

where $FDT_{norm}(\cdot)$ gives local scale normalized FDT value discussed in Section 2.3.1, in Chapter 2. Finally, the shortest path is computed using the following algorithm.

begin compute-shortest-path(p, q)

input:

    node p and q

    normalized FDT image: FDT_{norm}

    volumetric A/V tree: AV

output: shortest path $\pi_{p,q}$

auxiliary data structure

    shortest path distance transform image: $SPDT$

    shortest path connectivity image: SP

    a sequential queue Q

Initialization :

    for all $t \in AV$:

        $SP(t) = \text{t}$

        $SPDT(t) = \text{maxValue}$

    $SPDT(p) = 0$

    push p in Q

while Q is not empty

    pop a point t from Q

    for $s \in \mathcal{N}(t) \cap AV$

$$f_{dist}(s,r) = \frac{|s-t|}{min(FDT_{norm}(s),FDT_{norm}(t))}$$

$$\textbf{if } SPDT(s) > SPDT(t) + f_{dist}(s,t)$$

$$SPDT(s) = SPDT(t) + f_{dist}(s,t)$$

$$SP(s) = t$$

$$\text{push } s \text{ in } Q$$

$$\pi_{p,q} = \langle q \rangle$$

$$t = q$$

$$\textbf{while } r \neq p$$

$$\text{append } SP(t) \text{ in } \pi_{p,q}$$

$$t = SP(t)$$

$$\textbf{end } \text{compute-shortest-path}(p, q)$$

The resulted tree structure with the shortest path centrally passing along the volumetric A/V structure is shown in Figure 3.3(e) and compared with the skeletal tree structure which is shown in Figure 3.3(d). A zoomed in comparison between the shortest path and arc skeletal tree path is shown in Figure 3.3(f). It is observed that the short path representation produces relatively smoother connection between nodes in the tree structure, which is important to derive accurate measures for multi-level tree arc length and thickness/cross sectional area parameters.

It may be shown that the above defined shortest path satisfy metric properties, i.e.,

1. for all $p, q \in AV$, $\pi_{p,q} > 0$, if $p \neq q$ and '0' otherwise

2. for all $p, q \in AV$, $\pi_{p,q} = \pi_{q,p}$

3. for all $p, q, r \in AV$, $\pi_{p,r} + \pi_{r,q} > \pi_{p,q}$

3.4.4 Iterative Merging, Pruning, and Extraction of Multi-level Artery/Vein measures

The topologic tree generated using the algorithms, described in the previous section, successfully captures tree connectivity. However, it suffers from two major problems, primarily created at the time of arc skeletonization — (1) multiple junctions creates for single anatomic branching location and (2) noisy branches are created from protrusions and dents. These problems are solved using an iterative merging and pruning algorithm. A merging signal between a parent node p and a child node c is triggered where the nodes are spatially close as compared to their FDT values. However, before we describe the merging and pruning algorithms, we need to discuss the algorithm to compute different tree topologic and geometric measures associated to each node as stated at the beginning of Section 3.4. These measures are computed using the following recursive algorithm and used for iterative tree merging and pruning.

begin recursive-compute-tree-measures(T, p)

input:

    (1) tree data structure T

    (2) a root node $p \in T$ in the current subtree of T

    (3) Branch-Length-to-Parent-Node: branchLength for all nodes in T

output: updated Tree-Node values for each node in tree T

auxiliary data structure

    (1) Depth-from-the-Root: depth for all nodes in T

    (2) Height-from-the-Leaf: height for all nodes in T

    (3) Arc-length-from-the-farthest-Leaf: arcLength for all nodes in T

if p does not have a parent node // i.e., p is the root of T

    $p.depth = 0$

 else

    $p.depth = p.parentNode.depth + 1$

if p does not have any child node

    $p.height = 0$

    $p.arcLength = 0$

else

    for all $c \in childNodeList(p)$

        recursive-compute-tree-measures(T,c)

        $maxHeight = max_{c \in childNodeList(p)}(c.height)$

        $maxArcLength = max_{c \in childNodeList(p)}(c.arcLength + branchLenth(c, p))$

        $p.height = maxHeight + 1$

        $p.arcLength = maxArcLength$

end recursive-compute-tree-measures(T, p)

Three measurements for the entire tree is computed by invoking the recursive function "recursive-compute-tree-measures(T, $root$)" with the second parameter being the root of of the tree. The merging process is governed by the following algorithm.

begin recursive-tree-merging(T, p)

input:

    (1) tree data structure T

    (2) root node $p \in T$ in the current subtree of T

output: modified tree T after possible merging

auxiliary data structure

    numChild(n) : count for child nodes of each node $n \in T$

    chindNodeList(n) : child node list for each node $n \in T$

    Fuzzy Distance Transform image: FDT

for all $c \in childNodeList(p)$

    if $numChild(c) > 0$

        recursive-tree-merging(T,c)

        $FDT(p) = max_{m \in \mathcal{N}_5(p)}(FDT(m))$

        $FDT(c) = max_{n \in \mathcal{N}_5(c)}(FDT(n))$

        $FDT_{value} = max(FDT(p), FDT(c))$

        if $Dist(p,c) < 2 \times FDT_{value}$

            if $FDT(p) > FDT(c)$

                merge the child node c to p

$$\textbf{if } FDT(c) > FDT(p)$$

$$\text{merge the parent node } p \text{ to } c$$

end recursive-tree-merging(T, p)

The above algorithm is a recursive process which is initiated from the root node by invoking the function "recursive-tree-merging(T,$root$)". The process of merging a parent node p and a child node c in a tree structure is graphically illustrated in the Figure 3.5.
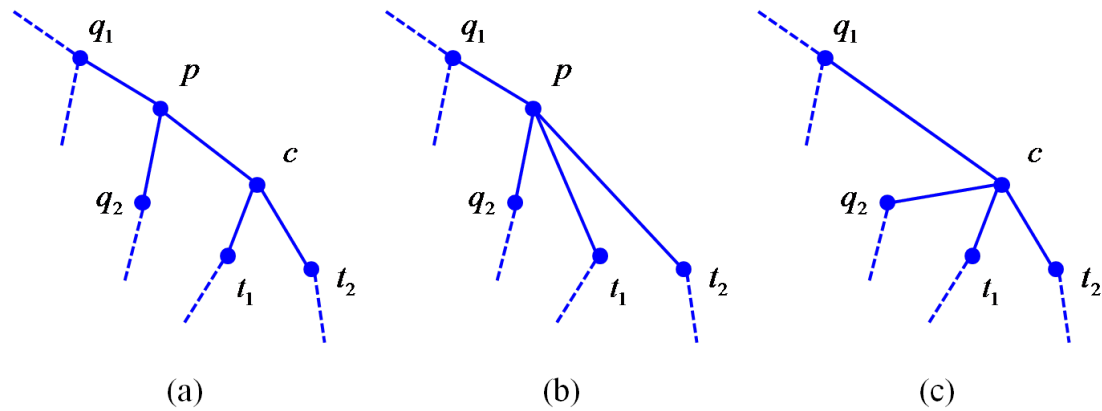
Figure 3.5: Tree operation of merging a parent node p and a child node c. (a) A part of a tree structure. (b) The result of merging the child node c to its parent node p. (c) The result of merging the parent node p to its child node c.

The pruning algorithm is applied on small subtree compared to the local tree size, which is governed by the following algorithm.

begin recursive-tree-pruning(T, p)

input:

    (1) tree data structure T

    (2) node $p \in T$ in the current subtree of T

    (3) a threshold on arc length: arcThr

    (4) shape distance transfrom image: SDT

output: modified tree T after pruning

auxiliary data structure

    numChild(n) : count for each node $n \in T$

    chindNodeList(n) : child node list for each node $n \in T$

    for all $c \in childNodeList(p)$

        if $numChild(c) > 0$

            recursive-tree-pruning(T, c)

            if $p.height > 3$ and $c.height < 1$ and $SDT(p) < arcThr$

                prune the subtree starting form the node c

            if $p.height > 5$ and $c.height < 2$ and $SDT(p) < arcThr$

                prune the subtree starting form the node c

end recursive-tree-pruning(T, p)

After merging and pruning process for the tree, the tree structure at different levels is determined using simple tree-analysis algorithm and the shortest path information between two nodes. Let edge (p, q) denote the sequence of voxels on the shortest path between two junction voxels p, q derived using the shortest path

computation algorithm described in Section 3.4.3. A multi-level tree representation may be computed as a digital image with tree-level information on the digital tree representation by invoking the following recursive algorithm with root being the node parameter.

begin recursive-multi-level-tree-generation(p)

input:

(1) tree data structure T

(2) root node $p \in T$ in the current subtree of T

(3) edge $(s,\ t)$ for every adjacent pair of node $s,\ t \in T$

output:

DigitalTree: A digital image representing the multi-level

digital representation

if p does not have a parent node //i.e., p is a root node

$p.depth = 0$

else

$p.depth = p.parent.depth + 1$

$DigitalTree(p) = p.depth + 1$

if $numChild(p) \neq 0$

for all $c \in ChildNodeList(p)$

for all $q \in edge(p,c) - \{c\}$

$DigitalTree(q) = p.depth + 1$

recursive-multi-level-tree-generation(c)

end recursive-multi-level-tree-generation(p)

Results of multi-level digital tree computation is shown in Figure 3.3(g) where different color is used to denote tree level, see Figure 3.3(i) for color coding scale. The most challenging part of multi-level tree generation is accomplished at this stage. The final stage in tree generation cascade is to propagate the multi-level tree information from one voxel thick shortest path information to the original volumetric representation. This step is solved using the feature propagation algorithm proposed in [135]. The basic idea of feature propagate can be shown in two stages — (1) initiate tree-level at each voxel p on the shortest-path digital tree representation DigitalTree(p) and (2) inherit tree-level at other voxels on the volumetric representation from its nearest shortest path digital tree point. The computational problem of the feature propagation is solved using the same dynamic programing algorithm proposed in [95], where the distance as well as closet voxel information are simultaneously propagated through a wave propagation technique. The result of volumetric multi-level tree representation of the same arterial tree is illustrated in Figure 3.3(h), and the same color coding scale of Figure 3.3(i) is used. As observed in Figure 3.3(g, h), the results of multi-level tree represention are visually satisfactory.

3.5   Experimental Methods and Results

In this section, we describe the accuracy and reproducibility of the multi-generated tree computation algorithm described in Section 3.1 to 3.4. The over-

all objective of our experimental plan for tree analysis is to examine the accuracy and reproducibility of our algorithm to generate multi-level tree representation for arterial/venous tree and to extract vascular measurements at different tree levels. Specifically, the accuracy of the algorithm has beed evaluated using computerized mathematical phantoms. Reproducibility of the method has been evaluated using pulmonary CT images of a pig vessel cast phantom and multi-user A/V separation of *in vivo* contrast-enhanced CT images of a pig lung at different respiratory volumes. In the rest of this section, I will describe experimental methods to evaluate accuracy and reproducibility of our tree analysis method.

3.5.1 Accuracy Analysis on Computer Generated Phantoms

It is difficult to generate ground truth for multi-level tree representations in *in vivo* pulmonary images of an animal or a human subject. Even for *in vivo* image of animal and the CT image of the cast phantom of pig lung, it is still difficult to obtain the ground truth for the volumetric multi-level tree information for the whole arterial/venous tree. We have designed our experimental plans to examine the accuracy of our tree analysis method using computer generated phantoms. Five computer generated phantoms have been created. In these computer generated phantoms, there are several branch levels with different scales along the structure, designed to evaluate the performance of our tree analysis method at the bifurcation locations and the various scales along the structure (see Figure 3.6).

The accuracy of the tree analysis method was evaluated by comparing how much with the tree analysis results using our method matches with the ground truth
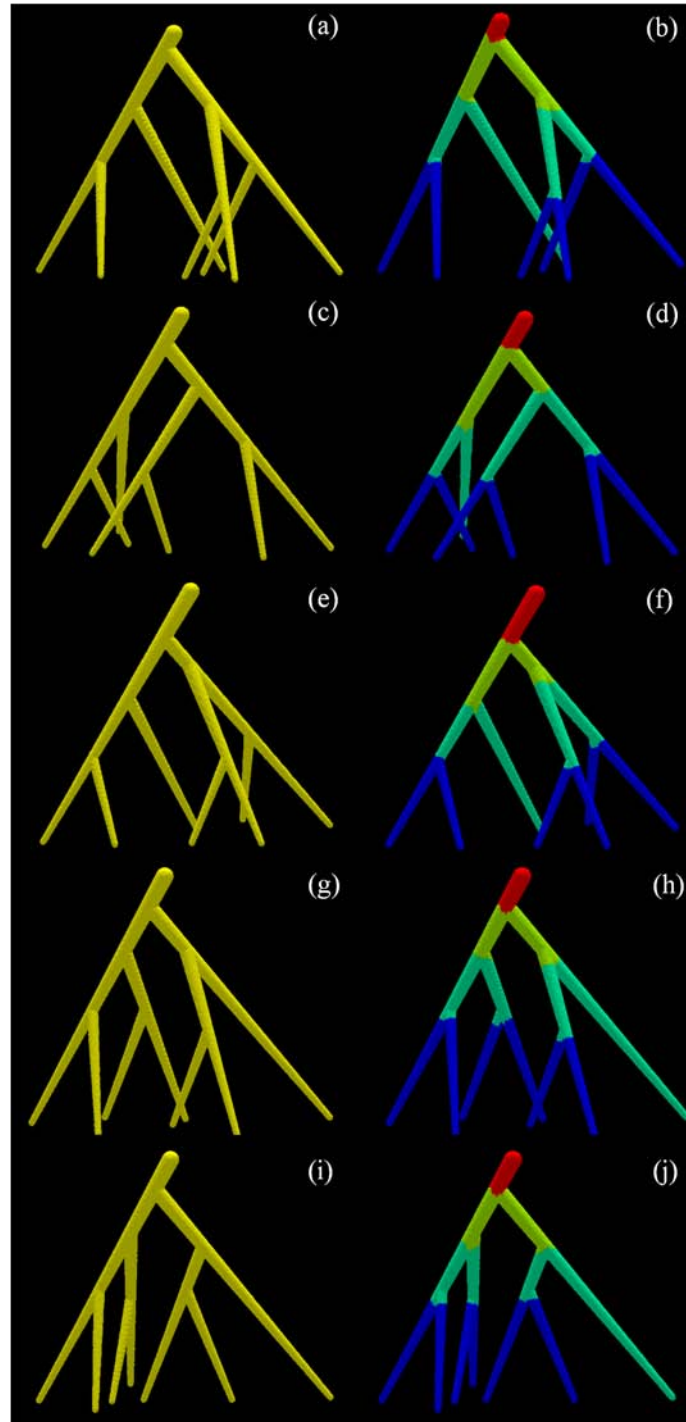
Figure 3.6: Results of tree generation and analysis on phantoms. (a) Computer generated phantom with four branch levels, (b) Volumetric multi-level tree presentation of the phantom, using different colors showing different branch levels. (c,d), (e,f), (g,h) and (i,j) are other phamtons

volumetric information in terms of total volume, tree arc and cross section area of the structure at each level. The ground true is calculated during phantom generation using a similar technique described in Section 2.4.1.1 in Chapter 2. Such comparison were applied for each phantom at each branch level. We computed vascular volume error, branch length error and cross section area error as the percent of difference between true and computed measurements defined as follows:

$$Volume_{Error} = \frac{Volume_{true} - Volume_{computed}}{Volume_{true}}. \tag{3.4}$$

$$BranchLength_{Error} = \frac{BranchLength_{true} - BranchLength_{computed}}{BranchLength_{true}}. \tag{3.5}$$

$$CrossSectionArea_{Error} = \frac{CrosssectionArea_{true} - CrosssectionArea_{computed}}{CrosssectionArea_{true}}. \tag{3.6}$$

The quantitative result on computer generated phantoms are shown in Tables 3.1, 3.2 and 3.3.

For all multi-level measurements, the error was calculated as the percent of difference from the true measurement. As observed in these tables most of normalized errors at different tree levels fall in the interval of $[-5\%, 5\%]$. By observing the illustrations of Figure 3.6, we noted that most errors took place near junctions. It

should be mentioned here that the multi-level delineation near junctions is difficult to define theorectically and which partially contribute to the error.

Table 3.1: Results of quantitative error analysis of computed vascularvolume at different tree levels for five computer generated phantoms.

Phantom	level 1	level 2	level 3	level 4
A	3.19%	1.68%	4.50%	1.20%
B	1.27%	1.57%	1.24%	-2.73%
C	1.36%	2.62%	1.76%	1.31%
D	1.33%	2.54%	1.18%	-4.76%
E	1.35%	2.12%	5.67%	-1.72%

Table 3.2: Results of quantitative error analysis of computed branch length at different tree levels for five computer generated phantoms.

Phantom	level 1	level 2	level 3	level 4
A	2.56%	-2.50%	-8.18%	5.66%
B	1.20%	-5.58%	1.73%	-5.95%
C	0.63%	4.91%	1.00%	-0.75%
D	1.41%	3.78%	2.72%	-2.52%
E	1.22%	0.93%	0.89%	-2.98%

3.5.2   Reproducibility Analysis Cast Phantom of a Pig Lung

In the pig vessel cast phantom, arterial side was contrast-enhanced, therefore ground truth of arterial and venous tree can be obtained by thresholding. We applied tree analysis both on ground truth of artery/vein tree as well as the artery/vein tree

Table 3.3: Results of quantitative error analysis of computed cross section area at different tree levels for five computer generated phantoms.

Phantom	level 1	level 2	level 3	level 4
A	1.08%	-3.38%	4.76%	6.92%
B	1.55%	2.04%	-5.57%	2.04%
C	0.78%	-4.4%	-0.9%	1.95%
D	1.27%	-1.92%	-2.01%	1.69%
E	1.07%	1.32%	5.52%	1.83%

computed using our algorithm. Result of application of multi-level tree analysis is displayed in Figure 3.7. Multi-level volumetric tree representation of both artery and vein on contrast separated and algorithm-separated results show nice visual agreements

Three quantitative tree measurements, namely, vascular volume, length of branches and cross section area were computed at different tree levels. Agreement of the these measurement was studied at each level. The results of graphical comparative analysis are summarized in Figure 3.8, 3.9, 3.10, 3.11, 3.12 and 3.13. From these figures, we can see that at higher tree levers the tree measurements from the contrast-separated arterial/venous trees and the computed arterial/venous trees using method described in Chapter 2, match with each other better than at lower tree levels. The possible reason is the starting points of the arterial/venous tree are not identified at the same, even similar locations. During vasculature segmentation in cast phantom CT images, vessel tree has to be separated from the heart region and all other non-vessel structure. It is quite difficult to cut the vessel tree at the same location for different phantoms.
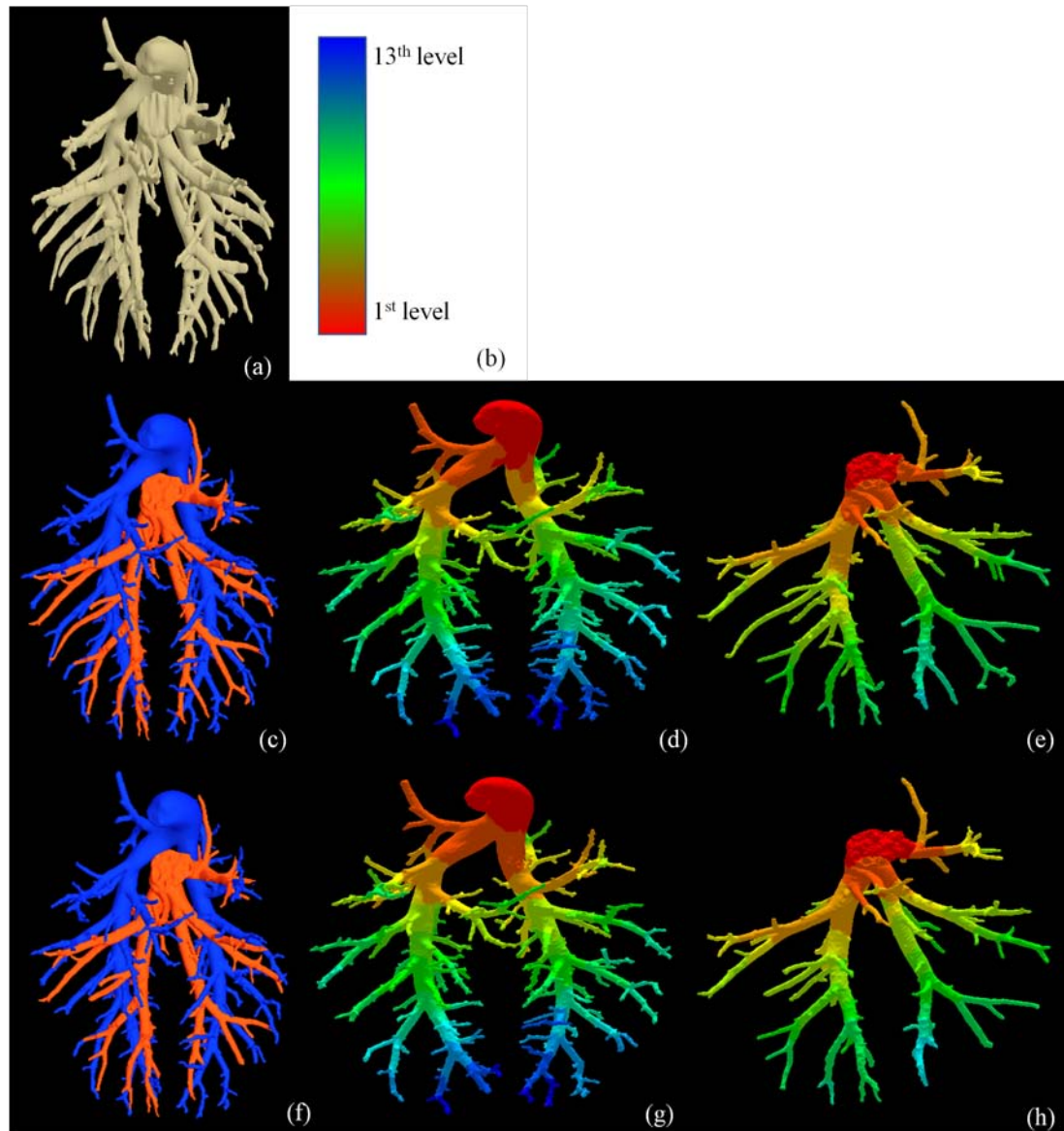
Figure 3.7: Results of multi-level tree analysis on pulmonary pig vessel cast. (a) 3-D reconstruction of pulmonary vessel cast. (b)Color coding bar for (c-h). (c-e) Contrast separated A/V separation(c) and multi-level volumetric tree representations for arteries(d) and veins(e). (f-h) Same as (c-e) but on A/V separation using the method describe in Chapter 2.

108

I performed intraclass correlation(ICC) analysis of vascular volume for the arterial/venous tree segmented from CT images of vessel cast of pig lung at various slice thickness and slice spacing. Here, measurement at each tree level is considered as a event, while arterial/venous trees computed using contrast information and using method describe in Chapter 2 are considered as obervations. Suppose there are N levels in the arterial/venous tree, the definition of intraclass correlation of vascular volume was defined as follows:

$$ICC_{volume} = \frac{\frac{1}{N}\sum_{n=1}^{N}(x_{1,n} - \bar{x})(x_{2,n} - \bar{x})}{\frac{1}{2N}\sum_{n=1}^{N}(x_{1,n} - \bar{x})^2 + (x_{2,n} - \bar{x})^2} \tag{3.7}$$

where $x_{1,n}$ is the vascular volume value of the arterial/venous tree computed using contrast information at tree level n; $x_{2,n}$ is the vascular volume value of arterial/venous tree computed using the method in Chapter 2 at tree level n; $\bar{x}$ is the overall average vascular volume values at different tree levels in arterial/venous trees computed using the above two methods. Results of intraclass correlation as shown in Table 3.4.

3.5.3   *In vivo* CT Image of Pig Lung

The *in vivo* CT images used in Chapter 2 (see Figures 2.12 and 2.13) were used to study the reproducibility of A/V separation at different airway pressure — 7.5cm, 12cm and 18cm H_2O PEEP. Multi-level volumetric reproducibility of arterial/venous trees at different airway pressure are illustrated in Figure 3.14. To evaluate the reproducibility of the tree analysis method , we used A/V separation results from two mutually blinded users. The experimental process we followed is that two groups of

Table 3.4: Results of intraclass corrlation on vascular volume evaluated on arterial/venous trees from CT images of pulmonary vessel cast of a pig lung reconstructed with different combinations of slice thickness and slice spacing

Slice Thickness (mm)	Slice Spacing(mm)	Artery	Vein
0.6	0.4	0.9982	0.7980
0.6	0.6	0.9987	0.8429
0.75	0.5	0.9715	0.9542
0.75	0.75	0.8960	0.9053
1.0	0.8	0.8606	0.9261
1.0	1.0	0.8221	0.9421
1.5	1.2	0.7384	0.7884
1.5	1.5	0.8751	0.9751
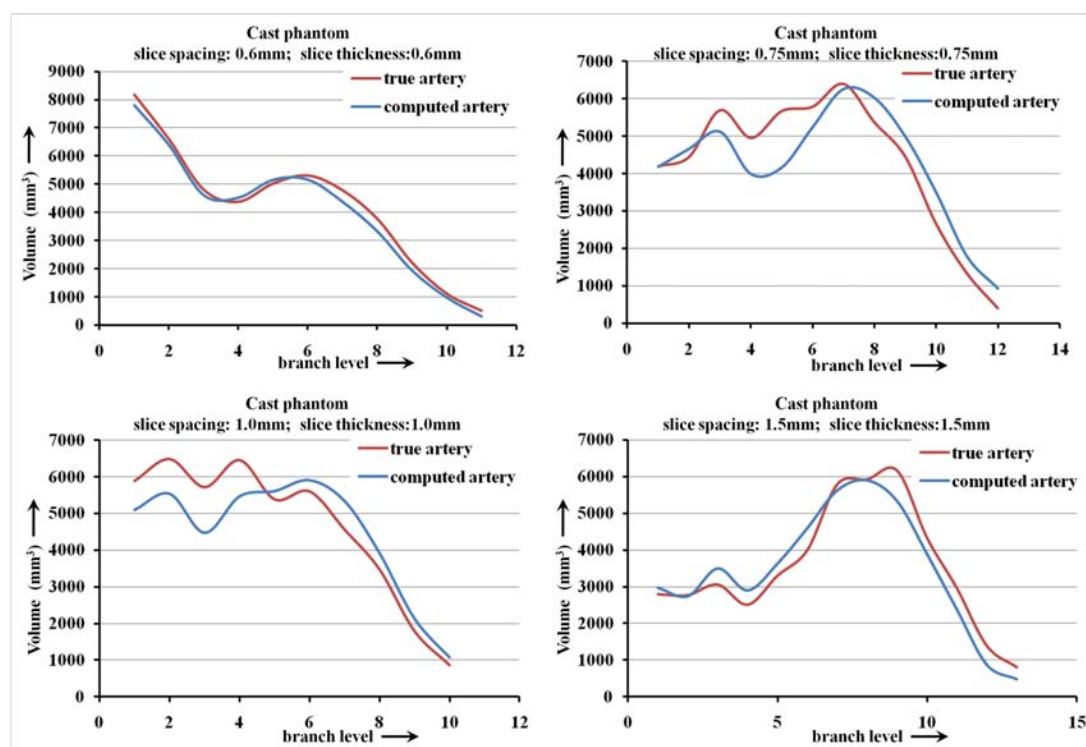
Figure 3.8: Graphical illustration of agreements between computed vascular volumes at different tree levels from the arterial structure in contrast separation and computed arterial tree using method described in Chapter 2.
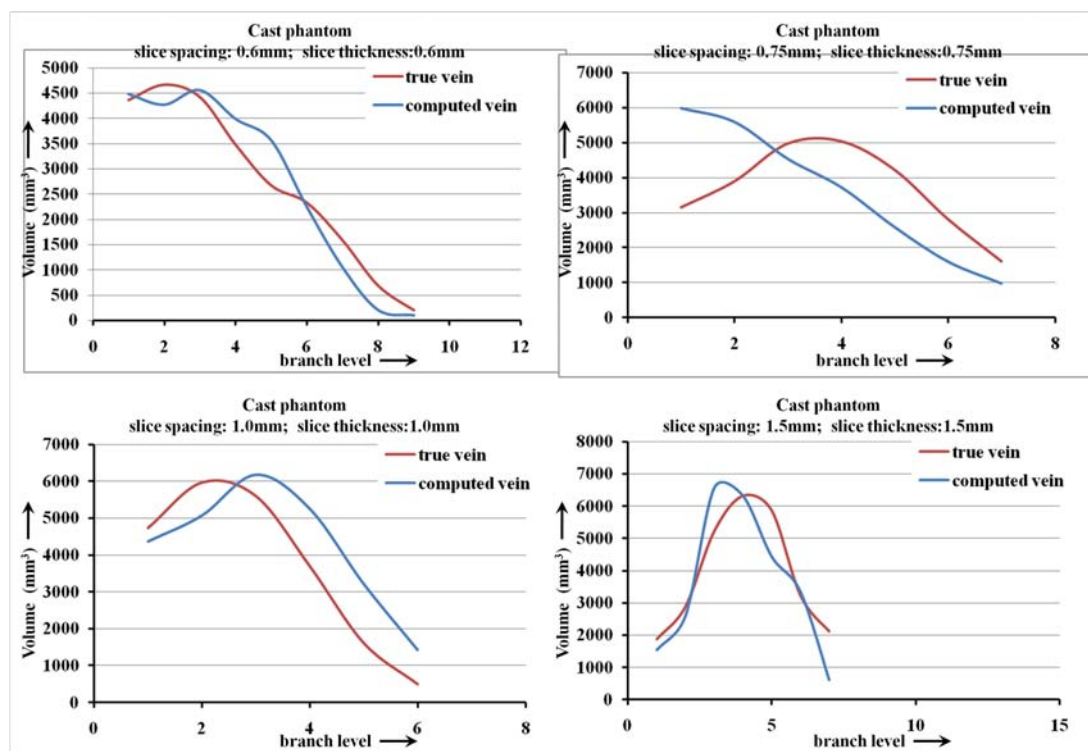
Figure 3.9: Graphical illustration of agreements between computed vascular volumes at different tree levels from the venous structure in contrast separation and computed venous tree using method described in Chapter 2.
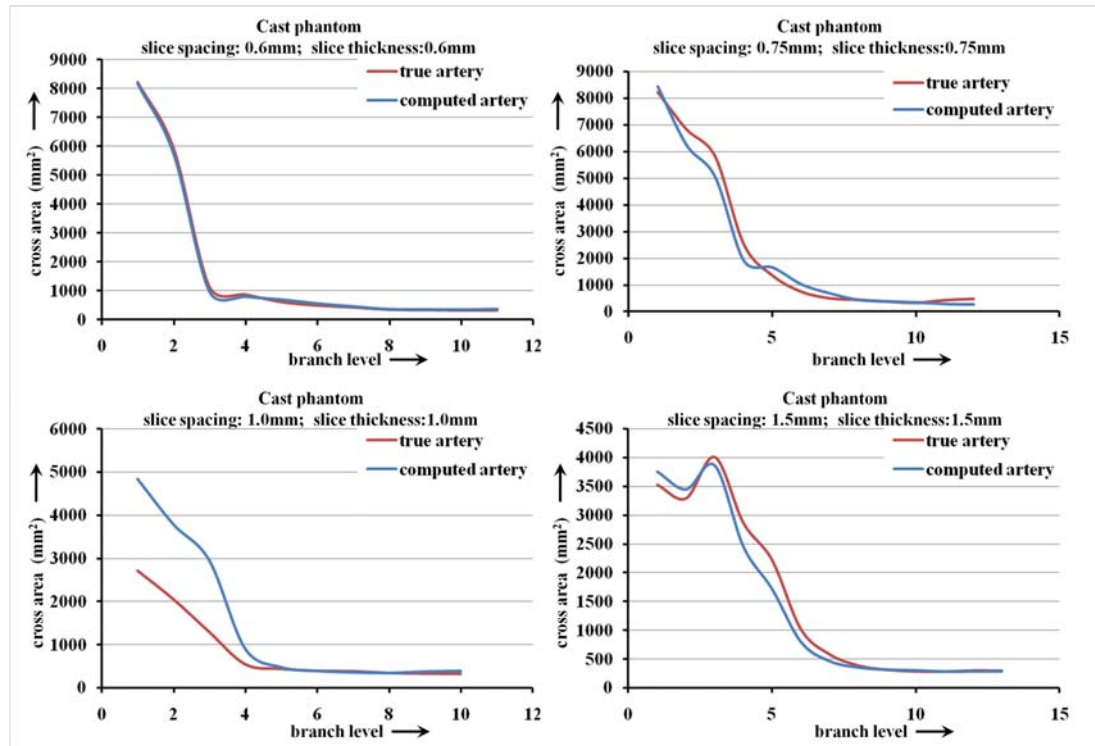
Figure 3.10: Graphical illustration of agreements between computed cross section areas at different tree levels from the arterial structure in contrast separation and computed arterial tree using method described in Chapter 2.
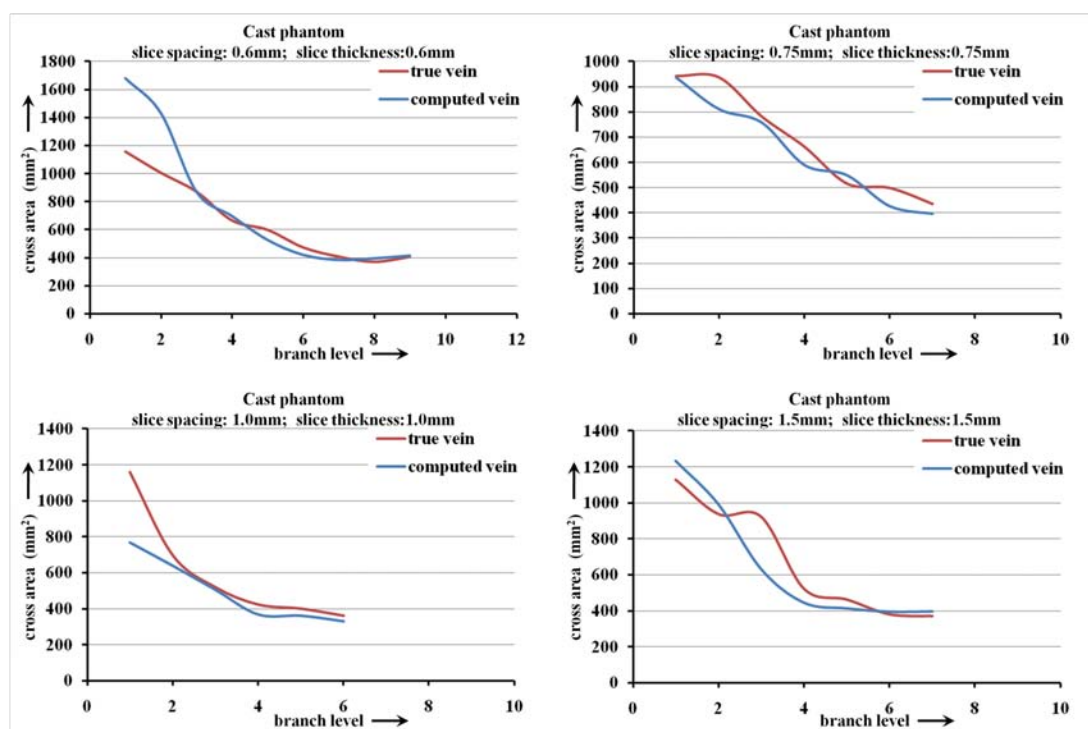
Figure 3.11: Graphical illustration of agreements between computed cross section areas at different tree levels from the venous structure in contrast separation and computed venous tree using method described in Chapter 2.
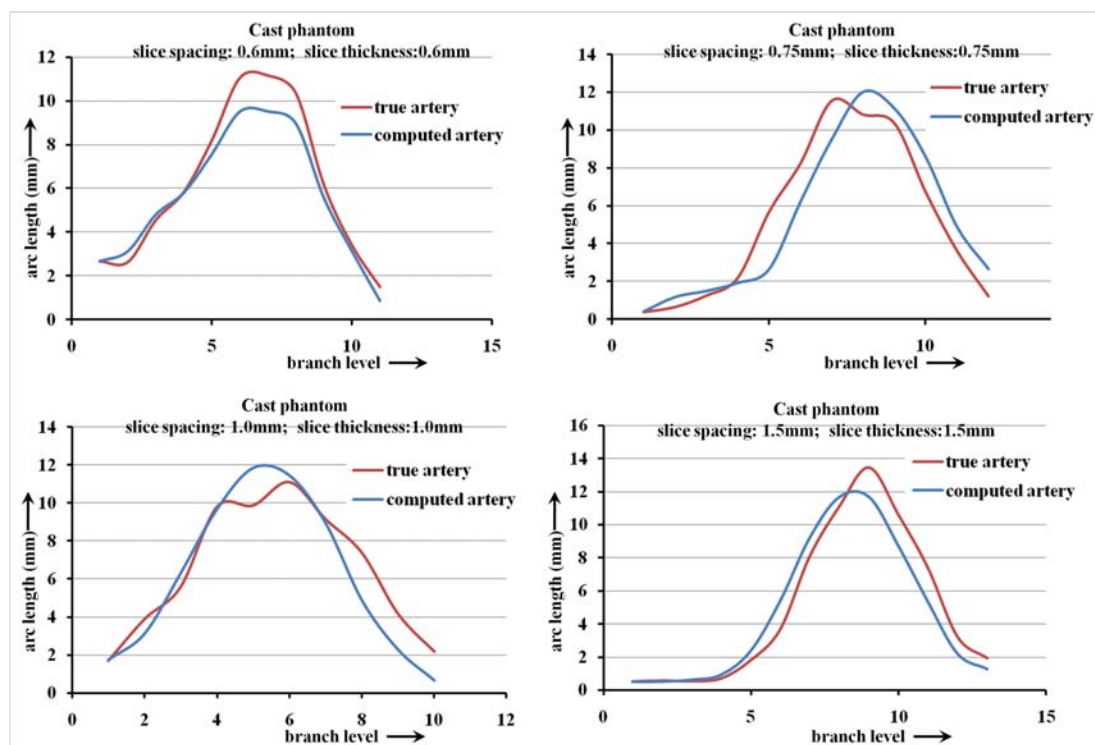
Figure 3.12: Graphical illustration of agreements between computed branch lengths at different tree levels from the arterial structure in contrast separation and computed arterial tree using method described in Chapter 2.
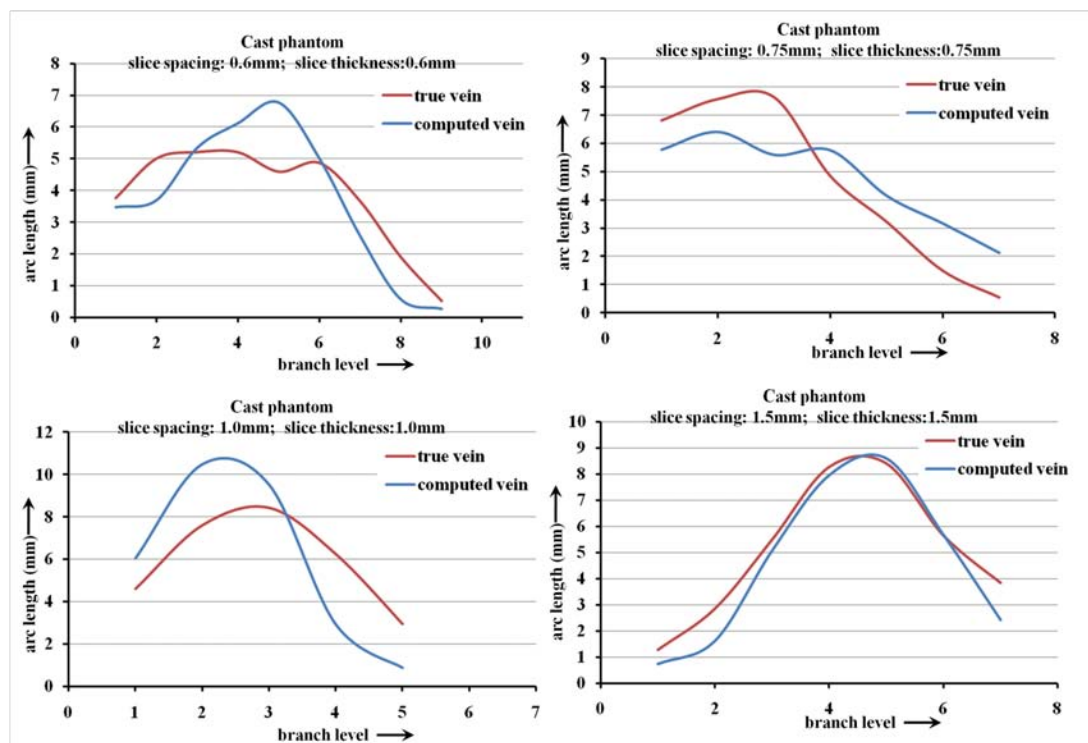
Figure 3.13: Graphical illustration of agreements between computed lengths at different tree levels from the venous structure in contrast separation and computed venous tree using method described in Chapter 2.
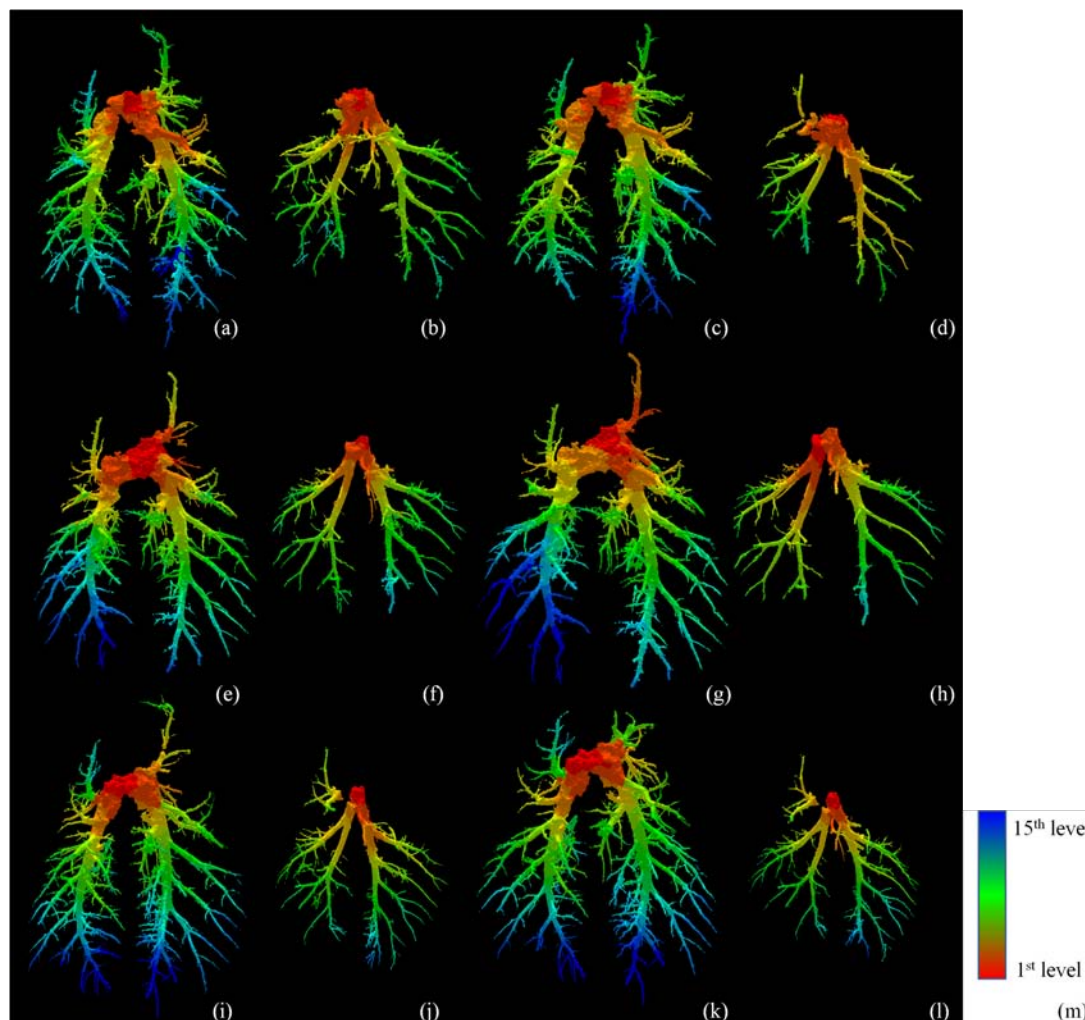
Figure 3.14: Results of quantitative tree analysis on *in vivo* pulmonary CT image of a pig lung under three different airway pressures. (a-d) Multi-level representation of arterial (a, c) /venous (b,d) tree of pig lung on 7.5cm H_2O PEEP, using the multi-level tree analysis method. (a, b) are results based the artery/vein separation using seeds selected by user1 and (c, d) are the results based on user2. (e-h) and (i-l) are the same as (a-d) expect at 12 and 18 cm H_2O PEEP

seeds from two independent mutually blinded users were used to separate artery/vein and then apply tree analysis on these two sets of artery/vein separation results. Since the artery/vein separation results based on seeds selected by two users will be quite similar with differences at various locations. We compared the tree measurements at different tree levels for two arterial/venous trees, obtained using seeds from two users and check the reproducibility of our tree analysis method. The comparison results are graphically illustrated in Figure 3.15, 3.16, 3.17, 3.18, 3.19 and 3.19. From those figues, we can see that the measurements at different tree levels of A/V trees computed using seed selected by two independent users match with each other quite well except at lower levels in respective trees and some other noisy locations. These results confirmed that our multi-level tree analysis method can produce consistent measurements at different tree levels.

Also, we conducted intraclass correlation analysis of vascular volume using observations at different tree levels. Here, vascular volume at different tree levels is considered as a event, while arterial/venous trees computed using seeds selected by two independent users are considered as obervations. The intraclass correlation was defined similarly to the one in Section 3.5.2, expect $x_{1,n}$ and $x_{2,n}$ are the vascular volume value at tree level n of the arterial/venous trees computed using seeds selected by user 1 and user 2, respectively. The results of intraclass correlation analysis are summarized in Table 3.5.
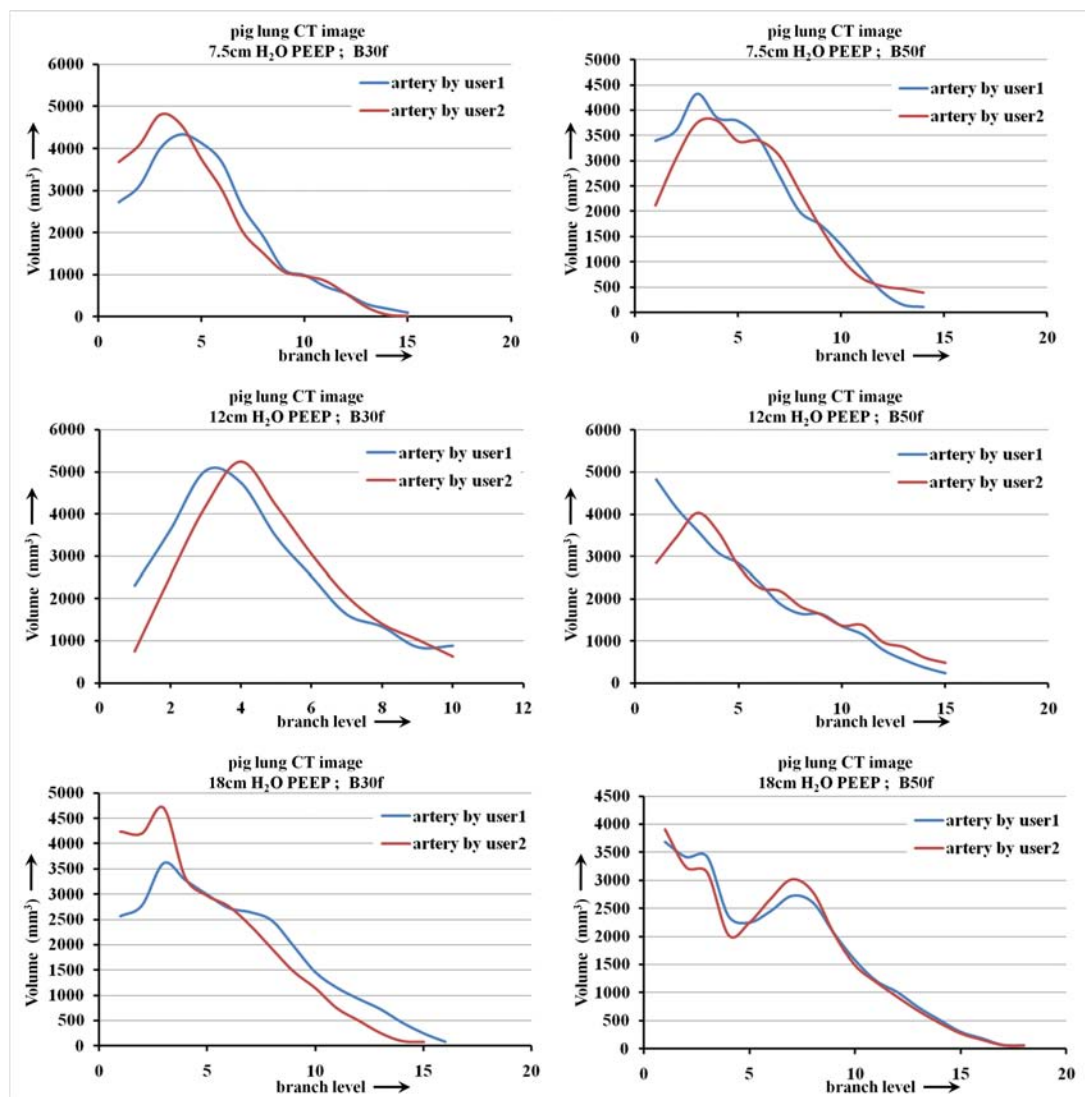
Figure 3.15: Results of quantitative analysis of computed volume at different tree levels for the arterial trees generated using seeds selected by two independent users.
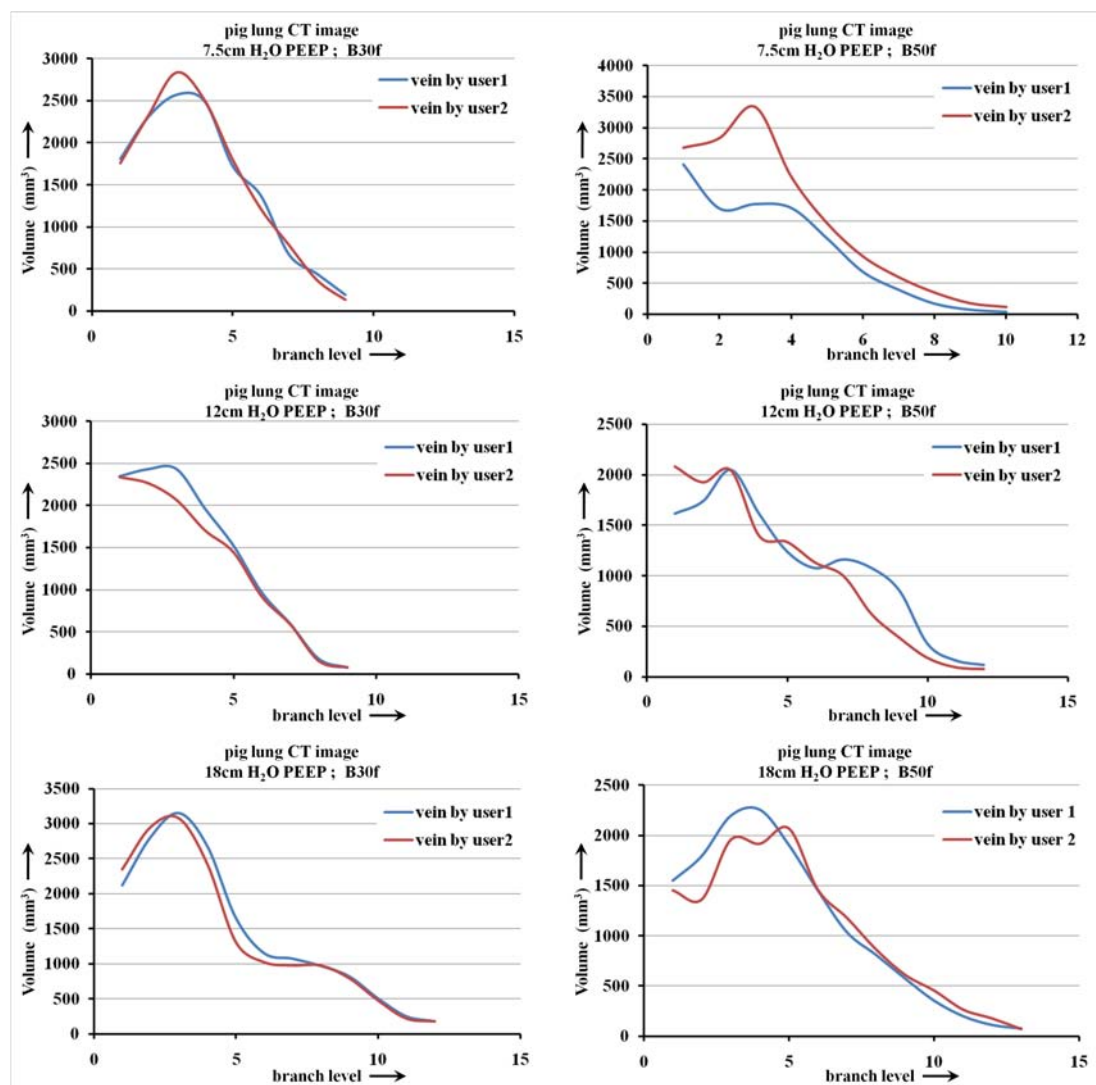
Figure 3.16: Results of quantitative analysis of computed volume at different tree levels for the venous trees generated using seeds selected by two independent users.
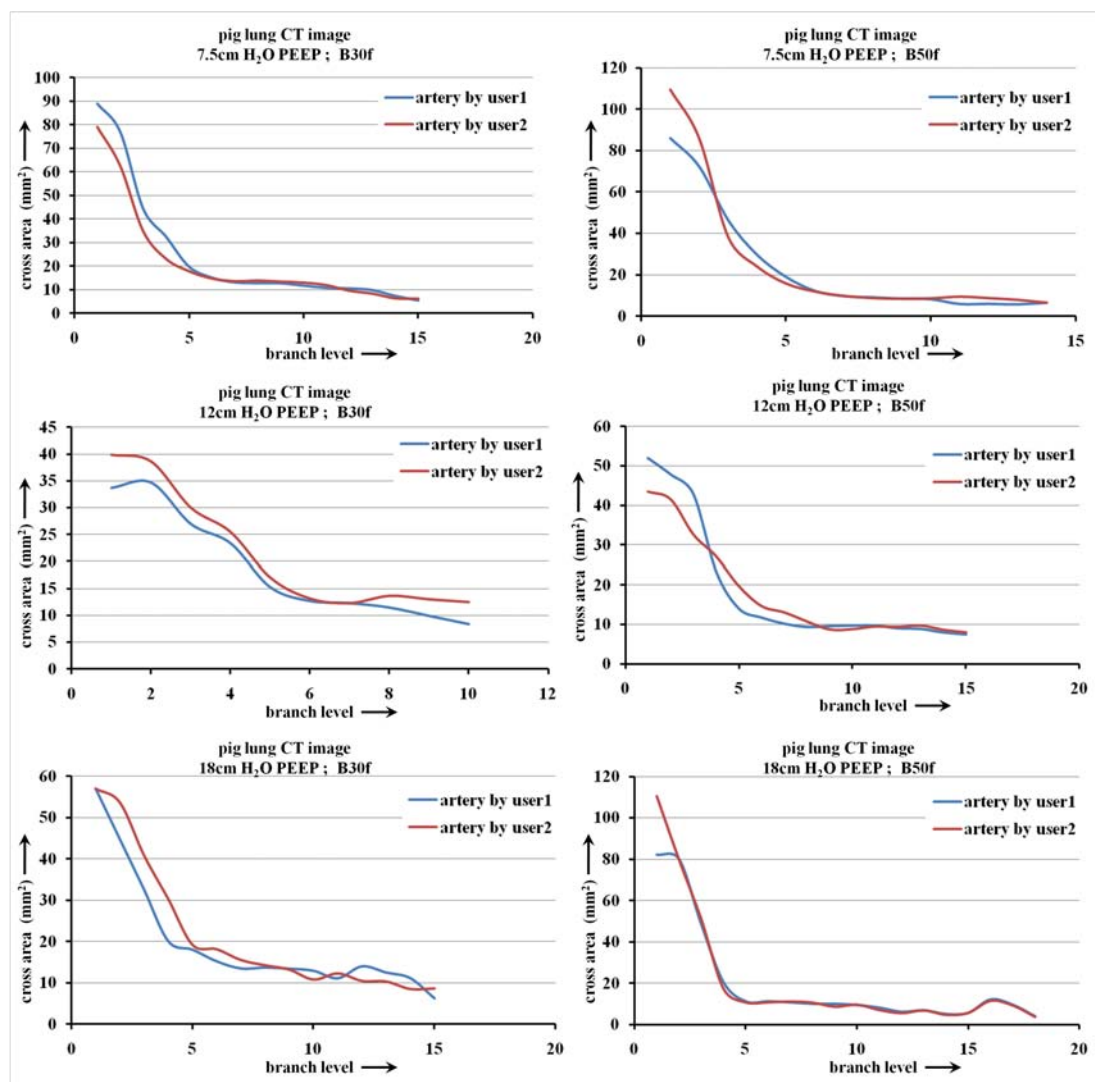
Figure 3.17: Results of quantitative analysis of computed cross section area at different tree levels for the arterial trees generated using seeds selected by two independent users.
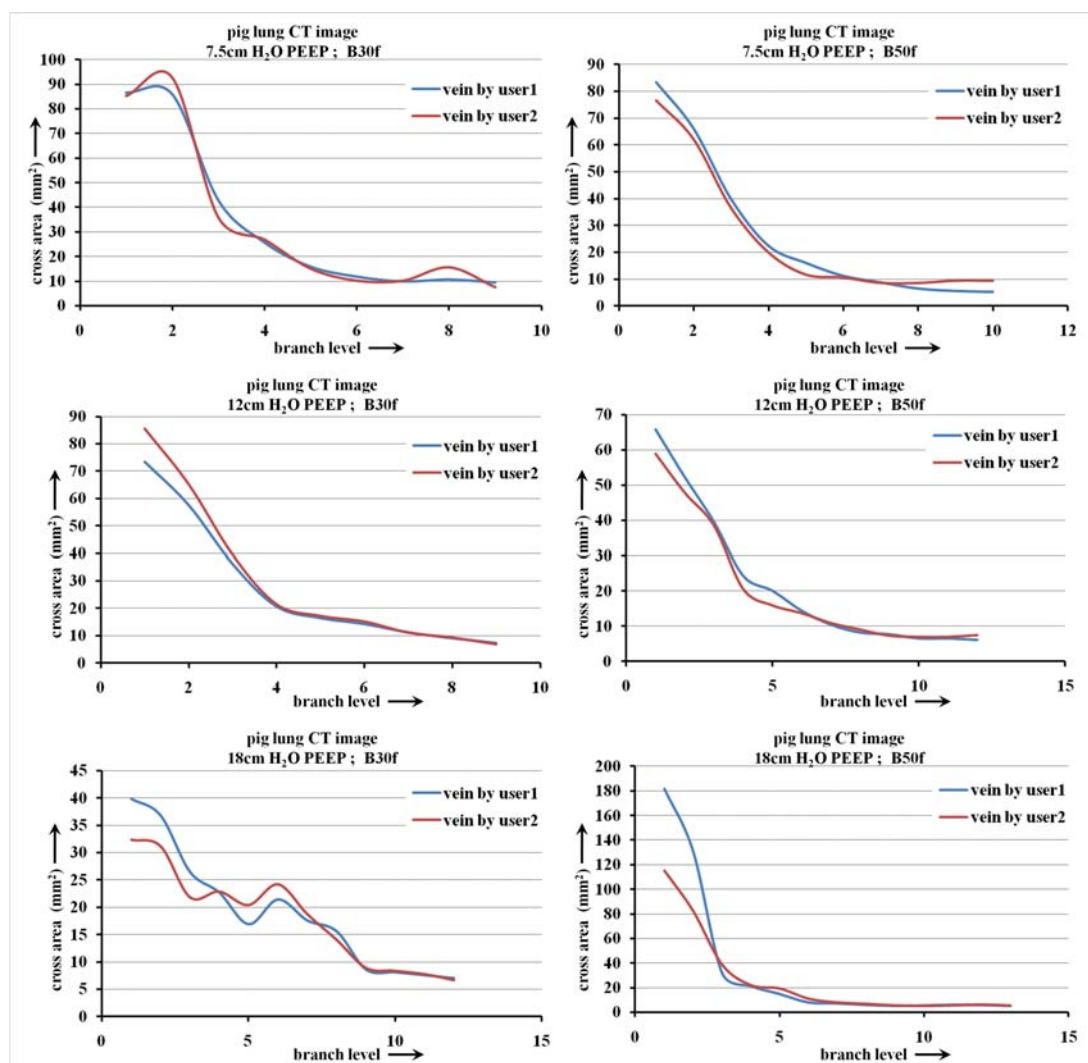
Figure 3.18: Results of quantitative analysis of computed cross section area at different tree levels for the venous trees generated using seeds selected by two independent users.
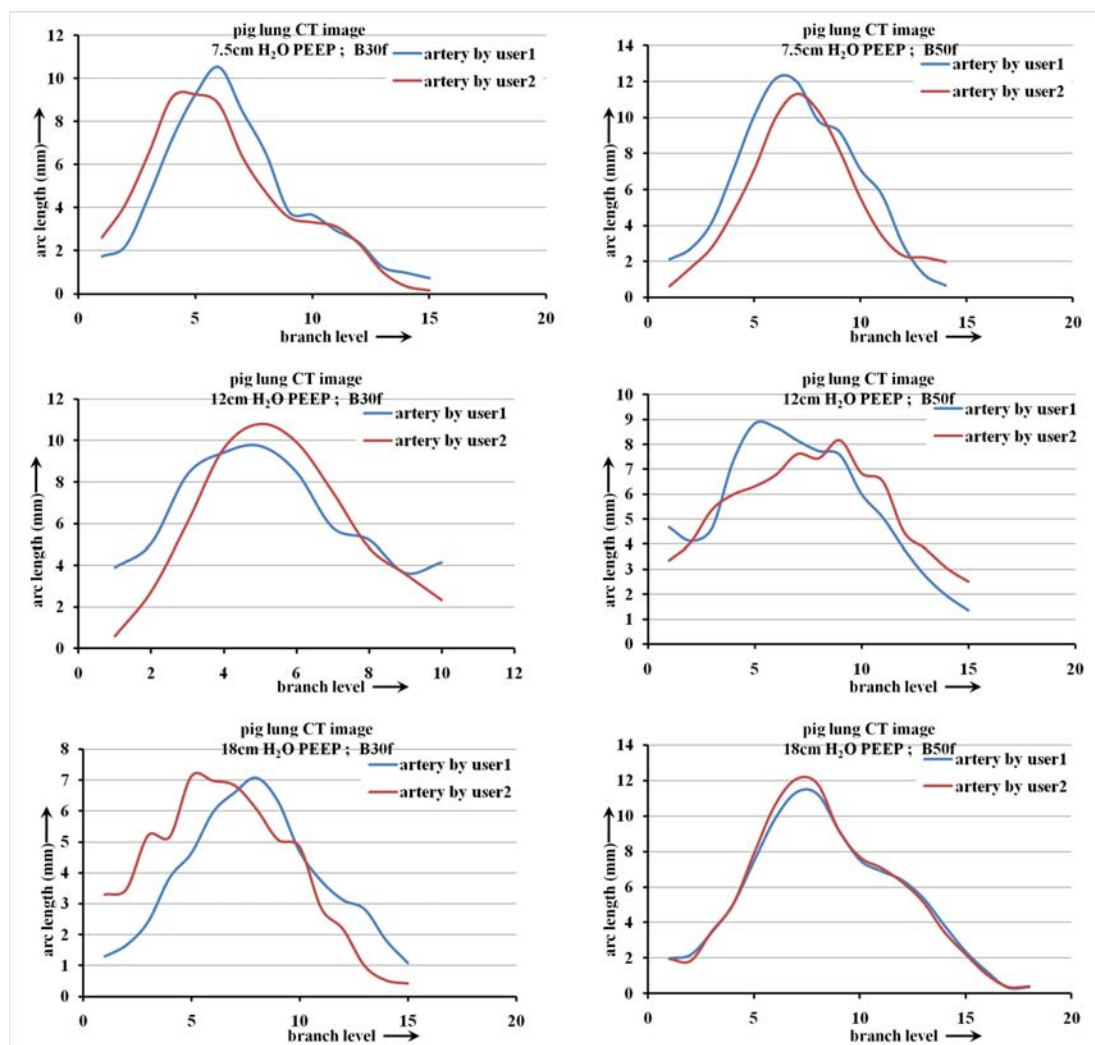
Figure 3.19: Results of quantitative analysis of computed branch length at different tree levels for the arterial trees generated using seeds selected by two independent users.
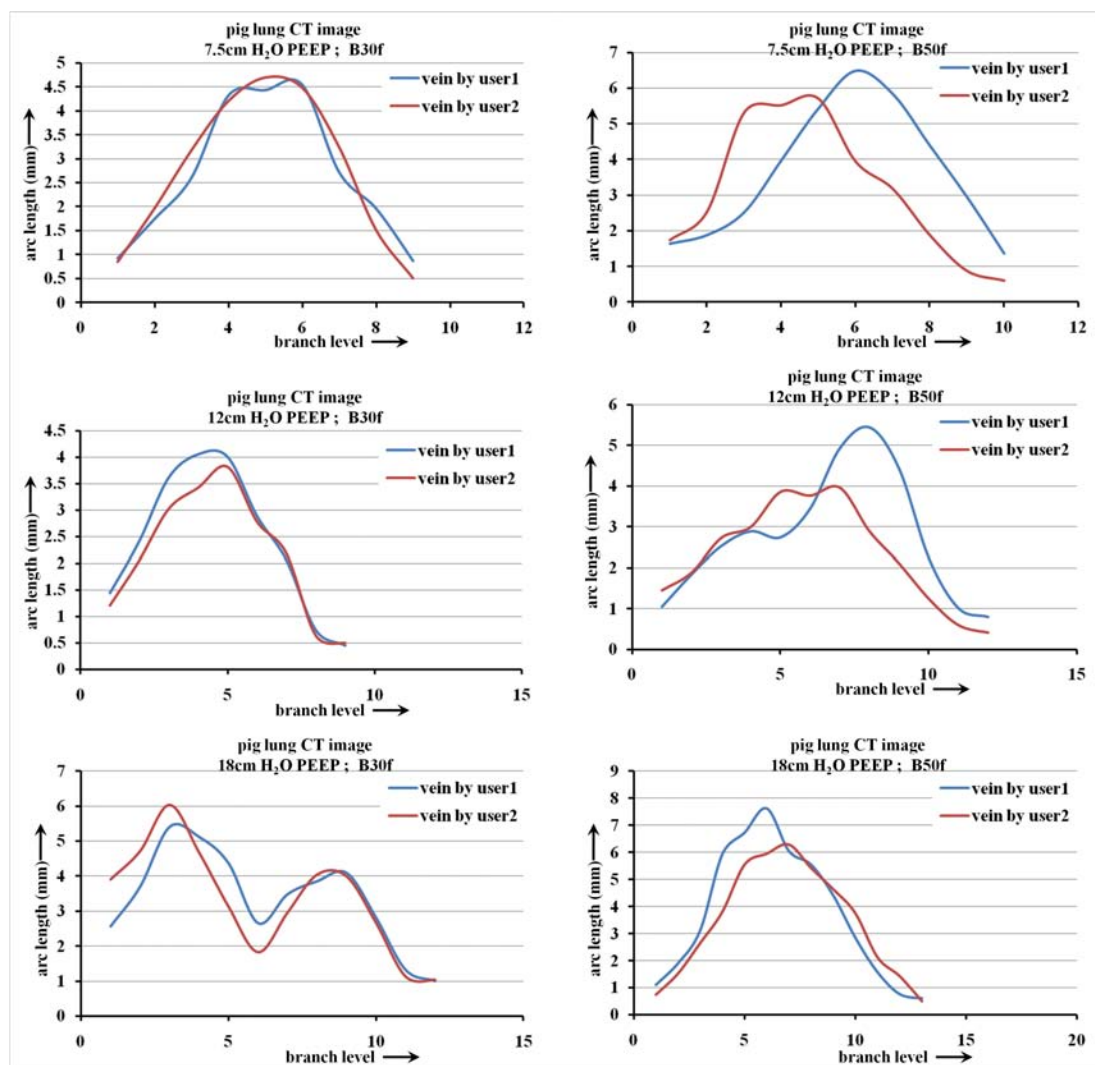
Figure 3.20: Results of quantitative analysis of computed branch length at different tree levels for the venous trees generated using seeds selected by two independent users.

Table 3.5: Results of intraclass correlation of vascular volume on artery/vein trees from *in vivo* pulmonary CT images of a pig lung at three different PEEP values (7.5cm, 12cm , 18cm H_2O) and reconstructed with two different kernels(B30f and B50f).

		7.5 cm H_2O	12 cm H_2O	18cm H_2O
B30f	Artery	0.9387	0.9366	0.6916
	Vein	0.9243	0.9573	0.9780
B50f	Artery	0.8600	0.7241	0.9724
	Vein	0.8359	0.8641	0.8798

CHAPTER 4
TENSOR SCALE BASED CONSTRAINED REGION GROWING FOR PULMONARY VESSEL SEGMENTATION IN NON-CONTRAST CT IMAGING

4.1 Introduction

In this Chapter, I present a new algorithm to segment pulmonary vasculature in non-contrast CT imaging of human subjects. We have developed a new constrained region growing algorithm to solve the problem. The idea of constrained region growing is to design a region growing algorithm that encourage growth along a structure while arresting cross-structure leaking. The basic foundation of constrained region growing based on fuzzy connectivity approach originally introduced by Rosenfeld [111] and late popularized by Udupa, Saha and others [160, 126]. The novelty of constrained region growing to update local parameters in a direction-dependent function using local scale information leading to a completely anisotropic region growing mechanism. Here, we have used tensor scale, an ellipsoidal representation of local structures, to control the anisotropic constrained region growing algorithm. This chapter is organized in four sections including the current one. In the second section, I formulate and describe the basic idea of tensor scale. The theory and algorithms for constrained region growing in presented in Section 3. Section 4 describes our experimental plans and results.

4.2   Tensor Scale

In this section, I present the basic idea and definition of for tensor scale originally introduced by Saha et al. [117]. Saha [117] described tensor scale using an algorithmic approach and a precise analytic definition has been missing. Although, tensor scale may be useful in several image processing and computer vision applications [117], previous algorithmic framework is unrealistic for three- and higher-dimensional images due to high computational complexity. Recently, Saha and Xu have introduced an analytic approach to define tensor scale considering an image as a partitioning of the image space into multiple objects regions.

Let us consider an image in $\mathbb{R}^n$ | $\mathbb{R}$ is the set of real numbers, where multiple objects are defined as partitions by finitely many $(n-1)$-D manifolds, say, m_1, $m_2, \cdots, m_M$; referred to as *partitioning hyper-surfaces.* First, let us consider a point $p \in \mathbb{R}$ and a set of orthogonal vectors $\tau_1(p)$, $\tau_2(p) \cdots$, $\tau_i(p)$. An $(n-i)$-D image is formed over the orthogonal complement $W_i^\perp$ of the subspace W_i defined by $\tau_1(p)$, $\tau_2(p) \cdots$, $\tau_i(p)$ with p as the origin where partitioning hyper-surfaces are $(n-i-1)$-D manifolds $W_i^\perp \cap m_1$, $W_i^\perp \cap m_2 \cdots W_i^\perp \cap m_M$. Let us refer to this image as *orthogonal complement image* of $\tau_1(p)$, $\tau_2(p) \cdots$, $\tau_i(p)$ at p. *Tensor scale* $T(p)$ at a point $p \in \mathbb{R}^n$ is defined as an ordered sequence of orthogonal vectors $\tau_1(p)$, $\tau_2(p) \cdots$, $\tau_i(p)$ inductively defined as follows:

1. $\tau_1(p)$ is the vector from p to the nearest point on a partitioning hyper-surface.

2. Given the first i orthogonal vectors, $\tau_1(p)$, $\tau_2(p) \cdots$, $\tau_i(p)$, $\tau_{i+1}(p)$is defined as the vector from p to the nearest point on a partitioning hyper-surface in the

orthogonal complement image of $\tau_1(p)$, $\tau_2(p)$ $\cdots$, $\tau_i(p)$ at p.

$\tau_1(p)$ and $\tau_2(p)$ are referred to as primary and secondary tensor vectors of p; in 3D, $\tau_3(p)$ is referred to as the *tertiary tensor vector*. The notion of tensor scale defined as above is schematically described in Figure 4.1 using a 3D representation of rabbit femur bone surface m_1 segmented via μCT imaging; here, cancellous bone and marrow regions are filled in for illustration purpose. As illustrated in the figure, tensor scale $T(p)$ at a point p in a 3D image is an ordered sequence $\tau_1(p)$, $\tau_2(p)$, $\tau_3(p)$ of three orthogonal vectors. The first vector $\tau_1(p)$ (red) defines the direction and distance to the closest point on the femur surface. The orthogonal complement plane $W_1^{\perp}$ and the 1-D separating manifold $W_1^{\perp} \cap m_1$ on $W_1^{\perp}$ are shown in the figure; note that the 1-D separating manifold (cyan) is essentially the intersection between the plane $W_1^{\perp}$(blue) and the partitioning surface m_1 (the femur bone surface) in the 3D image. The secondary tensor vector $\tau_2(p)$ (yellow) is defined by the point on $W_1^{\perp} \cap m_1$ that is closest to p. Once $\tau_1(p)$ and $\tau_2(p)$ are found, the line (dotted green) on which the tertiary tensor vector $\tau_3(p)$ (green) lie is confirmed; the final direction and the length of $\tau_3(p)$ is defined by finding the closest point on the separating surface along the line.

4.3 Constrained Region Growing: Theory, Algorithms and an Application to Vessel Segmentation

Several segmentation approaches, including manual outlining [58], thresholding, boundary based [34, 63] graph-cut [10], region-based [159, 152], and shape and model-based [26, 24] techniques have been introduced and subsequently modified and
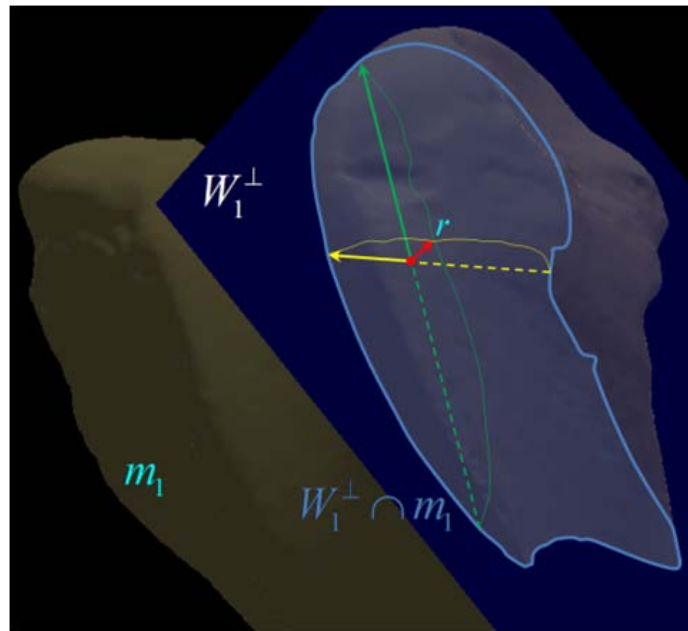
Figure 4.1: An illustration of tensor scale using a rabbit femur bone surface (dark off-white) forming a 2-D manifold m_1. The candidate point p is shown as a red dot; the point on m_1 closest to p gives the primary tensor vector $\tau_1(p)$ (red). The orthogonal complement plane $W_1^\perp$ and the 1-D manifold $W_1^\perp \cap m_1$ are shown in blue and cyan, respectively. Secondary tensor vector $\tau_2(p)$ is defined by the point on $W_1^\perp \cap m_1$ closest to p; finally, $\tau_3(p)$ is given by the closest point on $W_1^\perp \cap m_1$ along the line orthogonal to $\tau_2(p)$. It may be noted that projections of the two lines (dotted yellow and green) on m_1 along $\tau_1(p)$ provide principal directions of m_1 at r, the meeting location with $\tau_1(p)$; this idea is used in our computational solution in 3D.

Figure 4.2: A schematic representation of a vascular tree structure in 2D. Tensor scale at a point p is indicated by the ellipse in red. The proposed constrained region growing algorithm uses this knowledge to facilitate growth along the structure while restricting growth across the local structure to stop leaking.

investigated in different applications. In this research project, we develop a new region growing algorithm with target application to segmentation of pulmonary vasculature in non-contrast CT imaging for human subjects. For this application, we selected region growing approach due to the following reasons - (1) large variations in shape of pulmonary vasculature from one subject to another, (2) difficulty of generating pulmonary vascular shape model, (3) complexity in both geometry and topology of vascular tree, especially, in the presence of fusions among artery, vein, and airway. The first two reasons discourage selection of shape or model based approaches while the third one indicates difficulty of using a boundary based approach for pulmonary vascular segmentation. However, we have observed a major challenge in using a region growing approach for the current application. Often, a region growing approach starts with a set of seeds specified inside a target object and continues growing the object region under a predefined set of rules. Among other region growing approaches [15, 21], fuzzy connectivity [111, 160, 112, 127] has become quite popular method, where the region growing is governed by a predefined fuzzy affinity relation as described in Section 4.2. Effectiveness of fuzzy connectivity is highly dependent on the choice of the affinity relation. A major challenge with application of fuzzy connectivity in pulmonary vessel segmentation emerges from the fact that vessels, the target object in the current application, form a tree-like structure of tubular paths and at fine scales, the diameter of these paths may be comparable to voxel resolution. Therefore, these tubular paths, especially at finer scales, are vulnerable and getting broken by noise and other imaging artifacts and the continuity of vascular structure

may get lost using a region growing rules suitable for other regions. On the other hand, softening the rules to capture the broken continuity may cause to leaking at other regions. However, a human expert may capture the broken continuity implicitly using the contextual local structures. In our research, we develop a constrained region growing algorithm where the growing rules adapt to local structure geometry facilitating growth along a structure while constraining it across local structures. To solve this problem, we use tensor scale [117] that gives an ellipsoidal representation of the local structure at every image point as described in Section 4.2. For example, consider the example of Figure 4.2; using the tensor scale at the point p, we know the orientation and geometry of local structures at p. The proposed constrained region growing algorithm uses this knowledge to facilitate growth along the structure while restricting growth across the local structure to stop leaking. In the following paragraph, we formally describe the theory and algorithms.

As described in Section 2.2.1, the effectiveness of fuzzy connectivity largely depend on the choice of the affinity function $\mu_\kappa : \mathcal{Z}^3 \times \mathcal{Z}^3 \to [0,1]$. A detailed discussion of formulation of affinity function may be found in [117]. However, there is not mention on how to use structure anisotropy and orientation informally to locally adopt the affinity in a direction-dependent fashion. Here, we formulate a local tensor-scale definited affinity function to simulate a constrained region growing that facilitates the growth of an object along local structure direction while constraining it across local structure. Following the suggestion of [117], we use the basic underlying
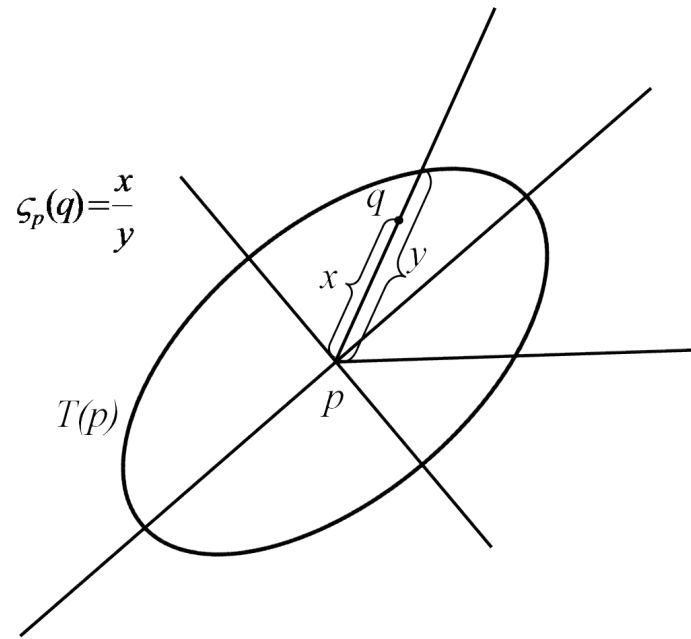
Figure 4.3: An illustration to explain the expression $\varsigma_p(q)$ used in Equation 4.4 .

formulation of the affinity function:

$$
\mu_\kappa(p, q) = \begin{cases} 1, & \text{if } p = q, \\ \mu_\alpha(p, q)\sqrt{\mu_\psi(p, q)\mu_\varphi(p, q)}, & \text{otherwise.} \end{cases} \tag{4.1}
$$

where $\mu_\alpha : \mathcal{Z}^3 \times \mathcal{Z}^3 \to 0, 1$ is the adjacency function while $\mu_\psi(p, q)$ captures homogeneity between p and q and $\mu_\varphi(p, q)$ gives the hanging-togetherness of p, and q in the target object based on likeliness of their feature values with respect to the expected feature distribution of the target object. It was also argued in [117] that the function $\mu_\psi(p, q)$ should be chosen to reflect the measure of the fuzzy proposition "x is small" [64] while the other function μ_φ should be chosen to reflect the measure of the fuzzy proposition "x is close to an expected value" [64]. In our research work we have used

the following functional forms for $\mu_\psi(p,q)$ and $\mu_\varphi(p,q)$ satisfying these properties:

$$\mu_\psi(p,q) = e^{-\frac{|f(p)-f(q)|^2}{2\sigma_\psi^2}}. \tag{4.2}$$

and

$$\mu_\varphi(p,q) = min(e^{-\frac{|f(p)-m|^2}{2\sigma_\varphi^2}}, e^{-\frac{|f(q)-m|^2}{2\sigma_\varphi^2}}). \tag{4.3}$$

where σ_ψ and σ_φ are two different standard deviation parameters used for homogeneity and object feature distribution and m is the mean object feature value. Although, this formulation immediately extends to vector-valued images, here, we consider only scalar-valued images depending on our application. The key idea of our constrained region growing is to locally adapt the two parameters σ_ψ and σ_φ a direction dependent manner using local tensor to enhance growth compliance with local structures.

As discussed in the previous paragraph, the control parameters σ_ψ and σ_φ determine the growth process for an object. When these parameters are large, the object grows more vigorously and possibilities of leaking through object boundaries increase. On the other hand, when small values are used for these parameters, the growth process works conservatively and the chance of breaking object continuity due to noise and other imaging artifacts increases. In the conventional region growing methods [15, 21], these parameters was kept fixed and fine control on and adaptivity to local structural properties were lacking. These regional control and adaptivity are provided by local scale. The motivation of using tensor scale in region growing is to introduce the local control and adaptivity in an orientation-dependent fashion as

illustrated in Figure 4.2. Specifically, the two controlling parameter σ_ψ and σ_φ are determined by local tensor scale in a space- and orientation-variant manner as follows:

$$\sigma_X(p,q) = \chi(max(\frac{|\vec{qp}|}{\varsigma_p(q)}, \frac{|\vec{pq}|}{\varsigma_q(p)}))\sigma_{X,global},\tag{4.4}$$

$$\varsigma_p(q) = \sqrt{\frac{(\vec{qp}\cdot\hat{\tau}_1(p))^2}{\tau_1(p)} + \frac{(\vec{qp}\cdot\hat{\tau}_2(p))^2}{\tau_2(p)}},\tag{4.5}$$

and $X \in \psi, \phi$ and χ is a monotonically non-decreasing function and $\sigma_{X,global}$ is the parameter determined in the same way as described in [129]. In this paper, the following functional form is used for χ

$$\chi(x) = \begin{cases} 1, & \text{if } x > x_{max} \\ \frac{1+x}{1+x_{max}}, & \text{otherwise.} \end{cases}\tag{4.6}$$

The value of x_{max} will be determined experimentally. As illustrated in Figure 4.3, $\varsigma_p(q)$ gives the ratio of the distance "x" to the distance "y" so that $|\vec{qp}|/\varsigma_p(q)$ (see Equation 4.4) yields the length of the tensor scale $T(p)$ along $\vec{qp}$ ("y" in Figure 4.3). To finish with the explanation of Equation 4.4, $\hat{\tau}_1(p)$ and $\hat{\tau}_2(p)$ are the unit vectors along $\tau_1(p)$ and $\tau_2(p)$, respectively; recall that $\tau_1(p)$ and $\tau_2(p)$ are the two semi-axes of $T(p)$.

4.4 Experimental Methods and Results

The method has been applied on several non-contrast pulmonary human CT imaging. Results of application of the method on two human data are presented in Figures 4.4 and 4.5 and compared with that of Shikata *et al*'s [141] method. For our

method, we selected only one seed point in the cardiac region and allowed to grow under constrained region growing. The fuzzy connectivity image computed based on tensor scale information is shown in Figure 4.4(b). Result of application of the method of constrained region growing for vessel segmentation is shown in Figure 4.4(c). It may be noted that the method successfully captured results of at different scales including those at very high and small scales. However, the method grows into the tissue regions in the body. Pulmonary vessel was separated from cardiac and other tissue regions by putting a separator on pulmonary trunk. Result of pulmonary vasculature after removing the heart and other body regions is shown in Figure 4.4(d). For comparison, a matching slice form Shikata *et al*'s algorithm is shown in Figure 4.4(e). Although, the method by Shikata *et al* was able to capture thin vessels, it somewhat compromised with vascular geometry specially for large scale vessels. Three-dimensional rendition of vasculature using our method and Shikata *et al*'s method are presented in Figure 4.4(f, g) respectively. Three-dimensional rendition confirmed our observations in two dimension. In Figure 4.5, pulmonary vessel segmentation on another data set is shown. From the results shown in Figures 4.4 and 4.5, we can see that vessel segmentation results using constrained region growing algorithm capture not only more details at large and small scales but also maintain better topological information around the heart region.

To quantitatively evaluated the performance of our method, we compute true positive and false negative measures for our method on two non-contrast pulmonary CT data sets of human subject. For this purpose, we selected about 1000 points inside
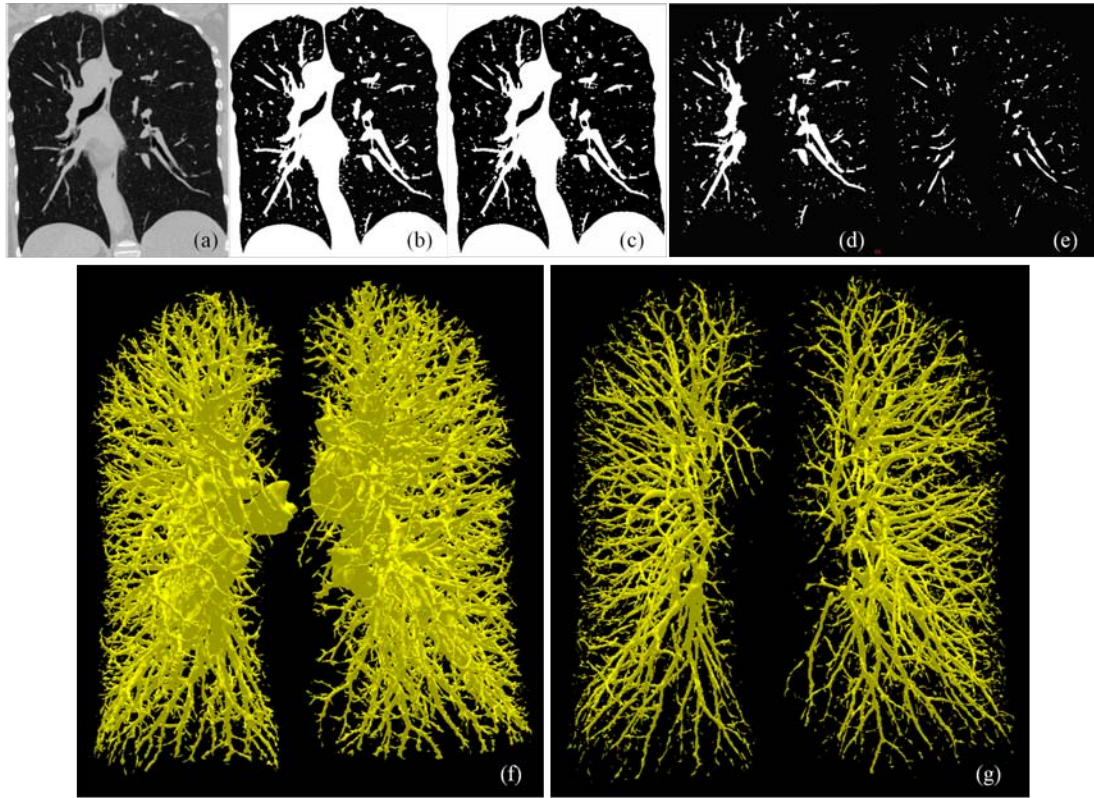
Figure 4.4: Results of application of the constrained region growing algorithm to a human *in vivo* pulmonary CT image. (a) Coronal image slice from a thoracic CT image of a human subject. (b) Fuzzy connectivity image computed using tensor scale information. (c) Vessel segmentation from fuzzy connectivity image. (d) Segmented vessel image after removing heart and other body region. (e) 3D rendition of segmented vessel tree using tensor scale based algorithm. (f) 3D rendition of segmented vessel using Shikata *et al*'s method
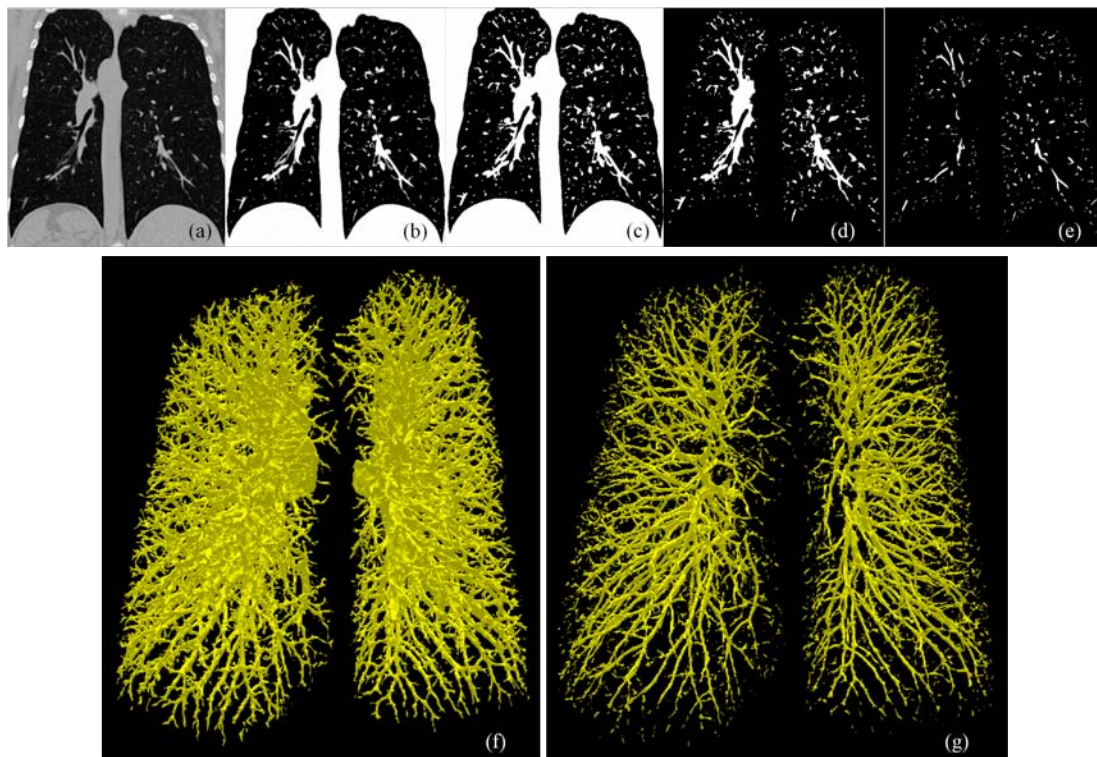
Figure 4.5: Same as Figure 4.4, but for another data set.

vascular region on randomly selected slices. Also, we selected another set of about 1000 ponts outside the vascular region. Let V denotes the set of points manually selected on vascular region and let B denotes the set of points manually selected outside the vascular region. Let V_C and B_C denote the set of points on vascular region and its complement derived using the constrained region growing algorithm. Following the observation that $V_C \gg V$ and $B_C \gg B$, we defined the following measures to examine the performance of the constrained region growing algorithm.

$$True \ \ Positive = \frac{|V \cap V_C|}{|V|}. \tag{4.7}$$

$$True \ \ Negative = \frac{|B \cap B_C|}{|B|}. \tag{4.8}$$

$$False \ \ Positive = \frac{|B \cap V_C|}{|B|}. \tag{4.9}$$

$$False \ \ Negative = \frac{|V \cap B_C|}{|V|}. \tag{4.10}$$

$$Accuracy = \frac{|V \cap V_C| + |B \cap B_C|}{|V| + |B|}. \tag{4.11}$$

$$Error = \frac{|V \cap B_C| + |B \cap V_C|}{|V| + |B|}. \tag{4.12}$$

Results of quantitative analysis are shown in Table 4.1. The accuracy is quite high for both data sets. The *True Positive* and *True Negative* here are defined as the accuracy for detection of vascular region and background, which turn to be values close to 1. The *False Positive* is the percent of voxels outside vascular region are falsely detected vessel, which is a small value for both data sets. The *False Negative* is the percent of voxels inside vascular region are falsely detected as non-vessel, which is a small value for both data sets. The close to 1 value for *Accuracy* and small value for *Error* shows that the constrained region growing algorithm produce high accuracy for pulmonary vessel segmentation, which small error.

Table 4.1: Quantitative result of vasculature segment on non-contrast *in vivo* CT image of human subjects

	Data set 1	Data set 2
True Positive	0.9790	0.9726
True Negative	0.9729	0.9640
False Positive	0.0271	0.0359
False Negative	0.0210	0.0274
Accuracy	0.9761	0.9688
Error	0.0239	0.0313

CHAPTER 5
APPLICATION TO ACINAR SEGMENTATION IN HIGH RESOLUTION MICRO-CT IMAGES

In this chapter we briefly describe an application of our multi-scale topo-morphometric opening algorithm to assess acinar morphology using optically magnified micro-CT imaging [164, 40]. This research is primarily being conducted by Mr. D. M. Vasilescu in Professor E. A. Hoffman's laboratory. My contribution to this study is to help Mr. Vasilescu to design the image processing cascade. Overall aim of this study is to establish a database containing the normal characteristics of the murine lung based on nondestructive imaging via micro-CT. Recent techniques for high resolution micro-CT imaging (MicroXCT, XRadia, Concorde, CA) allows non-destructive imaging of murine lung, which is fixed in-situ via a modified Heitzman's solution and air dried, at resolutions upto 1μm/voxel. Localized imaging within the whole lung includes a volume of $8mm^3$. Such a volume contains multiple acini and small airways and vessels. Pulmonary acinus segmentation opens an avenue for morphometric analyses of alveoli which will be effective for characterizing the murine lung at the alveolar level. In the following sections, I describe the image processing steps involved in this study and describe our results.

5.1 Multi-Scale Topo-Morphologic Opening Method for Segmenting the Pulmonary Acinus

Simple segmentation algorithms such as thresholding, filtering, and region growing, fail to produce acceptable results for acinus segmentation. Primary causes behind the failure are presence of granular noise, noisy leakages through airways and alveolar walls as well as complex three-dimensional geometry and spatial coupling among different acini. Here, we present a computerized semi-automatic method for segmenting an acinus in high resolution micro-CT images. The method is accomplished in the following steps. First, the image is filtered using an anisotropic diffusive filtering algorithm to reduce effects of noise which is followed by thresholding for airspaces and filling noisy topological cavities caused by residual noise after filtering. The resulting image provides a noise-free segmentation of airspace within the image. However, a simple region growing approach fails to extract a single acinus as multiple acini get connected through noisy leakages in airway and alveolar walls. This was solved using two sets of seeds - one, in the target acinus and the other in surrounding airspace, via a graphical user interface (GUI) system developed in our laboratory. The method works using the theory of iterative multi-scale topo-morphologic opening, recently developed in our lab, which iteratively eliminates leakages at different scales starting at larger scales and progressing toward smaller scales while maintaining spatial connectivity and identity of individual structures.

Overall task flow of the segmentation algorithm is presented in Figure 5.1. After selecting a ROI in a micro-CT image of a murine lung specimen, first, the effect
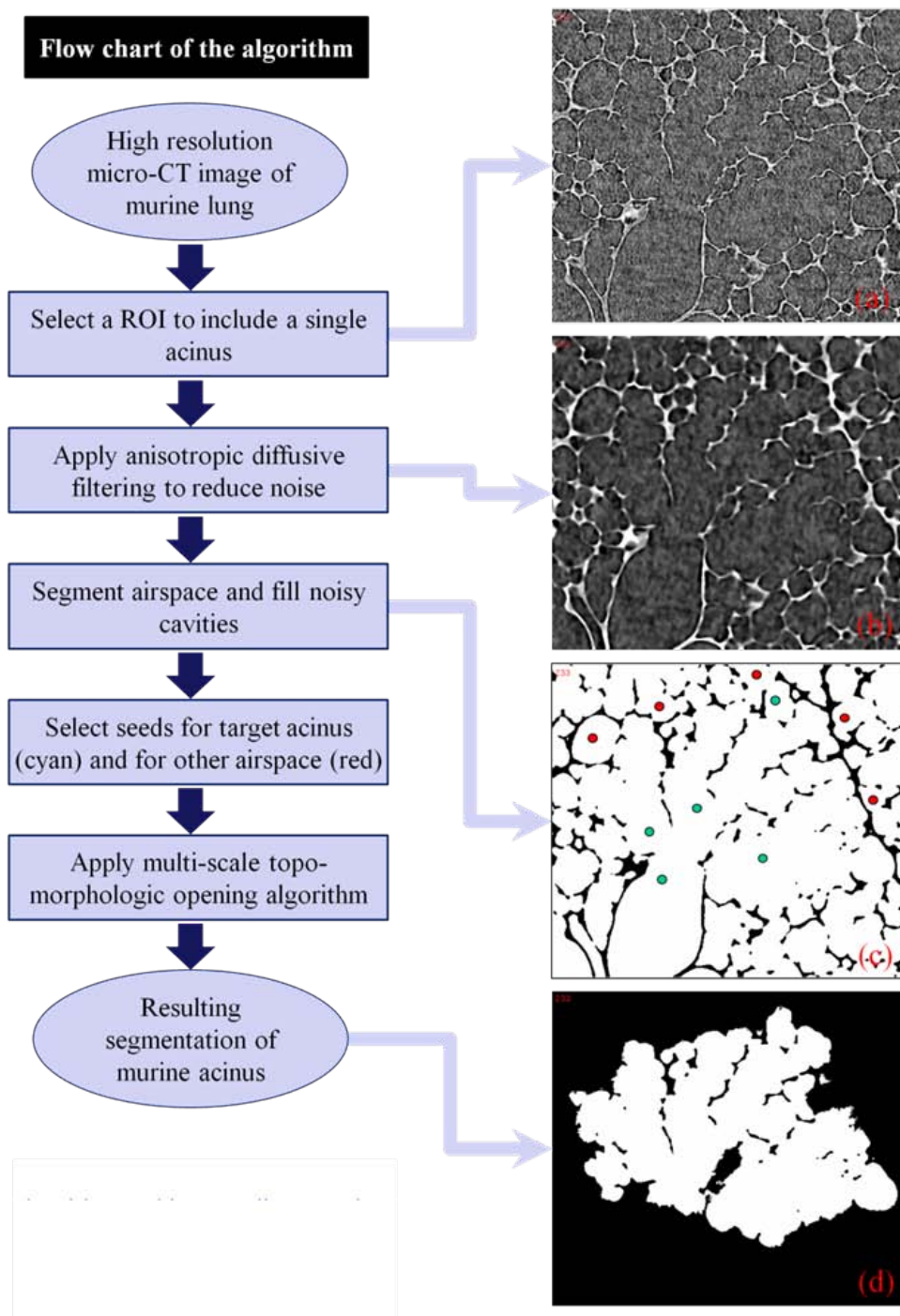
Figure 5.1: Sequential steps of the algorithm and intermediate results during segmentation of pulmonary acinus in high resolution micro-CT imaging.

of noise is reduced using anisotropic diffusive filtering [102] that preserves most edges (Figure 5.1(b)). Then air-space is segmented from filtered image using thresholding and noisy cavity filling. Segmented air-space gets connected in 3D through noisy leaks at various scales. A single acinus volume is isolated from fused 3D air-space using a multi-scale topo-morphologic opening algorithm described in Chapter 2. The method is initialized with two sets of seeds, one for the target acinus and the other for surrounding air-space (Figure 5.1(c)). The algorithm morphologically separates two mutually fused structures starting at large scales and iteratively progressing toward finer scales. The algorithm produces an isolated acinar volume at convergence.

5.2   Results of Acinar Segmentation and Discussion

The method has been successfully applied on micro-CT images of 6 murine lung specimens. Results of computerized segmentation of an acinus in a micro-CT image is illustrated in Figure 5.2. Also, a quantitative evaluation was performed on two data sets. Manual outlining of acinus region was performed on micro-CT images using a manual outlining tool on a two-dimensional graphical interface. True positive and false negative measures were computed using manual outlining (M) and computerized segmentation (S) described in the previous section. The true positive and the false negative measure were defined as follows:

$$True\ Positive\ =\ \frac{M \cap S}{M \cup S}.$$
(5.1)
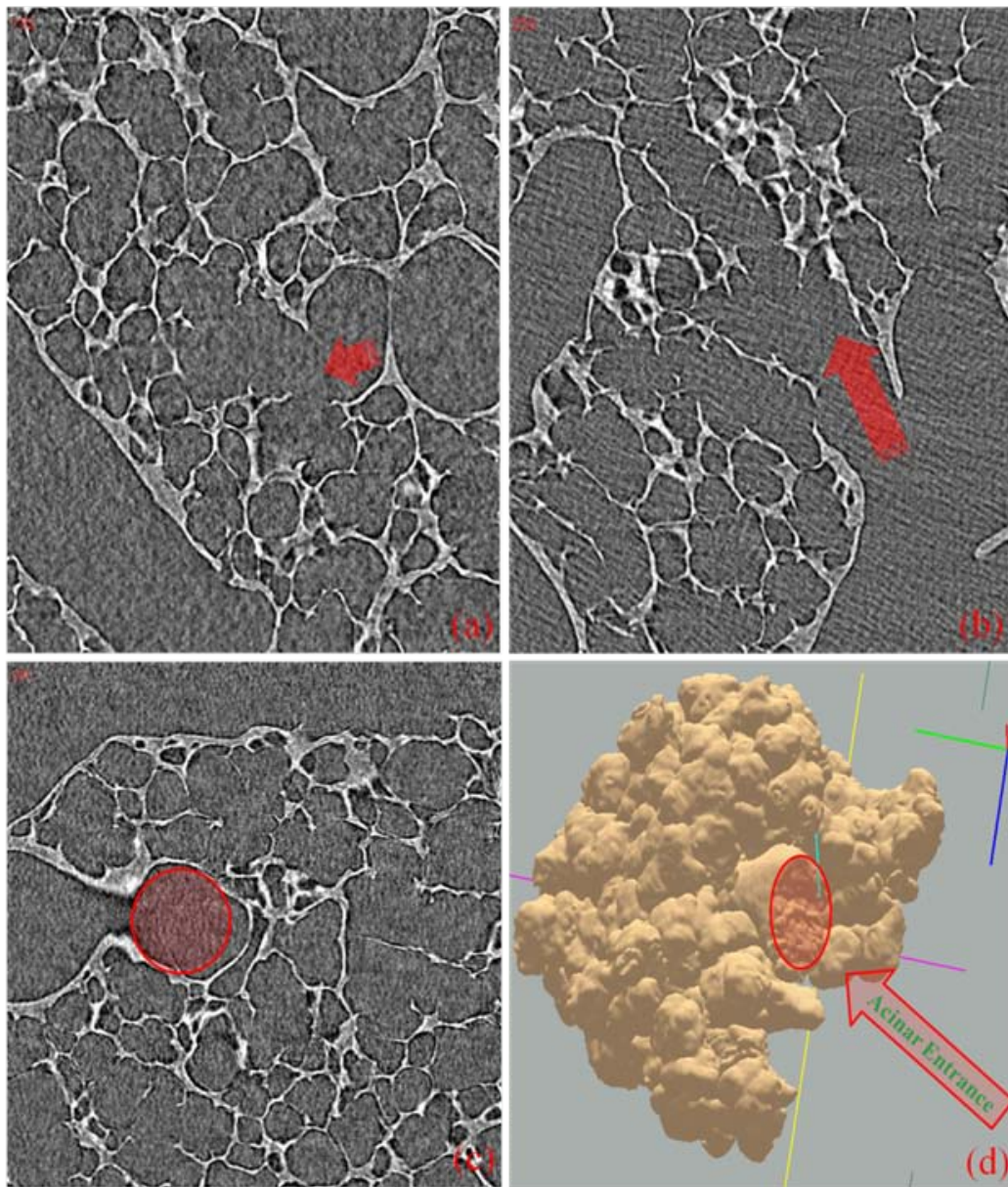
Figure 5.2: Results of computerized segmentation of an acinus in a micro-CT image. (a-c) Coronal, transverse, and saggital slices from a micro-CT image of a murine lung specimen. 3D rendition of an isolated single acinus. The entrance to the acinus is marked with red arrows and circles.

$$False\ Negative\ =\ \frac{(M \cup S) - (M \cap S)}{M \cup S}. \tag{5.2}$$
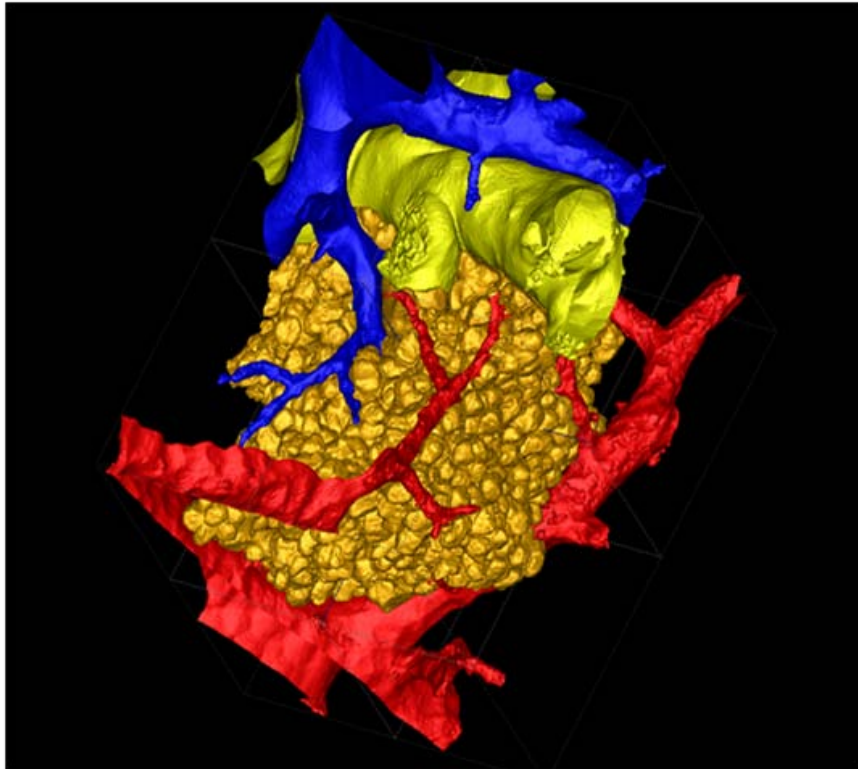
Figure 5.3: Additional segmentation of transitional bronchiole and vasculature in an acinus with multi-scale topo-morphologic opening algorithm. Courtesy of Mr. Vasilescu and Prof. Hoffman.

Results of quantitative analysis is shown in Table 5.1. Mr. Vasilescu applied the same method to further segment terminal arteries and veins fused with the acinus structure (see Figure 5.3).

Overall, a new method has been developed to segment individual acini via high resolution micro-CT imaging. The method is suitable for routine segmentation

of acinar structures The segmented acinus can be used for murine acinar morphometry

[164].

Table 5.1: Results of quantitative accuracy analysis of the new acinus segmentation algorithm on micro-CT images of two murine lung specimens.

	True Postive	False Negative
data set 1	95.1%	4.9%
data set 2	96.0%	4.0%

Note: Here the ground truth was determined using a manual outlining technique.

CHAPTER 6
CONCLUSIONS AND FUTURE WORKS

6.1   Concluding Remarks

The overall aim of my PhD research project was to design, develop and evaluate a new practical environment to generate isolated representation of arterial and venous trees in non-contrast pulmonary CT imaging of human subjects and to extract quantitative measures at different tree levels. This overall aim was structured in six specific aims. In the following, I describe my accomplishments and challenges faced under each of these six chapter.

Aim 1 and 2: The first aim was to design and develop a new method to separate artery/vein trees in non-contrast pulmonary CT imaging of human subjects. The second aim was dedicated to evaluate the accuracy, reproducibility and efficiency of the method. We have developed a novel theory and algorithm for multi-scale topo-morphologic opening algorithm to separate two similar-intensity objects mutually fused at different scales and spacial locations with unknown geometry of fusions. The method has answered to several fundamental questions including — (1) how to determine optimal local scale to separate two fused structures, (2) how to account for scale variations of both structures and fusions and (3) how to build connectivity of locally separated structures at various scales. The accuracy of the method has been examined on computer generated phantoms as well as on CT imaging of a vessel cast of a pig's lung with different contrast for arterial/venous trees. The reproducibility

of the method has been studied *in vivo* pulmonary images of a pig at three different lung volumes and multi-level artery/vein separations of non-contrast pulmonary CT imaging of human subjects. The efficiency of the method has been studied in terms of number of seed required to achieve a certain level of accuracy . The original theory, algorithm and evaluation results have been published in a journal paper [123] and in several conference proceeding papers. We have developed an integrated 2D and 3D graphical interface with local update at interactive speed. Currently, we are preparing a journal paper (IEEE Transaction on Biomedical Engineering) reporting new improvements with method and results of a comprehensive evaluation experiments. Major challenges with A/V separation are how to find the scale of local morphological operators and how to trace continuity of locally separated regions. These challenges have been successfully addressed in our method by incorporate the morphological FDT feature with topological fuzzy connectivity along with a morphological reconstruction algorithm.

Aim 3 and 4: the third aim was dedicated to develop a multi-level volumetric tree representation of isolated arterial/venous tree and to extract vascular measurements at different tree levels. The fourth aim was targeted at evaluation of the method. We have developed an arc-skeleton based volumetric tree generation algorithm. We recognized several challenges during our method design and developments, including (1) topological aberrations in digital space, (2) presence of noisy branches and junctions, (3) non-optimal path joining to junction nodes or between junction node and end node. We have meet these challenges using digital topological

and tree geometric analysis. We have developed a shortest path computation function that joins two voxels in a volumetric tree structure that passes centrally along the tree. A volumetric multi-level tree representation has been achieved using a new feature propagation algorithm recently developed in our laboratory. The method has been appiled on several computer generated phantoms and CT images of pulmonary vessel cast and *in vivo* pulmonary CT images of a pig at different airway pressure. Experimental results have shown that the method is accurate and reproducible . The method also been applied on pulmonary CT images of human subject. However, the artifact distortions of vascular morphology, especially, at large scale have reduced meaningfulness of tree levels at large scales.

Aim 5 and 6: The objective of these two aims to develop a new pulmonary vessel segmentation algorithm (aim 5) and to evaluate it accuracy in *in vivo*non-contrast pulmonary CT images of human subjects (aim 6). We have developed a new theory and algorithms for a anisotropic constrained region growing that encourages axial region growing while arresting cross-structure leaking. The method is based on a local anisotropic parameter control based on tensor scale. The method has been successfully applied on several non-contrast pulmonary CT images of human subjects. The accuracy of the new method has been evaluated using manually selection of vascular and non-vascular voxels and the results found are very promising.

Beside completion of the above six aims, I have also presented an application of our algorithm for acinus segmentation in high resolution micro-CT images of murine lung specimen (this study is primarily carried out by Mr. Vasilescu in Professor

Hoffman's laboratory).

6.2 Future Works

Future works related to my PhD thesis may be grouped into two major categories — (1) improvements of algorithms and methods and (2) new research direction. Research plans of my future works under the first category are as follows:

1. Incorporate tensor scale or other advanced tubular features to improve performance of A/V separation.

2. Improve multi-level volumetric tree generation algorithm by improving

   - Detection of noisy branches.

   - Optimization of junction nodes location.

   My future works under new direction are as follows:

1. Develop a tree matching algorithm to build correspondence between intra- and inter-subject pulmonary A/V trees.

2. Develop method to active statistical tree model of pulmonary A/V trees and detect major common branches.

REFERENCES

[1] J. M. Abrahams, P. K. Saha, R. W. Hurst, P. D. LeRous, and J. K. Udupa. Three dimensional bone-free rendering of the crebral circulation using computed tomographic angiography and fuzzy connectedness. *Neurosurgery*, 51:264–269, 2002.

[2] T. Alderliesten, W. Niessen, K. Vincken, J. Maintz, F. Janson, O. van Nieuwen-huizen, and M. Viewgever. Objective and reproducible segmentation and quan-tification of tuberous sclerosis lesions in FLAIR brain MR images. In *SPIE: Medical Imaging*, San Diego, CA, 2001.

[3] J. Babaud, A. P. Witkin, M. Baudin, and R. O. Duda. Uniqueness of the gaussian kernel for scale-space filtering. *IEEE Transactions on Pattern Analysis and Machine Intelligence*, 8:25–33, 1986.

[4] A. L. D. Beckers and A. W. M. Smeulders. Optimization of length measure-ments for isotropic distance transformations in three dimension. *CVGIP: Image Understanding*, 55:296–306, 1991.

[5] James C. Bezdek and Sankar K. Pal, editors. *Fuzzy Models for Pattern Recog-nition: Methods That Search for Structures in Data*. IEEE, New York, NY, 1992.

[6] S. Bodas and J. Reinhardt. Improved association graph matching of intra-patient airway trees. Master thesis, The The University of Iowa, 2010.

[7] G. Borgefors. Distance transform in arbitrary dimensions. *Computer Vision Graphics Image Processing*, 27:321–345, 1984.

[8] G. Borgefors. Distance transformations in digital images. *Computer Vision Graphics Image Processing*, 34:344–371, 1986.

[9] G. Borgefors. On digital distance transformation in three dimensions. *Computer Vision Graphics Image Processing*, 64:368–376, 1996.

[10] Y. Boykov and G. Funka-Lea. Graph-cuts and efficient N-D image segmentation. *Interantion Journal of Computer Vision*, 70:109–131, 2006.

[11] R. N. Bracewell, editor. *Two-Dimensional imaging*. Prentice-Hall, Inc, Engle-wood Cliffs, New Jersey, 1995.

[12] J.J. Buckley and E. Eslami. Fuzzy plane geometry I: Points and lines. *Fuzzy Sets and Systems*, 86:179–187, 1997.

[13] B. M. Carvalho, C. J. Gau, G. T. Herman, and T. Y. Kong. Algorithms for fuzzy segmentation. *Pattern Analysis and Applications*, 2:73–81, 1999.

[14] J. E. Cates, R. T. Whitaker, and G. M. Jones. Case study: an evaluation of user-assisted hierarchical watershed segmentation. *Med Image Anal*, 9:566–578, 2004.

[15] Y. L. Chang and X. Li. Adaptive image region growing. *IEEE Transactions on Image Processing*, 3:868–873, 1994.

[16] A. Charnoz, V. Agnus, G. Malandain, M. Tajine S. Nicolau, and L. Soler. Design of robust vascular tree matching: Validation on liver. *Information Processing in Medical Imaging*, pages 443–455, 2005.

[17] A. Charnoz, V. Agnus, G. Malandain, L. Soler, and M. Tajine. Tree matching applied to vascular system. *Graph-Based Representations in Pattern Recognition*, pages 183–196, 2005.

[18] V. Chatzis and I. Pitas. A generalized fuzzy mathematical morphology and its application in robust 2-D and 3-D object representation. *IEEE Trans Image Process*, 9:1798–1810, 2000.

[19] M.H. Chen and P.F. Yan. A multiscaling approach based on morphological filtering. *IEEE Trans. Pattern Analysis and Machine Intelligence*, 11:694–700, 1989.

[20] S. Chen and R. M. Haralick. Recursive erosion, dilation, opening, and closing transforms. *IEEE Trans Image Process*, 4:335–345, 1995.

[21] S. Chu and A. Yuille. Region competition: unifying snakes, region growing and bayes/MDL for multiband image segmentation. *IEEE Transactions on Pattern Analysis and Machine Intelligence*, 3:884–900, 1996.

[22] K. C. Ciesielski, J. K. Udupa, P. K. Saha, and Y. Zhuge. Iterative relative fuzzy connectedness for multiple objects with multiple seeds. *Computer Vision and Image Understanding*, 107:160–182, 2007.

[23] C. Ciofolo and C. Barillot. Atlas-based segmentation of 3D cerebral structures with competitive level sets and fuzzy control. *Med Image Anal*, 13:456–470, 2009.

[24] T. F. Cootes, G. J. Edwards, and C. J. Taylor. Active appearance models. In *the European Conference on Computer Vision*, 1998.

[25] T. F. Cootes, G. J. Edwards, and C. J. Taylor. Active appearance models. *IEEE Transactions on Pattern Analysis and Machine Intelligence*, 23:681–685, 2001.

[26] T. F. Cootes, C. J. Taylor, D. Cooper, and J Graham. Active shape models - their training and application. *Computer Vision and Image Understanding*, 61:38–59, 1995.

[27] A. Daneshgar. Residuated semigroups and morphological aspects of translation invariant systems. *IEEE Trans. Fuzzy Syst*, 90:69–81, 1997.

[28] P. E. Daniensson. Euclidean distance mapping. *Computer Vision Graphics Image Processing*, 14:227–248, 1980.

[29] A. Darabi. Assessment of the porous media structure based on fuzzy distance transform and its map ridge. *Magnetic Resonance Imaging*, 25:556–556, 2007.

[30] M. de Bruijne and M. Nielsen. Multi-object segmentation using shape particles. *Inf Process Med Imaging*, 19:762–773, 2005.

[31] S. Dellepiane and F. Fontana. Extraction of intensity connectedness for image processing. *Pattern Recognition Letters*, 16:313–324, 1995.

[32] S. Dellepiane, F. Fontana, and G. L. Vernazza. Nonlinear image labeling for multivalued segmentation. *IEEE Trans. Image Processing*, 5:429–446, 1996.

[33] J. H. Elder and S. W. Zucker. Local scale control for edge detection and blur estimation. *IEEE Transactions on Pattern Analysis and Machine Intelligence*, 20:699–716, 1998.

[34] A.X. Falcão, J. K. Udupa, S. Samarasekera, and S. Sharma. User-steered image segmentation paradigms: live wire and live lane. *Graphical Models and Image Processing*, 60:233–260, 1998.

[35] M. Ferrant, O. Cuisenaire, and B. Macq. Multi-object segmentation of brain structures in 3D MRI using a computerized atlas. In *SPIE: Medical Imaging*, San Diego, CA, 1999.

[36] M. Ferraro, G. Bocclgnone, and T. Caell. On the representation of image structures via scale space entropy conditions. *IEEE Transactions on Pattern Analysis and Machine Intelligence*, 21:1190–1203, 1999.

[37] J. Fleureau, M. Garreau, D. Boulmier, and A. Hernandez. 3D multi-object segmentation of cardiac MSCT imaging by using a multi-agent approach. In *IEEE Eng Med Biol Soc*, 2007.

[38] D. Freedman, R. J. Radke, T. Zhang, Y. Jeong, and G.T.Y Chen. Model-based multi-object segmentation via distribution matching. In *IEEE Workshop on Articulated and Nonrigid Motion (in conjunction with IEEE CVPR)*, 2004.

[39] P. D. Gader. Fuzzy spatial relations based on fuzzy morphology. In *the 6th IEEE Int. Conf. Fuzzy Systems*, Barcelona, Spain, 1997.

[40] Z. Gao, D. M. Vasilescu, E. A. Hoffman, and P. K. Saha. A multi-scale topo-morphologic opening approach for segmenting the pulmonary acinus in high resolution micro-ct images of fixed murine lungs. In *American Journal of Respiratory and Critical Care Medicine*.

[41] Y. Ge, R. Grossman, J. K. Udupa, L.Wei, L. Mannon, M. Polansky, and D. L. Kolson. Brain atropy in relapsing-remitting multiple sclerosis and secondary progressive multiple sclerosis: longitudinal quantitative analysis. *Radiology*, 214:665–670, 2000.

[42] R. C. Gonzalez and R. E. Woods, editors. *Digital Image Processing*. Addison-Wesley, Reading, M, 1992.

[43] M. W. Graham. Optimal graph-theoretic approach to 3-D anatomical tree matching. In *3rd IEEE International Symposium on Biomedical Imaging: Nano to Macro*, pages 109–112, 2006.

[44] M. W. Graham and W. E. Higgins. Globally optimal model-based matching of anatomical trees. In *Medical Imaging 2006: Image Processing*, volume 6144, page 614415, 2006.

[45] G. J. Grevera. The dead reckoning signed distance transform. *Computer Vision Image Understanding*, 95:317–333, 2004.

[46] S. Grossert, M. Koppen, and B. Nickolay. A new approach to fuzzy morphology based on fuzzy integral and its application in image processing. In *the Int. Conf. Pattern Recognition*, Vienna, Austria, 1996.

[47] R. M. Haralick and P. L. Katz. Model-based morphology: The opening spectrum. *Graphical Models and Image Processing*, 57:1–12, 1995.

[48] R. M. Haralick, S. R. Sternberg, and X. Zhuang. Image analysis using mathematical morphology. *IEEE Transactions on Pattern Analysis and Machine Intelligence*, 9:532–550, 1987.

[49] R.M. Haralick, X. Zhuang, C. Lin, and J.S.J. Lee. The digital morphological sampling theorem. *IEEE Trans. Acoustic, Speech, and Signal Processing*, 37:2067–2090, 1989.

[50] R. He and P. A. Narayana. Automatic delineation of Gd enhancements on magnetic resonance images in multiple sclerosis. *Medical Physics*, 29:1536–1546, 2002.

[51] G. T. Herman and B. M. Carvalho. Multiseeded segmentation using fuzzy connectedness. *IEEE Transactions on Pattern Analysis and Machine Intelligence*, 23:460–474, 2001.

[52] E. A. Hoffman, J. M. Reinhardt, M. Sonka, B. A. Simon, J. Guo, O. Saba, D. Chon, S. Samrah, H. Shikata, J. Tschirren, K. Palagyi, K. C. Beck, and G. McLennan. Characterization of the interstitial lung diseases via density-based and texture-based analysis of computed tomography images of lung structure and function. *Acad Radiol*, 10:1104–1118, 2003.

[53] C. Holtze, S. Alford, W. Lynch, E. V. Beek, M. Sonka, and E. Hoffman. The human lung atlas project: characterizing the pulmonary vascular tree. In *Engineering Open house Poster of the University of Iowa*, Iowa City, IA, 2007.

[54] P.T. Jackway. Morphological scale-space. In *the 11 th IAPX, Int'l Conf, Pattern Recognition*, 1992.

[55] A. K. Jain, editor. *Fundamentals of Digital Image Processing*. Prentice Hall, Upper Saddle River, NJ, 1989.

[56] B. K. Jang and R. T. Chin. Morphological scale space for 2D shape smoothing. *Computer Vision and Image Understanding*, 70:121–141, 1998.

[57] Y. Jin, A. F. Laine, and C. Imielinska. Adaptive speed term based on homogeneity for level-set segmentation. In *SPIE: Medical Imaging*, pages 383–390, San Diego, CA, 2002.

[58] C. Johnson, R. MacLeod, and J. Schmidt. Software tools for modeling, computation, and visualization in medicine. *Comp Med*, 94, 1995.

[59] D. Kainmueller, H. Lamecker, S. Zachow, and H.-C. Hege. Coupling deformable models for multi object segmentation. In Lecture Notes in Computer Science, editor, *International Symposium on Biomedical Simulation*, 2008.

[60] D. Kainmueller, H. Lamecker, S. Zachow, and H.-C. Hege. An articulated statistical shape model for accurate hip joint segmentation. In *IEEE Eng Med Biol Soc*, volume 2009, pages 6345–6351, 2009.

[61] D. Kainmueller, H. Lamecker, S. Zachow, M. Heller, and H.-C. Hege. Multi-object segmentation with coupled deformable models. *Medical Image Understanding and Analysis*, 2008.

[62] A. Kamiya and T. Togawa. Optimal branching structure of the vascular tree. *Bulletin of Mathematical Biology*, 34(4):431–438, 1972.

[63] M. Kass, A. Witkin, and D. Terzopoulos. Snakes: active contour models. *International Journal of Computer Vision*, 1:321–331, 1988.

[64] A. Kaufmann, editor. *Introduction to the Theory of Fuzzy Subsets*. Academic Press, New York, 1975.

[65] R. Klette and A. Rosenfeld, editors. *Digital Geometry: Geometric Methods for Digital Picture Analysis*. Morgan Kaufmann, San Francisco, CA, 2004.

[66] H. Kobatake. Future CAD in multi-dimensional medical images–project on multi-organ, multi-disease CAD system. *Comput Med Imaging Graph*, 31:258–266, 2007.

[67] J. J. Koenderink. The structure of images. *Biological Cybernatics*, 50:363–370, 1984.

[68] T. Y. Kong and A. Rosenfeld. Digital topology: introduction a survey. *Computer Vision, Graphics, and Image Processing*, 48:357–393, 1989.

[69] L. Koskinen, J. Astola, and Y. Neuvo. Soft morphological filters. In *the SPIE Symp. Image Algebra Morphological Image Processing*, 1991.

[70] L. Koskinen, J. Astola, and Y. Neuvo. Statistical properties of soft morphological filters. In *the SPIE Symp. Image Algebra Morphological Image Processing*, 1992.

[71] A. Kumar, W. Bilker, Z. Jin, and J. K. Udupa. Atropy and high intensity lesions: complementary neurobiological mechanisms in late-life major depression. *Neuropsychopharmacology*, 22:264–274, 2000.

[72] A. Kumar, W. Bilker, Z. Jin, J. K. Udupa, and G. Gottlieb. Age of onset of depression and quantitative neuroanatomic measures: absence of specific correlations. *Psych. Res. Neuroimag.*, 91:101–110, 1999.

[73] T. Lei, J. K. Udupa, P. K. Saha, and D. Odhner. Artery-vein separation via MRA - an image processing approach. *IEEE Transactions on Medical Imaging*, 20:689–703, 2001.

[74] Y. Leung, J. S. Zhang, and Z. B. Xu. Clustering by scale space filtering. *IEEE Transactions on Pattern Analysis and Machine Intelligence*, 22:1396–1410, 2000.

[75] P. Liang and Y. F. Wang. Local scale controlled anisotropic diffusion with local noise estimate for image smoothing and edge detection. In *the International Conference in Computer Vision*, Bombay, India, 1998.

[76] R. Lin and E. K. Wong. Logic gate implementation for gray-scale morphology. *IEEE Trans Image Process*, 13:481–487, 1992.

[77] T. Lindeberg. Scale-space for discrete signals. *IEEE Transactions on Pattern Recognition and Machine Intelligence*, 12:234–254, 1990.

[78] Y. Liu and Y. Liu. An algorithm of image segmentation based on fuzzy mathematical morphology. In *the International Forum on Information Technology and Applications*, pages 1264–1273, 2009.

[79] T. Lohe, T. Krger, S. Zidowitz, H. Peitgen, and X. Jiang. Hierarchical matching of anatomical trees for medical image registration. *Medical Biometrics*, 2:224–231.

[80] B. C. Lovell and A. P. Bradley. The multiscale classifier. *IEEE Transactions on Pattern Analysis and Machine Intelligence*, 18:124–137, 1996.

[81] P. A. Maragos and R. W. Schafer. Morphological skeleton representation and coding of binary images. *IEEE Trans. Acoust., Speech, Signal Processing*, 34:228–244, 1986.

[82] D. Marr. Vision. In W. H. Freeman and Company, editors, *IEEE Workshop on Mathematical Methods in Biomedical Image Analysis*, San Francisco, CA, 1982.

[83] M. P. Martínez-Pénez, J. Jiménez, and J. L. Navalón.

[84] M. E. Martinez-Perez, A. D. Hughes, A. V. Stanton, S. A. Thom, N. Chapman, A. A. Bharath, and K. H. Parker. Geometric tree matching with applications to 3-D lung structures. *IEEE Transactions on Biomedical Engineering*, 49(8):912–917, 2002.

[85] G. Matheron, editor. *Elements Pour une Tiorre des Mulieux Poreux*. Masson, Paris, 1965.

[86] G. Matheron, editor. *Random Sets and Integral Geometry*. Wiley, New York, 1975.

[87] D. L. McCubbery and R. M. Lougheed. Morphological image analysis using a raster pipeline processor. In *the IEEE Cornput. Soc. Workshop Computer Architecture .for Pattern Analysis and Image Database Management*, Miami Beach, FL, 1985.

[88] J. Metzen, T. Krger, A. Schenk, S. Zidowitz, H. Peitgen, and X. Jiang. Matching of tree structures for registration of medical images. *Graph-Based Representations in Pattern Recognition*, pages 13–24, 2007.

[89] Y. Miki, R. I. Grossman, J. K. Udupa, M. A. vanBuchem, M. D. Philips L. Wei, U. Patel, J. C. McGown, and D. L. Kolson. Differences between relapsing remitting and chronic progressive multiple sclerosis as determined with quantitative MR imaging. *Radiology*, 210:769–774, 1999.

[90] Y. Miki, R. I. Grossman, J. K. Udupa, L. Wei, M. Polansky, L. Mannon, and D. L. Kolson. Relapsing-remitting multiple sclerosis: longitudinal analysis of MR images - lack of correlation between changes in T2 lesion volume and clinical findings. *Radiology*, 213:395–399, 1999.

[91] S. Mukhopadhyay and B. Chanda. A multiscale morphological approach to local contrast enhancement. *Signal Processing*, 80:685–696, 2000.

[92] S. Mukhopadhyay and B. Chanda. An edge preserving noise smoothing technique using multiscale morphology. *Signal Processing*, 82:527–544, 2002.

[93] S. Mukhopadhyay and B. Chanda. Multiscale morphological segmentation of gray-scale images. *IEEE Trans Image Process*, 12:533–549, 2003.

[94] L. Nyúl, J. K. Udupa, and P. K. Saha. Incorporating a measure of local scale in voxel-based 3D image registration. *IEEE Transactions on Medical Imaging*, 22:228–237, 2003.

[95] L. G. Nyúl, A. X. Falcão, and J. K. Udupa. Fuzzy-connected 3D image segmentation at interactive speeds. *Graphical Models and Image Processing*, 64:259–281, 2003.

[96] N. Okabe, J. Toriwaki, and T. Fukumura. Paths and distance functions in three dimensional digitized pictures. *Pattern Recognition Letters*, 1:205–212, 1983.

[97] N. Otsu. A threshold selection methods from grey-level histograms. *IEEE Transactions on Pattern Analysis and Machine Intelligence*, 9:62–66, 1979.

[98] K. Park and C. Lee. Scale-space using mathematical morphology. *IEEE Trans Pattern Analysis and Machine Intelligence*, 18:1121–1126, 1996.

[99] A. Bouchet J. Pastore and V. Ballarin. Segmentation of medical images using fuzzy mathematical morphology. *Journal of Computer Science & Technology*, 7:256–262, 2007.

[100] M. Pelillo. Matching free trees, maximal cliques, and monotone game dynamics. *IEEE Transactions on Pattern Analysis and Machine Intelligence*, 24(11):1535–1541, 2002.

[101] M. Pelillo, K. Siddiqi, and S. W. Zucker. Matching hierarchical structures using association graphs. *IEEE Transactions on Pattern Analysis and Machine Intelligence*, 21(11):1105–1120, 1999.

[102] P. Perona and J. Malik. Scale-space and edge detection using anisotropic diffusion. *IEEE Transactions on Pattern Analysis and Machine Intelligence*, 12(7):629–639, 1990.

[103] C. Pisupati, C. Pisupati, L. Wolff, W. Mitzner, and E. Zerhouni. Geometric tree matching with applications to 3D lung structures. In *Proceedings of the Twelfth Annual Symposium On Computational Geometry, ACM*, pages 19–20. Press, 1996.

[104] C. Pisupati, L. Wolff, W. Mitzner, and E. Zerhouni. Tracking 3-D pulmonary tree structures. mathematical methods in biomedical image analysis. In *the Workshop on Mathematical Methods in Biomedical Image Analysis*, pages 160–169, 1996.

[105] I. Pitas and A. N. Venetsanopoulos. Morphological shape decomposition. *IEEE Trans. Pattern Anal. Machine Intell.*, 12:38–45, 1990.

[106] S. M. Pizer, D. Eberly, and D. S. Fritsch. Zoom-invariant vision of figural shape: the mathematics of core. *Computer Vision and Image Understanding*, 69:55–71, 1998.

[107] A. T. Popov. Convexity indicators based on fuzzy morphology. *Pattern Recognit. Lett.*, 18:259–267, 1997.

[108] J. G. Postaire, R. D. Zhang, and C. Lecocq-Botte. Clustering analysis by binary morphology. *IEEE Transactions on Pattern Analysis and Machine Intelligence*, 15:170–180, 1993.

[109] B. L. Rice(Jr.) and J. K. Udupa. Clutter-free volume rendering for magnetic resonance angiography using fuzzy connectedness. *International Journal of Imaging Systems and Technology*, 11:62–70, 2000.

[110] A. Rosenfeld. Adjacency in digital pictures. *Information and Control*, 26:24–33, 1974.

[111] A. Rosenfeld. Fuzzy digital topology. *Information and Control*, 40:76–87, 1979.

[112] A. Rosenfeld. The fuzzy geometry of image subsets. *Pattern Recognition Letters*, 10:311–317, 1984.

[113] A. Rosenfeld and A. C. Kak, editors. *Digital Picture Processing I vol. 1*. Academic Press, Inc., Orlando, FL, 1982.

[114] A. Rosenfeld and A. C. Kak, editors. *Digital Picture Processing II vol. 2*. Academic Press, Inc., Orlando, FL, 1982.

[115] A. Rosenfeld and J. Pfaltz. Sequential operations in digital picture processing. *J. Assoc. Comput. Mach.*, 13:471–494, 1966.

[116] A. Rosenfeld and J. Pfaltz. Distance functions in digital pictures. *Pattern Recognition*, 1:33–61, 1968.

[117] P. K. Saha. Tensor scale: a local morphometric parameter with applications to computer vision and image processing. *Computer Vision and Image Understanding*, 99:384–413, 2005.

[118] P. K. Saha and B. B. Chaudhuri. Detection of 3D simple points for topology preserving transformation with application to thinning. *IEEE Transactions on Pattern Analysis and Machine Intelligence*, 16:1028–1032, 1994.

[119] P. K. Saha and B. B. Chaudhuri. 3D digital topology under binary transformation with applications. *Computer Vision and Image Understanding*, 63:418–429, 1996.

[120] P. K. Saha and B. B. Chaudhuri. 3D digital topology under binary transformation with applications. *Computer Vision and Image Understanding*, 63:418–429, 1996.

[121] P. K. Saha, B. B. Chaudhuri, B. Chanda, and D. D. Majumder. Topology preservation in 3D digital space. *Pattern Recognition*, 27:295–300, 1994.

[122] P. K. Saha, B. B. Chaudhuri, and D. D. Majumder. A new shape preserving parallel thinning algorithm for 3D digital images. *Pattern Recognition*, 30:1939–1955, 1997.

[123] P. K. Saha, Z. Gao, S. K. Alford, M. Sonka, and E. A. Hoffman. Topomorphologic separation of fused isointensity objects via multiscale opening: Separating arteries and veins in 3-D pulmonary CT. *IEEE transactions on medical imaging*, 29:840–851, 2010.

[124] P. K. Saha, B. R. Gomberg, and F. W. Wehrli. Three-dimensional digital topological characterization of cancellous bone architecture. *International Journal of Imaging Systems and Technology*, 11:81–90, 2000.

[125] P. K. Saha and A. Rosenfeld. Determining simplicity and computing topological change in strongly normal partial tilings of R2 or R3. *Pattern Recognition*, 33:105–118, 2000.

[126] P. K. Saha and J. K. Udupa. Iterative relative fuzzy connectedness and object definition: theory, algorithms, and applications in image segmentation. In *IEEE Workshop on Mathematical Methods in Biomedical Image Analysis*, Hilton Head, South Carolina, 2000.

[127] P. K. Saha and J. K. Udupa. Fuzzy connected object delineation: axiomatic path strength definition and the case of multiple seeds. *Computer Vision and Image Understanding*, 83:275–295, 2001.

[128] P. K. Saha and J. K. Udupa. Optimum threshold selection using class uncertainty and region homogeneity. *IEEE Transactions on Pattern Analysis and Machine Intelligence*, 23:689–706, 2001.

[129] P. K. Saha and J. K. Udupa. Scale based image filtering preserving boundary sharpness and fine structures. *IEEE Transactions on Medical Imaging*, 20:1140–1155, 2001.

[130] P. K. Saha, J. K. Udupa, and J. M. Abrahams. Automatic bone-free rendering of cerebral aneurysms via 3D-CTA. In *SPIE: Medical Imaging*, pages 1264–1273, San Diego, CA, 2001.

[131] P. K. Saha, J. K. Udupa, E.F. Conant, D.P. Chakraborty, and D. Sullivan. Breast tissue glandularity quantification via digitized mammograms. *IEEE Transactions on Medical Imaging*, 20:792–803, 2001.

[132] P. K. Saha, J. K. Udupa, and D. Odhner. Scale-based fuzzy connected image segmentation: theory, algorithms, and validation. *Computer Vision and Image Understanding*, 77:145–174, 2000.

[133] P. K Saha and F. W Wehrli. Measurement of trabecular bone thickness in the limited resolution regime of in vivo MRI by fuzzy distance transform. *IEEE Transactions on Medical Imaging*, 23:53–62, 2004.

[134] P. K. Saha, F. W. Wehrli, and B. R. Gomberg. Fuzzy distance transform: theory, algorithms, and applications. *Computer Vision Image Understanding*, 86:171–190, 2002.

[135] P. K. Saha, Y. Xu, H. Duan, A. Heiner, and G. Liang. Volumetric topological analysis: A novel approach for trabecular bone classification on the continuum between plates and rods. *IEEE Transactions on Medical Imaging*, page to be published on November, 2010.

[136] S. Samarasekera, J. K. Udupa, Y. Miki, and R. I. Grossman. A new computer-assisted method for enhancing lesion quantification in multiple sclerosis. *Journal of Computer Assisted Tomography*, 21:145–151, 1997.

[137] J. Serra, editor. *Image Analysis and Mathematical Morphology*. Academic Press, London, 1982.

[138] J. Serra. Introduction to mathematical morphology. *Computer Vision, Graphics, and Image Processing*, 35:283–305, 1986.

[139] B. Shao, Y. Jiang, and Z. Yang. The research on video supervision technology based on mathematical morphology. In *the International Conference on Industrial Mechatronics and Automation*, 2009.

[140] F. Y. Shih and C. C. Pu. Analysis of the properties of soft morphological filtering using threshold decomposition. *IEEE Trans. Signal Processing*, 43:539–544, 1995.

[141] H. Shikata, E. A. Hoffman, and M. Sonka. Automated segmentation of pulmonary vascular tree from 3D CT images. In *SPIE: Medical Imaging*, pages 107–116, San Diego, CA, 2004.

[142] D. Sinha and E. R. Dougherty. A general axiomatic theory of intrinsically fuzzy mathematical morphologies. *IEEE Trans. Fuzzy Syst*, 3:389–403, 1995.

[143] M. Sonka, V. Hlavac, and R. Boyle, editors. *Image Processing, Analysis, and Machine Vision*. PWS Publishing, Pacific Grove, CA, 1999.

[144] A. D. A. Souza, J. K. Udupa, and P. K. Saha. Volume rendering in the presence of partial volume effects. *IEEE Transactions on Medical Imaging*, 24:223–235, 2005.

[145] V. Starovoitov. A clustering technique based on the distance transform. *Pattern Recognition Letters*, 17:231–239, 1996.

[146] S. R. Sternberg. Cellular computers and biomedical image processing. In *Biomedical Images and Computers, J. Sklansky and J. C. Biscounte, Eds*, pages 294–391, Berlin, 1982. Springer.

[147] S. R. Sternberg. Grayscale morphology. *Computer Vision, Graphics, and Image Processing*, 35:333–355, 1986.

[148] S. Svensson. Centres of maximal balls extracted from a fuzzy distance transform. In *8th International Symposium on Mathematical Morphology*, pages 19–20, Rio de Janeiro, Brazil, 2007.

[149] S. Svensson. A decomposition scheme for 3D fuzzy objects based on fuzzy distance information. *Pattern Recognition Letters*, 28:224–232, 2007.

[150] S. Svensson. Aspects on the reverse fuzzy distance transform. *Pattern Recognition Letters*, 29:888–896, 2008.

[151] T. Blaffert C. Lorenz T. Büelow, R. Wiemker and S. Renisch. Automatic extraction of the pulmonary artery tree from multi-slice CT data. In *SPIE: Medical Imaging*, pages 730–740, San Diego, CA, 2005.

[152] M. Tabb and N. Ahuja. Multiscale image segmentation by integrated edge and region detection. *IEEE Transactions on Image Processing*, 6:642–655, 1997.

[153] W. H. Tang and Albert C. S. Chung. Cerebral vascular tree matching of 3D-RA data based on tree edit distance. In *Medical Imaging and Augmented Reality*, pages 116–120, 2006.

[154] A. Tsai, W. Wells, C. Tempany, E. Grimson, and A. Willsky. Mutual information in coupled multi-shape model for medical image segmentation. *Med Image Anal*, 8:429–445, 2004.

[155] J. Tschirren, E. A. Hoffman, G. McLennan, and M. Sonka. Branchpoint labeling and matching in human airway trees. In *Medical Imaging 2003: Physiology and Function: Methods, Systems, and Applications*, volume 5031, pages 187–194, 2003.

[156] J. Tschirren, G. McLennan, K. Palagyi, E. A. Hoffman, and M. Sonka. Matching and anatomical labeling of human airway tree. *IEEE Transactions on Medical Imaging*, 24(12):1540–1547, 2005.

[157] J. K. Udupa and G. T. Herman, editors. *3D Imaging in Medicine*. CRC Press, Boca Raton, FL, 1991.

[158] J. K. Udupa and P. K. Saha. Fuzzy connectedness in image segmentation. *Proceedings of IEEE, Emerging Medical Imaging Technology, (invited paper)*, 91:1649–1669, 2003.

[159] J. K. Udupa, P. K. Saha, and R. A. Lotufo. Relative fuzzy connectedness and object definition: theory, algorithms, and applications in image segmentation. *IEEE Transactions on Pattern Analysis and Machine Intelligence*, 24:1485–1500, 2002.

[160] J. K. Udupa and S. Samarasekera. Fuzzy connectedness and object definition: theory, algorithms, and applications in image segmentation. *Graphical Models and Image Processing*, 58:246–261, 1996.

[161] J. K. Udupa, L. Wei, S. Samarasekera, Y. Miki, M. A. van Buchem, and R. I. Grossman. Multiple sclerosis lesion quantification using fuzzy connectedness principles. *IEEE Transactions on Medical Imaging*, 16:598–609, 1997.

[162] C. M. van Bemmel, L. J. Spreeuwers, M. A. Viergever, and W. J. Niessen. Level-set-based artery-vein separation in blood pool agent CE-MR angiograms. *IEEE Trans Med Imaging*, 22:1224–1234, 2003.

[163] R. van der Boomgaard and A. Smeulders. Morphological multiscale image analysis. In *the Proc. First Int'l Workshop on Math. Morphology and Its Applications to Signal Processing*, Barcelona, Spain, 1993.

[164] D. M. Vasilescu, Z. Gao, L. Yin, T. Eggleston, P. K. Saha, and E. A. Hoffman. Automatic, objective assessment of adult murine acinar morphometry via optically magnified microct. In *American Journal of Respiratory and Critical Care Medicine*.

[165] B. J. H. Verwer. Local distances for distance transformations in two and three dimensions. *Pattern Recognition Letters*, 12:671–682, 1991.

[166] K. L. Vincken, A. S. E. Koster, and M. A. Viergever. Probabilistic multiscale image segmentation. *IEEE Transactions on Pattern Analysis and Machine Intelligence*, 19:109–120, 1997.

[167] S. Wan, E. L. Ritman, and W. E. Higgins. Multi-generational analysis and visualization of the vascular tree in 3D micro-CT images. *Computers in Biology and Medicine*, 32:55–71, 2002.

[168] F. W. Wehrli, B. R. Gomberg, P. K. Saha, H. K. Song, S. N. Hwang, and P. J. Snyder. Digital topological analysis of in vivo magnetic resonance microimages of trabecular bone reveals structural implications of osteoporosis. *Journal of Bone Mineral Research*, 16:1520–1531, 2001.

[169] J. Williams and L. Wolff. Analysis of the pulmonary vascular tree using differential geometry based vector fields. *Computer Vision and Image Understanding*, 65(2):226–236, 1997.

[170] A. P. Witkin. Scale-space filtering. In W. H. Freeman and Company, editors, *8th International Joint Conference Artificial Intelligence*, Karlsruhe, West Germany, 1983.

[171] J. K. Udupa Y. Zhuge and P. K. Saha. Vectorial scale-based fuzzy connected image segmentation. In *SPIE: Medical Imaging*, pages 1476–1487, San Diego, CA, 2002.

[172] T. Yonekura, M. Matsuhiro, S. Saita, M. Kubo, Y. Kawata, N. Niki, H. Nishitani, H. Ohmatsu, R. Kakinuma, and N. Moriyama. Classification algorithm of pulmonary vein and artery based on multi-slice CT image. In *SPIE: Medical Imaging*, pages 65142E1–65142E8, San Diego, CA, 2007.

[173] K. Yu, W.E. Higgins, and E. L. Ritman. 3D model-based vascular tree analysis using differential geometry. In *IEEE International Symposium on Biomedical Imaging: Nano to Macro*, pages 177–180, 2004.

[174] A.L. Yuille and T.A. Poggio. Scaling theorems for zero crossings. *IEEE Trans. Pattern Analysis and Machine Intelligence*, 8:15–25, 1986.

[175] W. Zheng, H. Yang, H. Sun, and H. Fan. X-ray image enhancement based on multiscale morphology. In *International Conference on Bioinformatics and Biomedical Engineering*, 2007.

[176] X. Zhuang and R. M. Haralick. Morphological structuring element decomposition. *Computer Vision, Graphics, and Image Processing*, 35:370–382, 1986.